EVALUATION OF WEATHER RESEARCH AND FORECASTING MODEL PHYSICS IN SIMULATING WEST AFRICAN MONSOON

BY

GBODE, IMOLEAYO EZEKIEL
B.Tech, M.Tech (MET/07/0895)

A Thesis in the Department of Meteorology and Climate Science, School of Earth and Mineral Sciences, in partnership with the West African Science Service Center on Climate Change and Adapted Land Use (WASCAL) submitted to the School of Postgraduate Studies in partial fulfillment of the requirements for the award of Doctor of Philosophy in Meteorology and Climate Science of the Federal University of Technology, Akure, Nigeria.

SEPTEMBER, 2019

DECLARATION

I hereby declare that this Thesis was written by me and is a correct record of my own research work. It has not been presented in any previous application for any degree of this or any other University. All citations and sources of information are clearly acknowledged by means of references.

Candidate's Name: GBODE, Imoleayo Ezekiel

Signature:…… Date:25/09/2019……..

CERTIFICATION

We certify that this Thesis entitled "Evaluation of Weather Research and Forecasting Model Physics in Simulating West African Monsoon" is the outcome of the research carried out by Gbode, Imoleayo Ezekiel in the Department of Meteorology and Climate Science, the Federal University of Technology, Akure, Nigeria, in partnership with the West African Science Service Center on Climate Change and Adapted Land Use (WASCAL).

Major Supervisor's Name: Prof. K. O. Ogunjobi

Signature: ……... Date: ……..

Co-Supervisor's Name: Dr. V. O. Ajayi

Signature: ……... Date: ……..

Advisor's Name: Dr. J. Dudhia

Signature:  Date: 25/09/2019

ACKNOWLEDGEMENTS

The German Federal Ministry of Education and Research (BMBF) primarily funded this research through the West African Science Service Center on Climate Change and Adapted Land-Use Doctorate Research Programme in West African Climate Systems (WASCAL DRP-WACS) host in the Federal University of Technology Akure, Nigeria.

I am grateful to my Major Supervisor, Prof. K. O. Ogunjobi, Co-Supervisor, Dr. V. O. Ajayi, and Advisor, Dr. J. Dudhia for their encouragement, constructive criticism, insightful suggestions and comments throughout the conduct of this research. The valuable comments and suggestions of the external examiner, Prof. J. A. Adedoyin, and other members of the examination panel are highly appreciated.

Here is thanking the Directors and staffs of WASCAL Head Office, Accra, Ghana and DRP-WACS FUTA, Nigeria for their coordination and administration throughout the course of study. Also, I would like to extend my profound gratitude to the HOD of MCS department, Prof. A. A. Balogun, SEMS PG Seminar Coordinator, Prof. Y. A. Asiwaju-Bello and, the Dean of SEMS, Prof. P. A. Enikanselu.

Many thanks to the Mesoscale and Microscale Meteorology (MMM) Laboratory of the National Center for Atmospheric Research (NCAR) for supporting the research work. Also thanks to Wei Wang, Changhai Liu, and Akintomide A. Akinsanola for their constructive comments, and Ming Chen and Michael Duda for technical supports as well as Dr. Joseph Intsiful and Prof. Jerome Adebayo Omotosho for quality mentorship.

The initial model configuration was done on the DRP-WACS FUTA cluster unit. I would like to acknowledge high-performance computing support from Yellowstone and

Cheyenne provided by NCAR's Computational and Information Systems Laboratory, sponsored by the National Science Foundation.

Special thanks go to my counselors, Prof. Oyetunji Akinlabi and Surv. (Mrs.) Oyetunji Falilat, my wonderful and very encouraging parents Mr. Gbode Stephen O. and Mrs. Gbode Hannah A., and my siblings; Solomon Gbode, Kemi Gbode, Tosin Owaseye and Victoria Adepoju, as well as my colleagues. Furthermore, I sincerely thank and appreciate my dear wife, Mrs. Gbode Omoyeni Abosede, for her moral support and understanding. Last but not the least, I thank my lovely daughter, Iremide Christiana Gbode, for the joy she brought into my household.

DEDICATION

This Thesis is dedicated to the Almighty GOD, the giver of knowledge, understanding, and wisdom, who made it possible for this research to be successfully executed and to all taxpayers whose money is used to support research and development in developing countries.

ABSTRACT

This research evaluates the ability of Weather Research and Forecasting model physics in simulating the West African monsoon. The purpose is to identify a possible model physics combinations in the WRF model whose outputs can be used to inform weather- and climate-related decision-making process at local to regional scale. In the study, the sensitivity of West African Monsoon (WAM) regimes to three model physics (i.e. Cumulus (CU), Microphysics (MP) and Planetary Boundary Layer (PBL) parameterization schemes) is assessed, performance of the model in representing the WAM dynamics is evaluated and impact of warming climate on WAM under the RCP8.5 scenario is also assessed.

Twenty-seven (27) WRF simulations of the August-September 2007 monsoon regime at a 20-km grid over West Africa were evaluated to investigate the sensitivity of the WAM regime to the three model physics. The focus was on precipitation and surface temperature during the simulated period. The model's precipitation was evaluated against the TRMM (reference), CMORPH and GPCP satellite rainfall products. Also, the surface temperature was evaluated against the ERA-Interim (reference), NCEP, MERRA, and GSAT. Results showed that all model physics combinations simulated the diurnal cycles of surface temperature better than the simulation of precipitation. A comparative model skill score was developed and used to identify that combination of WSM5-MYNN-nTDK and GD-MYJ-BMJ are best performing physics combinations in both temperature and precipitation. Also, the three WRF model physics combinations reproduced the characteristics of the region's monsoon during selected normal (2007), wet (2008 and 2010) and dry (2001 and 2011) years. The dynamics of WAM such as monsoon flow,

African Easterly Jet, and Tropical Easterly Jet, are replicated by most of the model combinations. Therefore, underscoring the strong potential impact of regional moisture, heat and momentum transport and redistribution on the monsoon dynamics as prescribed by the physics.

Lastly, the Pseudo-Global Warming (PGW) simulation method perturbed by CESM1.0-CAM5.2 is employed to assess the impact of warming on WAM, the result shows a slight increase in precipitation amount (-2 to 16%) in the 2070s when compared with the current (reference) climate. This change is expected to be more pronounced in the Sahel, where the value is 16%, and less than 3% in the Guinea Coast. Furthermore, there is a decrease (increase) in both light and moderate (heavy) rainfall days.

The outcomes of this research underscore the significance of WRF model as a potentially useful tool to investigate how future WAM seasons could vary in a changing climate. This provides relevant information to improve the understanding of the possible implications of such changes on economic activities such as agriculture, water resources, and other climate-related sectors, and to guide the design and implementation of climate-resilient projects.

TABLE OF CONTENTS

LIST OF TABLES

LIST OF FIGURES

LIST OF EQUATIONS

LIST OF ABBREVIATIONS

AEJ	African Eater Jet
AEW	African Easterly Waves
AMIP	Atmospheric Model Intercomparison Project
AMMA	African Multidisciplinary Monsoon Analysis
AR5	Fifth Assessment Report
AWJ	African Westerly Jet
B	Mean Bias
BMJ	Bett-Miller-Janjić
CAMv5.2	Community Atmospheric Model version 5.2
CAPE	Convective Available Potential Energy
CESMv1	Community Earth System Model version 1
CFC-11	Chlorofluorocarbons-11
CFC-12	Chlorofluorocarbons-12
CH_4	Methane
CISL	Computation and Information Systems Laboratory
CMORPH	Climate Prediction Center MORPHing technique
CO_2	Carbon dioxide
CORDEX	Coordinated Regional Downscaling Experiment
CPC	Climate Prediction Center
CPS	Cumulus Parameterization Scheme
CRU	Climate Research Unit
CU	Cumulus

DOE	Department of Energy
ECMWF	European Center for Medium-range Weather Forecast
ENSEMBLES	Ensemble-based Prediction of Climate Change and their Impacts
ERAI	European Center for Medium-range Weather Forecast Re-Analysis Interim
FAO	Food and Agriculture Organization
FNL	Final analysis
GCM	Global Circulation Model
GD	Goddard
GF	Grell-Freitas
GHG	Greenhouse gas
GPCC	Global Precipitation Climatology Center
GPCP	Global Precipitation Climatology Project
GSAT	Global Surface Air Temperature
GWL	Global Warming Level
IPCC	Intergovernmental Panel on Climate Change
ITCZ	Inter-Tropical Convergence Zone
ITD	Inter-Tropical Discontinuity
JJAS	June-September
KF	Kain-Fritsch
LAM	Limited Area Model
LENS	Large Ensemble Community Project
LLJ	Low level Jet

MAE	Mean Absolute Bias
MCS	Mesoscale Convective Systems
MERRA	Modern-Era Retrospective analysis for Research and Applications
MP	Microphysics
MSS	Model Skill Score
MYJ	Mellor-Yamada-Janjić
MYNN	Mellor-Yamada-Nakanishi-Niino 2.5 level Turbulent Kinetic Energy
N_2O	Nitrous oxide
NCAR	National Center for Atmospheric Research
NCEI	National Centers for Environmental Information
NCEP	National Center for Environmental Prediction
nGF	Newly modified Grell-Freitas
NOAA	National Oceanic and Atmospheric Administration
nSAS	Newly modified Simplified Arakawa-Schubert
nTDK	Newly modified Tiedtke
PBL	Planetary Boundary Layer
PGW	Pseudo-Global Warming
r	Pearson Correlation Coefficient
R-2	Reanalysis 2
RCM	Regional Climate Model
RCP	Representative Concentration Pathway

RCP2.6	Representative Concentration Pathway for 2.6 Wm^{-2} radiative forcing
RCP4.5	Representative Concentration Pathway for 4.5 Wm^{-2} radiative forcing
RCP6.0	Representative Concentration Pathway for 6.0 Wm^{-2} radiative forcing
RCP8.5	Representative Concentration Pathway for 8.5 Wm^{-2} radiative forcing
RDA	Research Data Archive
RegCM	Regional Climate Mode
RRTMG	Rapid Radiative Transfer Model with Greenhouse gases
SAS	Simplified Arakawa-Schubert
SHL	Saharan Heat Low
SRES	Special Report on Emission Scenarios
SRP	Satellite Rainfall Product
SST	Sea Surface Temperature
T2m	Surface temperature at 2meters
TEJ	Tropical Easterly Jet
TKE	Turbulent Kinetic Energy
TRMM	Tropical Rainfall Measurement Mission
USAID	United States Agency for International Development
WA	West Africa
WAM	West African Monsoon

WAWJ	West African Westerly Jet
WRF	Weather Research and Forecasting model
WSM5	Weather Research and Forecasting model Single moment class 5
YSU	Yonsei University

CHAPTER ONE

INTRODUCTION

1.1 BACKGROUND

The West African rainfall season is dominated by the West African Monsoon (WAM), which provides about 75% to 90% of the total rainfall in the region (Hagos & Cook, 2007a). Most countries practice rainfed agriculture in West Africa, as a major source of sustenance, and greatly depend on the monsoon for water supply to ensure food security. Aside this importance, the variability of the monsoon system can also be related to issues of health, water resources and demography for nations of the region (Janicot et al., 2008; Redelsperger et al., 2006).

The WAM is a large-scale circulation system defined by changes in the direction of surface winds at lower level of the atmosphere. The monsoon is initiated as a result of meridional horizontal temperature gradient between the Atlantic Ocean and the continent. It is a complex interaction of multiple dynamical atmospheric rainfall-producing features such as monsoon flow, African Easterly Jet (AEJ), Tropical Easterly Jet (TEJ), African Easterly Waves (AEW) and Mesoscale Convective Systems (MCS). These features interact in a complex way to not only provide the summer monsoon rainfall but also determine the amount and variability of the produced rainfall (Redelsperger et al., 2002).

Rainfall over the West African region depends on northward inland propagation of rain band associated with the movement of the Inter-Tropical Discontinuity (ITD). The propagation of the rain band subjects the rainfall across the different climatic zones of West Africa; namely Guinea coast, Savannah and Sahel, to high intraseasonal, interannual and interdecadal variability. Over the past decades, such variability has

caused a downward trend in the rainfall amount received during the wet season (Biasutti & Giannini, 2006; Dai et al., 2004; L'Hôte et al., 2002; Nicholson et al., 2000) thereby leading to drought, which in turn results to famine in the Sahel. To understand the origin of this variability several mechanisms have been analyzed by previous studies. Among these mechanisms are ocean Sea Surface Temperature (SST) anomalies (Eltahir & Gong, 1995; Fontaine et al., 1998; Giannini et al., 2003; Hagos & Cook, 2008; Hoerling et al., 2006; Nicholson & Webster, 2007), continental surface conditions (Charney et al., 1977; Semazzi & Sun, 1997; Wang & Eltahir, 2000), atmospheric structures (Jenkins et al., 2005; Nicholson & Grist, 2001; Nicholson, 2008) and possible effect of global climate change (Held & Soden, 2006; Paeth & Hense, 2004). Other studies also found the dynamics of the low-level monsoon flow, the mid-tropospheric AEJ and the upper-level TEJ to have modulating effects on the rainfall amount and variability at both intraseasonal and interannual timescales.

Though extensive studies on WAM have been performed, there are still fundamental gaps in our knowledge of its variability and the interaction between its associated features. This is partly due to the lack of appropriate observational datasets; a major reason for the launch of the African Monsoon Multidisciplinary Analysis (AMMA) project in 2003 (Redelsperger et al., 2006). Complementarily, atmospheric climate models have become a useful tool to study and understand the WAM variability and its associated features. Global Circulation Models (GCMs) lacks in their ability to represent the main features of the WAM climate and spatiotemporal rainfall distribution variability (Hourdin et al., 2010; Sylla et al., 2010; Vizy & Cook, 2002; Xue et al., 2010). This deficiency could be attributed to a number of reasons such as their coarse horizontal

resolution (100–400 km; Druyan et al., 2009; IPCC, 2007), model formulation, as well as initialization of their land surface/soil moisture (Xue et al., 2010; Yamada et al., 2012) and therefore are less suitable to fully represent the local and regional topographical forcing and mesoscale weather features.

An alternative approach to resolve these fine-scale features is by considering a domain that covers a certain region of the globe in a Limited Area Models (LAMs), also known as mesoscale models. Examples of models in such category include; Regional Climate Model (RegCM) and Weather Research and Forecasting (WRF) model. These models are suitable for dynamical downscaling of GCMs simulation or reanalysis as well as performing efficient climate and weather simulation at a horizontal resolution of typically 50km or less (Flaounas et al., 2011; Giorgi & Mearns, 1999; Klein et al., 2015). RCMs also provides an improved description of the regional forcing such as surface heterogeneities while being controlled by the large-scale boundary conditions taken from the GCM or reanalysis data.

So far, the potential of WRF model in simulating atmospheric processes over the West African region is yet to be fully explored as only a few numbers of studies have utilized the model. Also, the model has several physics options that can be combined in different ways to reproduce a particular atmospheric phenomenon of interest but previous studies have only used some few combinations with no clear recommendation on the best performing physics suit. For example, Flaounas et al. (2011) conducted a first comprehensive study of the sensitivity of WRF for three cumulus and two planetary boundary layer parameterizations during the WAM of 2006. The work investigated the behavior of some selective model physics schemes by analyzing their capability in

representing surface variables and some dynamical monsoon features but found no consistently best-performing configuration. Noble et al. (2014) also compared African Easterly Wave occurrences of 64 WRF configurations with those of two reanalysis datasets and radiosonde observations for 12-days time slices over 10 years. The result of the study gave valuable insights into the development of these atmospheric disturbances and revealed deficiencies of the model in reproducing them. Furthermore, Klein et al. (2015) considered the advantages of an ensemble approach to generalize the process-based impact of individual parameterization schemes. Their study examined the ability of a WRF multi-physics ensemble in representing certain WAM features. They found that microphysics and planetary boundary layer schemes contribute most to the ensemble spread for monsoon precipitation over the study region. These earlier studies showed that the simulated atmospheric phenomena are sensitive to the different physics of the model. So far the best scheme combination in the model configuration and the statistical significance of WRF in simulating the WAM features has not been presented.

Although, studies have provided substantial information as regards model improvement and the sensitivity of WAM to model physics and configuration, however, most of the results contain large uncertainties owing to the inherent systematic biases (Li et al., 2015a), which underline the utmost importance for improvement in the simulation of vital atmospheric processes such as the WAM. This study will consolidate on previous works by providing a comprehensive evaluation of more robust model physics combination with a major focus on improving the WAM simulations and its associated rainfall-producing features. Furthermore, the identified best model physics combination would be used to project the future outlook of the WAM.

1.2 STATEMENT OF PROBLEM

The application of weather and climate models is a useful tool to study global and regional atmospheric processes and phenomena, mostly the prominent WAM and its associated features. However, these models still contain large uncertainties. These uncertainties could influence the accuracy of the model outputs and thus, hinder the use of findings derived from model outputs to make and implement sound economic plans and policies. Studies have shown that a large amount of uncertainties in these models is produced by parameterization of physical atmospheric processes within the model. Other sources of errors are inherent in the forcing data, representation of the land use land cover of the model domain and to a little extent the computing resources. All these factors limit the accuracy of representing the atmospheric phenomenon of interest and thus, influence the generation of reliable climate information necessary to achieve sustainable development goals in different sectors of the economy such as agriculture, water resource management and energy etc. For these reasons, numerous studies have provided substantial information and attempt to evaluate the sensitivity of WAM to model physics and configuration for improved simulation. The volume of present information still provides room for further studies to improve and test for the sensitivity of WAM and its associated features within the model environment.

1.3 AIM AND OBJECTIVES

1.3.1 Aim

The aim of this study is to evaluate WRF model physics in simulating the West African Monsoon (WAM) and its associated features.

1.3.2 Objectives

The specific objectives of the research are to;

i. assess the sensitivity of West African Monsoon (WAM) regimes to three model physics (i.e. Cumulus (CU), Microphysics (MP) and Planetary Boundary Layer (PBL) parameterization schemes),

ii. evaluate the performance of the model in representing the WAM dynamics in comparison to observed data, and

iii. apply the identified best performing model physics combination to assess the impact of warming climate on WAM under the Representative Concentration Pathway (RCP8.5).

1.4 JUSTIFICATION

The rationale behind this research is to identify a regional climate model whose output can be used as an integral input to provide sound climate information that will guide policy formulation and decision-making in climate-related sectors of the economy at the national and regional scale. Model evaluation, application, and development are most vital areas that have been explored in past and present-day researches, particularly in data-sparse region like Africa. It is therefore critical to constantly evaluate the available model physics options, which are subjected to modifications and regular updates. More so, there has been more demand for reliable simulation of the monsoon system because of its influence on physical, chemical and biological environment, which in turn affects life in nations of the region and globally (Janicot et al., 2008; Mounier et al., 2008; Redelsperger et al., 2006), however, this has been challenging to date. In West

Africa, the availability of dense surface and upper air observation data networks is a major issue that restricts our understanding of the large-scale monsoon system and its associated rainfall-producing features. Previous studies have provided substantial information as regards model improvement and the sensitivity of WAM to model physics and configuration; however, most of the results contain large uncertainties owing to the inherent systematic biases, which underscore the utmost importance for improving the simulation of vital atmospheric processes. Also, the role of the monsoon in producing rainfall of the region strengthens the above argument. Hence, the need for the current study to consolidate on previous work by providing a comprehensive evaluation of more robust model physics combination with a major focus on improving WAM simulation.

1.5 THE CONTRIBUTION OF THE RESEARCH TO KNOWLEDGE

The outcome of this research will be useful for the model development community to identify areas of model structures that need to be modified for improved model outputs. Also, to close the gaps in our scientific understanding of how the West African rainfall will potentially respond to the impact of future global warming and other emission pathways. Policymakers can, therefore, use such information to make informed decision and policies that will be robust enough to enhance sustainable economic planning and climate-resilient development. These measures will help to reduce risk and challenges facing key sectors of the economy such as agriculture, water resources, public health, energy, and other weather-sensitive sectors. Besides, the study will suggest new promising research areas for future studies.

CHAPTER TWO

LITERATURE REVIEW

2.1 WEST AFRICAN MONSOON

Monsoon is the seasonal reversal of surface wind direction accompanied by changes in precipitation. The West African summer monsoon is a climatological feature that dominates the West African rainfall season during May through to September and brings a significant amount of rainfall to the region (Hagos & Cook, 2007; Janicot et al., 2008; Sylla et al., 2013; among others). The rainfall produced by the monsoon system is largely controlled by the advection of warm-moist airmass from the Gulf of Guinea in the low-levels of the atmosphere (Sultan & Janicot, 2000). Several studies have identified various factors that control the monsoon variability. These factors include the variability of ocean sea surface temperature (e.g. Fontaine et al., 1998; Giannini et al., 2003), continental land surface conditions (Charney et al., 1977; Wang & Eltahir, 2000) and atmospheric circulation (e.g. Jenkins et al., 2005; Nicholson & Grist, 2001).

In the context of atmospheric circulation, the WAM is a large-scale circulation system embedded with different rainfall producing systems such as the Inter-Tropical Convergence Zone (ITCZ), Inter-Tropical Discontinuity (ITD), African Easterly Jet (AEJ), Tropical Easterly Jet (TEJ), Warm Saharan Air (above the Saharan heat low (SHL)), and Dry Air (as shown in Figure 2.1). Previous studies have shown that the interannual variability of WAM rainfall, mostly in the Sahel, is linked to the anomalous latitudinal migration of the ITCZ (Bryson, 1973; Kraus, 1977) while others argued that the link between ITCZ position and Sahel rainfall was weak (Miles & Follard, 1974; Nicholson, 1981), but the relationship between the ITCZ defined by rainfall intensity is

evident. Afterward, a significant paradigm shift emerged to establish that the interannual variability rather is linked to changes in higher-level circulation features (Nicholson, 2013). These in addition to the above-mentioned rainfall producing systems include two low-level westerly jets, the African Westerly Jet (AWJ) over the continent and the West African Westerly Jet (WAWJ). These features are important in determining the climatology of the WAM system, most especially in terms of interannual variability. Most of the features are apparent in the zonal circulation as described in Figure 2.2 (Grist & Nicholson, 2001; Nicholson, 2013).

2.1.1 African Easterly Jet

The African Easterly Jet (AEJ) is one of the most prominent features of strong zonal winds core (up to ~10 ms^{-1}), typically found in the mid-tropospheric layer (600-700 mb). It travels from East to West Africa (Lafore et al., 2010; Sylla et al., 2013). The jet is known to have two independent cores, that is, the western and eastern cores, which occasionally merge (Hall et al., 2006). Nicholson & Grist (2003) described the mean characteristics of the jet to be strongest in May and June, when the mean core speed of the western (10^oW to 10^oE) and eastern (10^oE to 30^oE) sector is on the order of $12ms^{-1}$ and $10ms^{-1}$, respectively. Further, Nicholson & Grist (2003) reported that the core of this jet could attain $16ms^{-1}$ and may decrease by $2ms^{-1}$ during the monsoon phase in the Sahel. The western core of the AEJ is more prominent and maintains a nearly stable latitudinal position on average about 16^oN. For the eastern core, the jet lies on the average about 13^oN during the boreal summer but could vary between 20^oN to 10^oN in some wet and dry years, respectively.

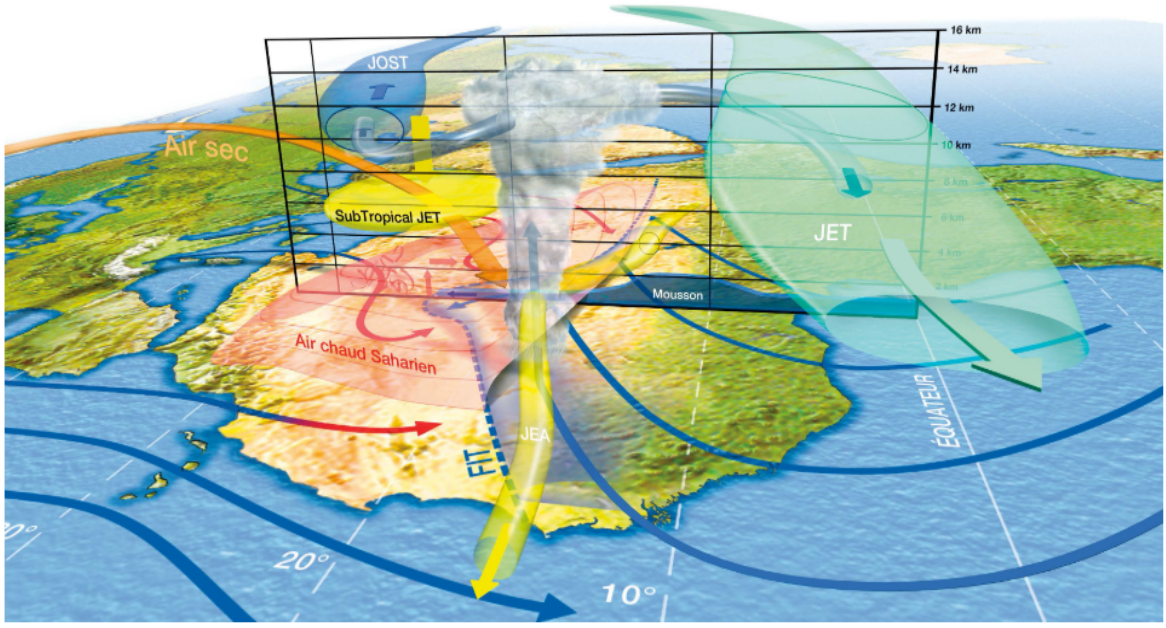

Figure 2.1: A Diagram of the West African Monsoon System showing the Interactions of Different Rainfall Producing Features.

NOTE: FIT represents ITD, "Air Chaud Saharien" represents "Warm Saharian Air", JEA represents AEJ, JET represents TEJ and "Air sec" represents "Dry Air" (Source: Lafore et al., 2010).

The zonal circulation associated with this jet creates a disturbance known as the African Easterly Waves, a critical driver of convection and rainfall (Diedhiou et al., 1998; Nicholson & Grist, 2003). The AEJ develops in response to the latitudinal temperature gradient of the southern Atlantic Ocean and Sahara, as a result causing it to have an east-west orientation (Nicholson & Grist, 2003). The temperature gradient associated with this jet is usually strong from June through August. It attains maximum intensity in May and June, before the onset of the rainy season in the Sahel. However, Chen (2005) suggests that the emergence of AEJ is consequent to the Saharan High that lies along its external boundaries. Other studies reported that moist processes contribute to the intensification of the jet (Cornforth et al., 2009) and that aerosols also influence its development (Tompkins et al., 2005). The AEJ is mainly maintained by both deep and shallow meridional circulations associated with the monsoon, which are driven by local Hadley circulation and the Saharan Heat Low (SHL), respectively (Cook, 1999; Thorncroft & Blackburn, 1999). The role of the heat low is most important during the pre- and post-monsoon seasons (Kalapureddy et al., 2010) while the boundary layer processes become dominant during the peak period (Nicholson, 2013). Chen (2005) further suggested another maintenance mechanism to be the Coriolis acceleration associated with divergent northerlies in the mid-troposphere over the Chad-Sudan region. In wet years, the core of the jet shifts further north, which enhances deep low-level monsoon flow centered at 10^{o}N. On the other hand, when the core of the jet is displaced to the south, it inhibits the monsoon flow (Figure 2.2).

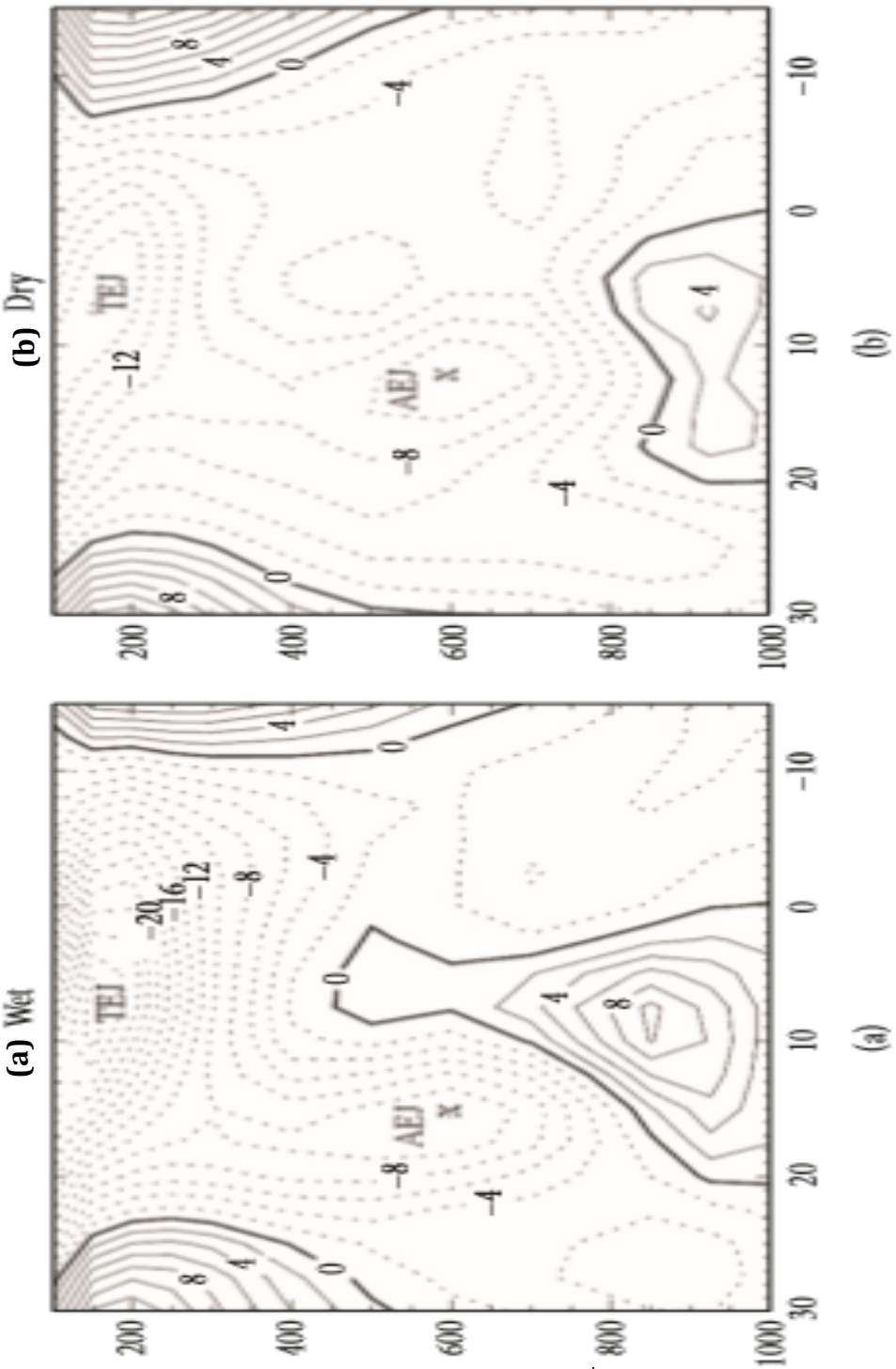

Figure 2.2: Vertical Cross-Section of Zonal Wind (ms^{-1}) in (a) Wet and (b) Dry Years.

NOTE: Dashed (Solid) lines correspond to easterly (westerly) winds. The upper-tropospheric Tropical Easterly Jet (TEJ) and the mid-tropospheric African Easterly Jet (AEJ) is shown (Source: Grist & Nicholson, 2001 in Nicholson, 2013).

2.1.2 Tropical Easterly Jet

The Tropical Easterly Jet (TEJ) develops because of the intense north-south temperature gradient between the Himalayan plateau and the Indian Ocean. Studies on this jet over the West African region are few unlike in the Asia where it is the main focus of most researches (Pattanaik & Satyan, 2000; Raman et al., 2009; Ratnam et al., 2011). It is maintained through tropical divergent circulation associated with the east-west Walker circulation and north-south Hadley circulation. During the boreal summer, the TEJ attains a mean wind speed of approximately $18ms^{-1}$ over the eastern Sahel. Though this jet exhibits little latitudinal change on a year-to-year basis over West Africa, its speed and east-west extent vary greatly (Grist & Nicholson, 2001; Nicholson & Grist, 2001; Nicholson, 2008; Sathiyamoorthy, 2005).

A stronger (weaker) TEJ has been linked to wetter (drier) conditions in the Sahel (Grist & Nicholson, 2001; Hulme & Tosdevin, 1989; Nicholson, 2008), Ethiopia (Segele et al., 2009) and India (Pattanaik & Satyan, 2000) as well as decrease (increase) in cyclone events in Bay of Bengal (Rao et al., 2004). Its role on rainfall in equatorial Africa is prominent in both boreal spring and autumn, which in turn impacts the mean climate of West Africa (Besler, 1984; Flohn, 1964; Webster & Fasullo, 2003). The jet is present across the east-west extent of Africa and has a mean speed of about $30ms^{-1}$ during August of some wet years over the Sahel (Nicholson, 2013). Drier conditions emerge in the Sahel because of diminished speed and spatial extents of the TEJ between the 1950s and 1990s (Nicholson & Grist, 2001; Rao et al., 2004; Sathiyamoorthy, 2005). Also, the jet is found to correspond with cooler upper-troposphere tropical temperatures and latitudinal temperature gradients (Nicholson, 2008).

Nicholson & Grist (2003) presented a clear link between TEJ and rainfall around the upper-level divergence associated with the jet core. The divergence was described to emanate from strong meridional components associated with the TEJ over Africa. Existing relationship between the AEJ and TEJ is that, a more equatorward position of the AEJ over the Sahel corresponds with dry/drought conditions (Jenkins et al., 2005; Nicholson, 2008) while a stronger than average TEJ often results in wetter climate, but from a regional climate model, it is revealed that all displacement of AEJ may not be associated with wetter or drier Sahel (Sylla et al., 2013).

2.1.3 African Westerly Jet

Grist & Nicholson (2001) was the first to describe the African Westerly Jet (AWJ). Though it does not appear in all years, it develops mostly during the wet years in the Sahel. When it emerged in the late boreal summer (July to September) the mean speed of the jet is about $10ms^{-1}$ and can extend well into the mid-troposphere. This jet, however, disappears in dry years as indicated by the monthly mean and wind shifts to easterly above the 850hPa level. Also, in the presence of the AWJ the westerly range between $2\text{-}4ms^{-1}$ and its maximum resides in the monsoon layer at about 925hPa. The AWJ is not part of the southwest monsoon flow rather its core is well above the monsoon layer (Nicholson & Grist, 2003). During the height of the rainy season in the Sahel, in August, the core speed of the AWJ is well correlated with the surface pressure gradient between the latitude of 20^oS and 20^oN (Nicholson & Grist, 2003). The source of the jet is linked to inertial instability that develops in response to this pressure gradient, which enhances both the jet and rainfall (Nicholson & Webster, 2007; Tomas & Webster, 1997).

2.1.4 West African Westerly Jet

This jet is described to appear as a near-surface wind maximum over the equatorial Atlantic and prevails from May to September (Grodsky et al., 2003). The jet was later term West African Westerly Jet (WAWJ) by Pu & Cook (2010). It develops around 10^{o}N and resides in the region where the trade winds converge. The jet is quite different from the AWJ as it emerges at the surface in response to the mid-tropospheric westerly wind maximum and can reach speed between 10-15ms^{-1} (Grist et al., 2002). The role of this jet potentially lies in the moisture it transports from the Atlantic Ocean to the Continent within the zone of latitudes 8-11^{o}N. Though the jet does not extend to the Sahel, a study showed a strong correlation between its speed and the Sahel rainfall (Grodsky et al., 2003). The moisture transport associated with the WAWJ highly varies on a decadal-scale than that of the southwest monsoon and it may introduce moisture into the region when the monsoon is weak (Pu & Cook, 2012). Another important feature of the WAWJ is that it stabilizes the regional vorticity balance by introducing strong relative vorticity gradients (Nicholson, 2013).

2.1.5 Saharan Heat Low

The Saharan heat low, also known as the West African heat low, is a region of very high surface temperature and low pressures (Lavaysse et al., 2009). This phenomenon is a well-established intense heat low in the western Sahara that is assumed to be a passive component of the West African monsoon system. It is a shallow system of thermal depression below 700mb (Lavaysse et al., 2010a). The SHL is a very important

element of the monsoon system and its variability (Nicholson, 2013). A primary link between the strength of the heat low and Sahel rainfall exist on intraseasonal (Lavaysse et al., 2010b), interannual and decadal timescales (Biasutti et al., 2009). The SHL is present throughout the boreal summer and undergoes synoptic and intraseasonal changes in intensity (Nicholson, 2013).

The SHL is suggested to be the bridge between the midlatitudes and West African monsoon (Chauvin et al., 2010). It displays a strong seasonal migration starting from a location south of Darfur mountains during November to March and thereafter migrates northwestward to a location in the western Sahara during late June to September (Lavaysse et al., 2009). The SHL resides between Hoggar and Atlas Mountains 5 days before the onset of the West African monsoon in June (Nicholson, 2013). Lavaysse et al. (2010b) found strong and weak phases of the heat low. They further evaluated atmospheric circulation, temperature and convection within these phases to identify increased (decreased) convection in the central (western) Sahel in the strong phase in response to an increase (decrease) in the low-level cyclonic circulation around the heat low. Thus, Parker et al. (2005) concluded that changes in the intensity of the SHL influence the monsoon circulation further south of the region.

2.2 SOCIO-ECONOMIC IMPORTANCE OF MONSOON RAINFALL

The role of the monsoon system in providing rainfall over the West African domain is most critical to agriculture, water resource, hydro-electric power generation and other related rainfed activities of the region (Redelsperger et al., 2006; Sultan & Janicot, 2003). For example, in the agricultural sector, rainfed agriculture accounts for

almost 80% of agricultural land worldwide and provides an estimated 62% of the world's food, which makes the sector vulnerable to climatic changes (USAID, 2014). Over West Africa, the environmental and socio-economic importance of the monsoon system cannot be overemphasized. About 75% of its population actively engage in rainfed agriculture, however, only 2% of the cultivated land in West Africa is irrigated leaving 98% to be exclusively rainfed (FAO, 2009). For instance, the local crop yields over the Sudano-Sahelian zone of the region can be significantly impacted consequent to the onset of the monsoon characterized by an abrupt shift of ITCZ from 5^{o}N to 10^{o}N latitude as well as the intra-seasonal rainfall fluctuations of 15 and 40 days time scales (Sultan et al., 2005).

On the other hand, the occurrence of flood and drought that are associated with the interannual variability of the monsoon can cause significant damage to human health and well-being and the physical environment. The population of the region is fast growing and a vast majority of dwellers lives in ill-planned urban slums built on flood plains where flood occurrence could claim hundreds of lives, loss of properties and livelihoods thereby causing internal displacement of people in such areas (Dai et al., 2004; Hulme, 2001; Tall et al., 2012). Another event that emerges as a result of the monsoon variability is the drought, the absence of water. It is a complex phenomenon and very difficult to monitor because of its slow paste of emergence at different time scales and can impact many sectors of the economy. This drought can occur in four different climatological forms: i) Meteorological drought, when dry weather patterns dominate an area as it is in the case when there is monsoon rainfall amount below its normal; ii) Hydrological drought, when low water supply becomes evident most especially in reservoirs, streams, and groundwater levels, consequent to a prolonged period of the

meteorological drought; iii) Agricultural drought, when crops are adversely affected and; iv) Socio-economic drought, when the supply and demand of various commodities are affected due to the former types of drought (NCEI-NOAA, 2019). The unprecedented prolonged Sahelian drought from the early 70s to the late 80s drove peasants out of the countryside (Diagne, 2007; Pelling & Wisner, 2009). Also, drought, evident in the drying Lake Chad, is argued to be the precursor of insurgency in the Northern part of the region and herdsmen migration to the South in search for green pastures (Freeman, 2017).

2.3 MODELING OF WAM

Numerical models have however proven useful for understanding the complex interaction between the multiscale processes (Sylla et al., 2013). Most importantly, is the potential to apply these models for a better understanding of the West African climate response to global warming. Though similar simulations have been performed using Global Climate Models (GCMs), the model's horizontal resolution are typically coarse (~ =100km) and consequently, introduces some measure of uncertainties that limits the accuracy of reproducing the WAM main features (Hourdin et al., 2010; Sylla et al., 2010; Xue et al., 2010). This limitation, over the last few decades, makes the application of Regional Climate Models (RCMs) in studying the West African climate systems more significant for their higher resolution than the GCMs (Sylla et al., 2013). The high resolution of the RCMs, therefore, improves the representation of fine-scale forcing and land surface heterogeneity such as vegetation changes, complex topography, and coastlines, which reflects the physical response to global and regional climate signals (e.g. Paeth et al., 2005; Rummukainen, 2010; Sylla et al., 2013). Also, the quality of

simulation from RCMs may depend on how good the dynamical core represents the basic flow in the atmosphere (Prein et al., 2015).

The ability of the state-of-the-science RCMs to simulate the mean climatology, mean annual cycle and inter-annual variability of rainfall together with the dynamic structure associated with the monsoon rainfall of the West African region is very paramount. This skill is critical to assess relevant processes linked with the interactions between the atmosphere, land, and ocean alongside between the dynamics and convection (Sylla et al., 2013). The use of the RCMs can further improve the understanding of rainfall variability and hence, increase the ability to predict rainfall variability over the region.

2.3.1 Physical Parameterization Process

Regional climate models (RCMs) are limited-area numerical models forced at the lateral boundaries by Global climate model (GCM) outputs or reanalysis data. The RCMs can be initialized with SSTs, which are at large prescribed except in cases where the ocean model is enabled (Sylla et al., 2013). Usually, the RCMs are used to add further details to the GCM simulations or to perform study of a phenomenon that requires improved fine-scale detail over that obtained from the GCM (Filippo Giorgi & Mearns, 1999). Example of such phenomenon includes assessing the impact of land cover change, dust and biomass burning, and global warming at the regional scale.

A reflection of the impact of these unique processes results from the summation of direct physical interactions that occur within the atmosphere, ocean, and land interface. Some of the major direct physical processes considered within the RCM framework

include radiation, surface, cumulus convection, microphysics, surface and planetary boundary layer (see Figure 2.3). It is important to parameterize these physical processes in numerical models because sub-grid scale processes (that is, scales with length lesser than that of the model) are not explicitly resolved in RCM simulations mostly at a horizontal resolution greater the 4km. The processes do not act independently of each other but rather they get feedback from their responses. For instance, the radiation budget is influenced by the presence or absence of cloud, consequently reducing both the incoming shortwave and outgoing longwave radiation. Also, due to the different radiative properties of different microphysical species, the radiation budget is influenced by the relative amount, concentration and shape of the microphysical species present in the atmosphere. The surface supplies latent and sensible heat fluxes into the planetary boundary layer, which therefore defines the profile of moisture, heat and momentum with the atmospheric column. The cumulus convection process, which determines areas of instability within the atmospheric, is fed with the vertical flux information to produce convective precipitation. To avoid unrealistic precipitation activities, the excess water in the atmosphere is further removed by the microphysics parameterization as non-convective precipitation.

The most important physical parameterizations for WAM application are the cumulus convection, microphysics, and planetary boundary layer physics. The WRF model has quite several physics options with varying levels of complexities for each physics process. But, these three physics play important roles to modify the atmospheric moisture, momentum and heat distribution, and thus, their proper treatment is critical to

realistic simulation and prediction of the WAM and its dynamics (Gbode et al., 2019; Klein et al., 2015).

2.3.2 Global and Regional Modeling of WA Monsoon

Global Circulation Models (GCMs) simulations are usually at a typical grid spacing of approximately 100km. Due to this scale, they are limited in their ability to reproduce the WAM and its associated rainfall producing features such as AEWs, AEJ and TEJ. As earlier stated, one of the main purposes for using a limited area model (e.g. RCMs) is basically to add-value to individual and/or multi-model RCMs ensemble as against their forcing GCM or reanalysis field. Several studies have extensively employed RCMs to dynamically perform downscale experiments with applications for West Africa (Afiesimama et al., 2006; Diallo & Sylla, 2012; Gallée et al., 2004; Gbode et al., 2019; Hagos & Cook, 2007b; Kamga & Buscarlet, 2006; Klein et al., 2015; Nikulin et al., 2012; Noble et al., 2014, 2017; Paeth et al., 2005; Pal et al., 2007; Pohl & Douville, 2011b, 2011a; Vizy & Cook, 2002). Most of these studies showed that RCMs can adequately represent the WAM climatology and its variability however, with some localized systematic error.

The RCMs are a useful tool for understanding WAM dynamics alongside its interaction between different components. Application of a single RCM has revealed unpredictable and large random errors that significantly influence the simulation at shorter time scales (Vanvyve et al., 2008), which can be improved upon by appropriate selection of the model physics options (Gbode et al., 2019; Klein et al., 2015). This limitation has led to significant efforts to establish coordinated frameworks using different RCMs to improve the reproduction of WAM characteristics at various

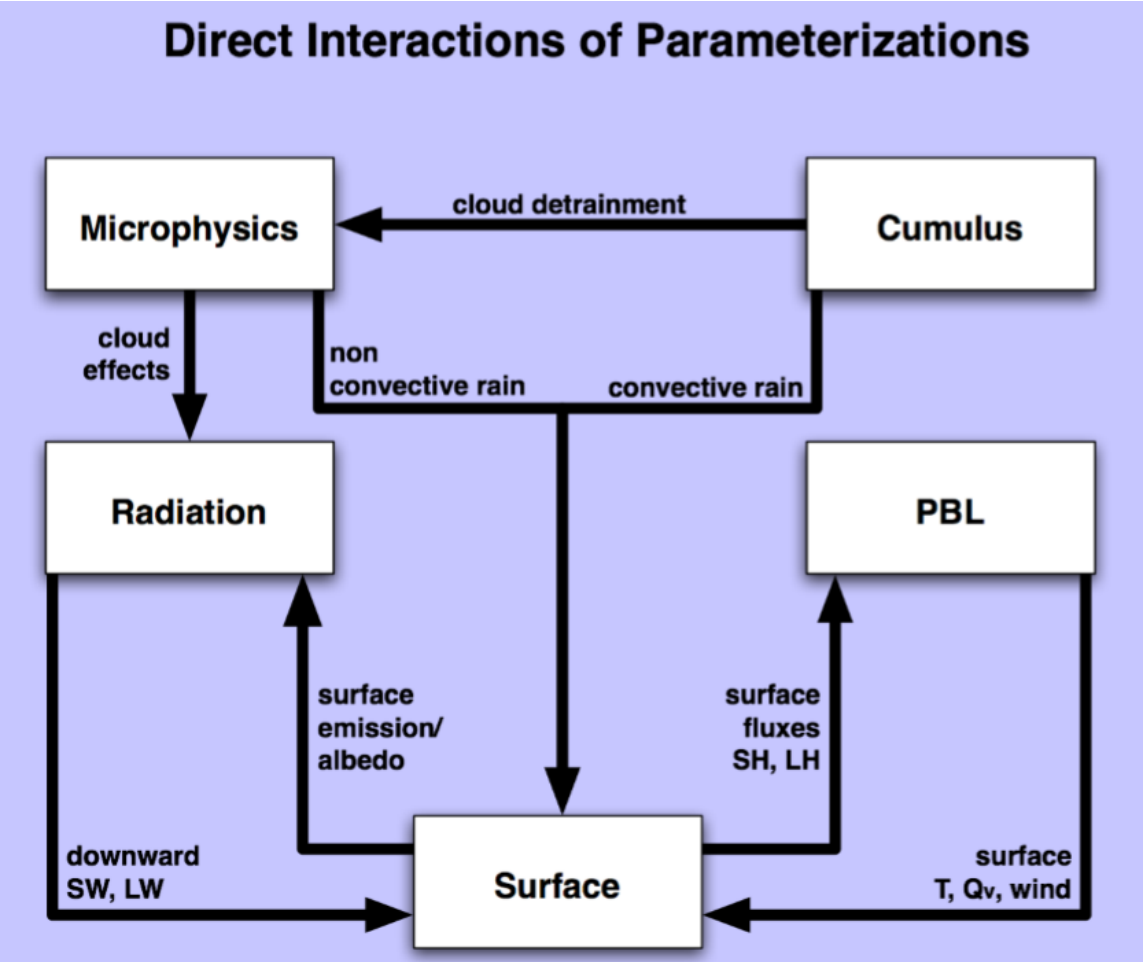

Figure 2.3: Direct Interactions between Physical Parameterizations within Numerical Models (Source: Dudhia, 2010)

time-scales. Example of such frameworks include the West African Monsoon Modelling and Evaluation (WAMME and WAMME II, Druyan et al., 2010; Xue et al., 2016, 2010), African Multidisciplinary Monsoon Analysis (AMMA, Hourdin et al., 2010), the Ensemble-based Prediction of Climate Change and their Impacts (ENSEMBLES, Paeth et al., 2011) and the Coordinated Regional Downscaling Experiment (CORDEX, Giorgi et al., 2009).

In all these frameworks the potentials of the WRF model is yet to be extensively explored. Only the CORDEX framework (Nikulin et al., 2012) examined a few of the numerous physics options present in the WRF model. As mentioned earlier, the model has several options that can be combined in multiple ways to simulate a specific atmospheric phenomenon.

Some studies have employed the WRF model over the region to understand the WAM variability and its associated rainfall producing features. For example, Flaounas et al. (2011) examined the impact of some physical schemes using the WRF model in regional climate mode. They reported that the effect of Planetary Boundary Layer (PBL) schemes is strongest on temperature, vertical distribution of humidity and rainfall amount and that the dynamics and precipitation variability is strongly influenced by the cumulus (CU) parameterization schemes. Furthermore, they found Mellor-Yamada-Janjić (MYJ) PBL was found to produce more realistic humidity, temperature, and WAM onset when combined with Kain-Fritsch (KF) CUs. The different combinations, used in Flaounas et al. (2011), however, revealed the role of different regional climate features in the dynamics of WAM. In another study, Li et al. (2015b), biases in radiation fluxes that originate from radiation physics influence radiative forcing and the spatial distribution

and intensity of WAM precipitation. Likewise, different radiation treatments reproduced different meridional surface temperature gradients between the Sahel and Guinea coast, a major driver of the WAM. This variation affects the position of both the AEJ and low-level monsoon inflow from the Gulf of Guinea coast. Noble et al. (2014) showed that Grell-Devenyi CU has a stronger linear relationship than KF CU in its ability to reproduce vorticity maxima associated with the AEW. The Grell-Devenyi scheme was also shown to perform relatively well in simulating the westward-propagating precipitation maxima associated with AEW (Noble et al., 2017).

Klein et al. (2015) used a multi-physics ensemble approach to reproduce the WAM and purported that both microphysics (MP) and PBL have significant contributions to the ensemble spread of monsoon precipitation over West Africa. Moreover, the PBL was found to impact more on cloud fraction and thus have a stronger influence on the movement of the monsoon rainband. These studies underscored the crucial role of physical parameterization in the simulation of WAM and the difficulty in the model setup giving that there are numerous available parameterization schemes in the WRF model. The complexity in the model setup underscores the need for having the best physics combination as presented in earlier studies (Flaounas et al., 2011; Noble et al., 2014). Further, conclusions from these studies, however, emphasized that any kind of physics evaluation is subjective and largely depends on the verification techniques, the region of focus, and variables of interest.

2.4 IMPACT OF WARMING ON MONSOON

Since the beginning of the industrial era, the Earth's surface has been exposed to warming consequently to the increasing rate of anthropogenic greenhouse gas emissions produced from the burning of fossil fuels and large-scale deforestation. The increased human-induced greenhouse gas concentration, mostly carbon dioxide, has been reported to alter the global atmospheric composition and thereby resulting in an increase in the amount of heat energy trapped near the Earth's surface which leads to enhanced surface temperature. This warming effect is expected to accelerate dramatically even up to the end of the 21st century, which could potentially incite significant climate modification especially in the large-scale atmospheric circulation and in the hydrological cycle (IPCC, 2001, 2007, 2018).

As mentioned earlier, the West African monsoon is a climatological feature that brings a significant amount of rainfall to the region. It is therefore important to assess the impact of climate change on the monsoon region with a focus on water resources and local subsistence economies based on agriculture. Generally, in Africa, agriculture and food production are extremely localized in nature and national scale food production is mostly based on subsistence production in which community members use local practices to produce and preserve food. Thus, if global climate change impact is evident on the local agriculture practice of the region, it will further result to a direct effect on the health and well-being and livelihood of its dwellers as well as the ecosystems of local communities (Maynard et al., 2002; Rowlands, 1996). This emphasis the need to evaluate the impact of global warming on these regions with a focus on the factors of the hydrological cycle (Rind et al., 1990).

Findings from previous studies emphasized the significant role land surface conditions play on rainfall variability over West Africa. Therefore, it is expected that the monsoon is sensitive to global warming. In an analysis of greenhouse gas impact on the African continent, Hulme (1994) combined results from seven GCMs, using greenhouse gases forcing only, to characterize the impact of global warming on temperature and precipitation. The study reported a significant warming over the continent and a tendency for much of the continent to sustain more precipitation. Nikulin et al. (2012) also assessed the impact of effects of 1.5 and 2 degrees of Global Warming Levels (GWLs) on Africa in the CORDEX ensemble under representative concentration pathway 8.5 (RCP8.5). Their study reported wetter conditions in terms of annual mean precipitation in some parts of central/eastern Sahel and eastern Africa but with low model agreement on the sign of change. Further, they found a consistent increase in daily precipitation intensity of wet days over a large fraction of tropical Africa surfaced at 1.5◦C and enhanced at 2◦C. Another study by Klutse et al. (2018), stressed that enhanced warming could potentially result in reduced mean rainfall across the West African region. Also, their study showed projected increase in consecutive dry days (i.e. days with precipitation less than 1mm) and a decrease in consecutive wet days (i.e. days with precipitation equal to or greater than 1mm) over the Guinea Coast at both 1.5◦C and 2◦C global warming levels. These projected changes can further impact the already fragile ecosystems and agriculture in the region.

2.5 GREENHOUSE GAS SCENARIOS

A Special Report on Emissions Scenarios (SRES) was developed by the Intergovernmental Panel on Climate Change (IPCC, 2000) as part of its mandate to assess the state of the global climate system. The SRES presented scenarios, which have been widely used in the analysis of possible climate change and its impacts. Four different narrative scenarios (A1, A2, B1, and B2) were developed to describe consistently relationships between emission driving forces and their evolution (Maynard et al., 2002). Each scenario represents a different demographic, social, economic, technological, and environmental development. These scenarios were subjected to either positive or negative criticism from some people across different social class. The B2 scenario family describes a world in which emphasis is on local solutions to economic, social and environmental sustainability. It is a world with a continuously increasing global population at a rate lower than A2, intermediate levels of economic development, less rapid and more diverse technological change than in B1 and A1. While this scenario is also oriented toward environmental protection and social equity, it focuses on local and regional levels. For these reasons, the marker scenario B2 was chosen for simulations of future climate with the coupled system (Maynard et al., 2002).

In 2014, Intergovernmental Panel on Climate Change (IPCC) adopted a Representative Concentration Pathway (RCP), a greenhouse gas concentration (not emissions) trajectory, for its fifth Assessment Report (AR5). This then supersedes the Special Report on Emissions Scenarios (SRES) projections published in 2000. In this report, another four pathways were selected for climate modeling and research. These pathways describe different future climate situations, all of which are considered possible

depending on how much greenhouse gases are emitted in the years to come. The four RCPs include RCP2.6, RCP4.5, RCP6, and RCP8.5 and are categorized based on the possible range of radiative forcing values in the year 2100 (2.6, 4.5, 6.0, and 8.5 W/m^2, respectively). The RCPs presents a consistent range of possible changes in future human-induced greenhouse gas (GHG) emissions and aim to represent their atmospheric concentrations (Collins et al., 2013). The RCP 2.6 assumes that global annual GHG emissions (measured in CO2-equivalents) peak between 2010 and 2020 (see Figure 2.4) thereafter with emissions declining substantially (Meinshausen et al., 2011). For RCP 4.5 emissions peak around 2040, then decline (Meinshausen et al., 2011). RCP 6.0 assumes GHG emissions peak around 2080, then decline. And lastly, in RCP 8.5 it is assumed that emissions continue to rise throughout the 21st century (Meinshausen et al., 2011).

Even though the RCPs have been categorized in terms of inputs, a major concern is that the RCPs ignore the carbon cycle by focusing on concentrations of greenhouse gases, not greenhouse gas inputs (Collins et al., 2013). The IPCC assessment separately studied the carbon cycle which predicts higher ocean uptake of carbon corresponding to higher concentration pathways, but land carbon uptake is much more uncertain due to the combined effect of climate change and land-use changes (Collins et al., 2013). The four RCPs are however consistent with certain socio-economic assumptions but are to be substituted with the shared socio-economic pathways which are anticipated to provide flexible descriptions of possible futures within each RCP. The RCP scenarios are, however, based on similar socio-economic models as those used to develop the SRES scenarios (Ward et al., 2012).

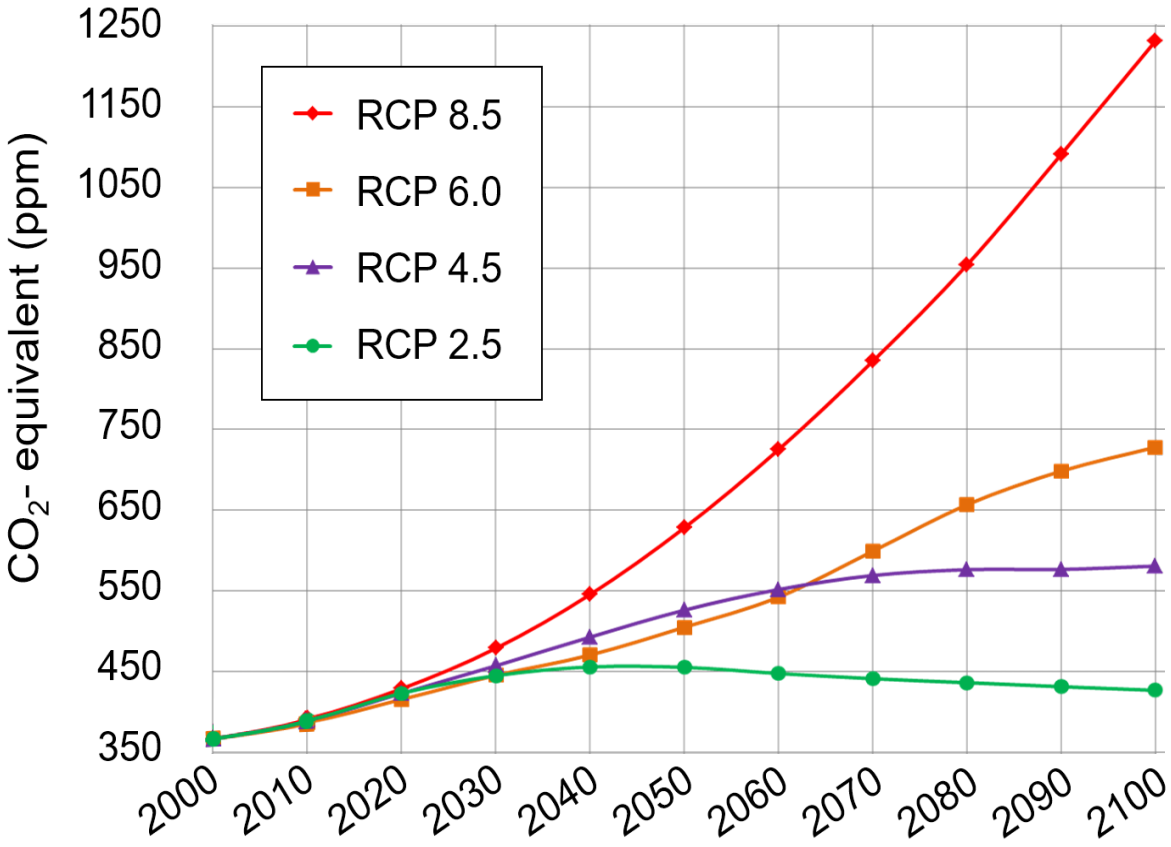

Figure 2.4: Representative Concentration Pathways (RCPs) from the Fifth Assessment Report by Intergovernmental Panel on Climate Change (IPCC AR5; Collins et al., 2013)

2.6 GAP IN LITERATURE

Most West African communities are challenged with various degrees of risk associated with climate change and variability. A way of understanding how great climate change and variability impacts the region's environment and economy is through quality scientific researches. Long-term observations and measurements of weather and climate parameters such as temperature, rainfall, relative humidity, winds speed and direction as well as their derivatives are critical to indicating changes in climate. Observation networks in West Africa are very sparse and the paucity of data makes it very difficult to understand the underlying drivers of climate change and variability. Alternatively, the emergence of reanalysis datasets and satellite products since the last 5 decades has helped to improve the understanding of some atmospheric processes. Though reanalysis and satellites products have contributed immensely to revealing certain facts in atmospheric research, they cannot answer the question about how the region's climate system will respond to potential future changes, therefore, the need for climate models.

Climate models are useful tools that can be used to simulate different atmospheric phenomena (Sylla et al., 2013). The model can be used to perform a diagnostic (historical) or prognostic (future) assessment of atmospheric processes at different temporal and spatial scales. However, the available climate models are not perfect due to large uncertainties that are introduced through either the forcing data, parameterization of sub-grid scale processes, model domain, spin-up, model dynamics or to some extent the computational resources used. These uncertainties may not be completely eradicated but can be reduced to make the model simulations closer to reality, therefore, continuous model development is required as new techniques and technology emerges. The

uncertainties in climate models are of great concern within the scientific community as researchers have attempted to address the issues and research are still ongoing to reduce model biases. These biases have greatly limited the uptake of model-derived information in decision support systems.

Furthermore, existing researches are yet to identify regional climate model whose output can be used as an integral input to provide sound climate information that will guide policy formulation and decision-making in climate-related sectors of the economy at the national and regional scale. Model development, evaluation, and application are most vital areas that have been explored in the past and present-day researches; nonetheless, these aspects of research are yet to be fully mature, most especially in data-sparse region like Africa. It is therefore critical to constantly evaluate the available model physics options, which are subjected to modifications and regular updates. Also, there are still deficiencies in meeting the increasing demand for reliable simulation of the monsoon system because of its influence on physical, chemical and biological environment, which in turn affects life in nations of the West African region and globally (Janicot et al., 2008; Mounier et al., 2008; Redelsperger et al., 2006). This challenge is exacerbated by the limited availability of dense surface and upper air observation data networks that restrict our understanding of the large-scale monsoon system and its associated rainfall-producing features.

Though previous studies have provided substantial information as regards model improvement and the sensitivity of WAM to model physics and configuration, most of the results still contain large uncertainties owing to the inherent systematic biases. Therefore, the importance of this research to further improves the simulation of vital

atmospheric processes. Also, the role of the monsoon in producing rainfall for the region strengthens the above argument. Hence, the need for the current study to consolidate on previous work by providing a comprehensive evaluation of more robust model physics combination with a major focus on improving WAM simulation.

CHAPTER THREE

DATA AND METHODS

3.1 DESCRIPTION OF STUDY AREA

The United Nations defines Western Africa as the 16 countries of Benin, Burkina Faso, Cape Verde, The Gambia, Ghana, Guinea, Guinea-Bissau, Côte d'Ivoire, Liberia, Mali, Mauritania, Niger, Nigeria, Senegal, Sierra Leone, and Togo. West Africa occupies an area of 6,140,000 km^2, which is approximately one-fifth of the African continent (Speth et al., 2010). The region can be divided into three (3) different climatic zones (see Figure 3.1); Guinea Coast (4-8°N), Savannah (8-11°N) and Sahel (11-16°N), based on similarities in land use/land cover, climate and ecosystems (Abiodun et al., 2013; Omotosho & Abiodun, 2007; Iloeje, 1981). These zones are strongly influenced by the West African monsoon, which provides most of the rains for agricultural and other rainfall-dependent sectors of the economy of countries lying within these zones.

The Guinea Coast (4°-8°N) is located in the southern part of the region and is characterized by a sub-humid climate with an average annual rainfall ranging from about 1575-2533 mm (Gbode et al., 2015; Oguntunde et al., 2011). To the north, from 8° to 11°N, is the Savannah zone, which is a semi-arid region with average annual rainfall of about 897-1535 mm. Rainfall reduction in this zone is as a response to the monsoon jump, which is the observed abrupt latitudinal shift of maximum precipitation from the Guinea coast into the Sahel region around June (Hagos & Cook, 2007b; Lebel et al., 2003; Le Barbé et al., 2002; Sultan & Janicot, 2000). The non-linear northward shift of the rainfall belt, therefore, paves way for the "little dry season" between July and August along the Guinea coast. The Sahel zone (11°-16°N) covers the northern part of the region

and is characterized by a single peak rainfall season spanning from July to September with a maximum in August which coincides with the northernmost position of the Inter-Tropical Discontinuity (ITD) at about 21°-22° N latitudes (e.g. Nicholson, 2013). The average annual rainfall over the region ranges between 434 and 969 mm (Gbode et al., 2015; Oguntunde et al., 2011).

The model domain is centered on the West African region (latitudes 0°–20° N and longitudes 20°W–20° E; bigger red box in Figure 3.2) and sufficient area of the Atlantic Ocean, which serves as the major source of moisture carried into the region by the monsoon flow. The horizontal grid size is 20 km and the center is at latitude 12.5° N and longitude 0°.

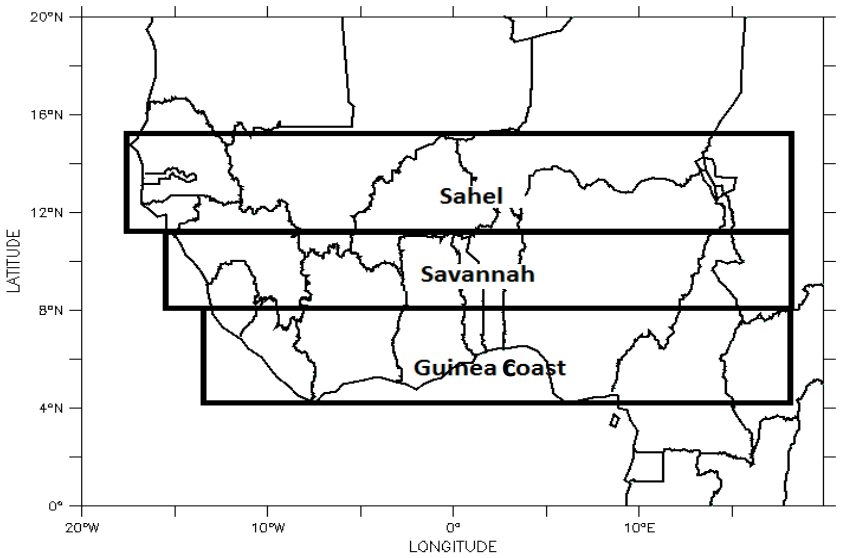

Figure 3.1: Map of West Africa showing the different Climatic Zones Adapted from Omotosho & Abiodun (2007)

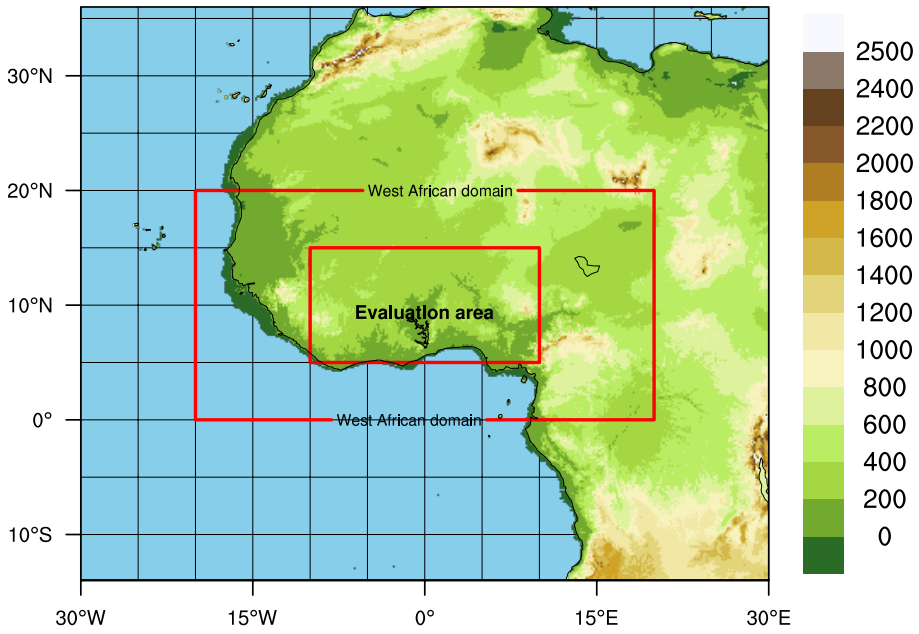

Figure 3.2: WRF Model Computational Domain with Topographic Elevation Contours at 200 m Intervals.

NOTE: The outer red box outlines the West African region while the inner box outlines the area used for precipitation and surface temperature evaluation. The outer red box outlines latitudes 0°–20° N and longitudes 20°W–20° E while the inner red box delineates the evaluation region of latitudes 5°–15° N and longitudes 10°W–10° E.

3.2 OBSERVATION AND REANALYSIS

West Africa is one of the data-sparse regions where conventional rain gauge and synoptic weather station network remain inadequate for validating the spatiotemporal distribution of the model results. Therefore, the skill of precipitation simulation is assessed using Satellite Rainfall Products (SRPs) from Tropical Rainfall Measurement Mission (TRMM; Huffman et al., 2007), Climate Prediction Center (CPC) MORPHing technique (CMORPH; Joyce et al., 2004), and Global Precipitation Climatology Project (GPCP; Huffman et al., 2016, 2009). The SRPs were interpolated at 1° × 1° resolution using the first-order conservative remapping method (Jones, 1999), which conserves the mean pattern of the highly variable rainfall products. The reliance on the precipitation verification analysis must be made with caution because of the differences between SRPs (Noble et al., 2017; Sylla et al., 2013) consequent to their retrieval platforms and different algorithms used in producing them. However, the high temporal and spatial (3 hourly and 0.25° resolution) Tropical Rainfall Measurement Mission (TRMM) 3B42 product is one of the reliable sources for merged high-quality precipitation estimates (Huffman et al., 2007) and it is therefore used as the standard for evaluating the model outputs in the sensitivity study. Global Precipitation Climatology Project 1° Daily (GPCP 1dd) is another reliable SRP produced from optimized merged estimates computed from microwave, infrared, and sounder data observed by the international constellation of precipitation related satellites and precipitation gauge analysis (Huffman et al., 2016, 2009). Also, the model results are compared with the CMORPH global precipitation analyses produced at a high spatial and temporal resolution similar to that of TRMM.

Also, for the sensitivity study, reanalyzed surface air temperature products including European Center for Medium-Range Weather Forecasts Re-Analysis (ERA-Interim), National Center for Environmental Prediction (NCEP), Modern-Era Retrospective analysis for Research and Applications (MERRA; Rienecker et al., 2011), and Global Surface Air Temperature (GSAT; ensemble of ERA, NCEP, and MERRA), interpolated at 0.5°×0.5° resolution, are used to validate the model surface temperature. The GSAT is bias-corrected using both monthly mean maximum (Tmax) and minimum (Tmin) of the Climate Research Unit Time Series version 3.10 (CRU TS3.10) data (Wang & Zeng, 2014).

Other model fields such as the moisture, temperature, and atmospheric circulation are compared with the National Center for Environmental Prediction - Department of Energy (NCEP–DOE) Atmospheric Model Intercomparison Project (AMIP-II) reanalysis (R-2) datasets (NCEP-DOE AMIP R2, Kanamitsu et al. (2002), hereafter NCEP). The NCEP is available in 2.5^{o} x 2.5^{o} horizontal resolution at 17 vertical pressure levels. It consists of omega, zonal and meridional winds, specific humidity and temperature data among others. Though, the difference in NCEP reanalysis II is much smaller from that in NCEP Reanalysis I (Kalnay et al., 1996), it contains improvements through error fixes and parameterization updates (Kanamitsu et al., 2002).

3.3 MODEL SETUP FOR THE SENSITIVITY STUDY

This section presents the approach employed in performing the sensitivity test of the WRF model physics options in simulating the West African monsoon. A detailed

description of how the first objective of the current research was performed is described here.

3.3.1 WRF Model Configuration

This study used the WRF model (version 3.8.1 released in 2016) to simulate a 2-month regime of WAM from August to September in 2007, which was observed to be a normal monsoon year. During this regime, the WAM is fully developed in August and consistent with the Saharan heat low over land and the highest pressures in southern tropical Atlantic. This interaction brings about widespread rainfall in the monsoon domain. Thereafter, the westerly wind speed drastically decreases with no significant change in the area of westerly wind in September (Janicot et al., 2008). Another set of simulations was done using the later version 3.9 of the WRF model to test the newly modified Grell-Freitas CU scheme (hereafter, nGF).

The initial and lateral boundary conditions are from ECMWF Interim Re-Analysis (ERA-Interim) at a horizontal resolution of 0.75° (Dee et al., 2011) and 1° resolution National Centers for Environmental Prediction (NCEP) final analysis (FNL) initial soil data (sea surface temperature, soil moisture, and temperature) from the NCAR's Computational and Information Systems Laboratory Research Data Archive (CISL RDA; NCEP-FNL, 2000). The reason for using the FNL soil data is that it is more consistent with the soil layers and scheme of the unified Noah land-surface model used. In this study, the first 5 days were used as spin-up, so only 6 August to 30 September 2007 was analyzed.

3.3.2 Physics Options

A total of 27 runs were produced from the combinations of two microphysics, six cumulus convection, and three planetary boundary layer schemes (see Table 3.1 for references). The WRF model has quite several options with varying levels of complexities for each physical process. These three physics play important roles to modify the atmospheric moisture and heat distribution, and thus, their proper treatment is critical to realistic simulation and prediction of the WAM and its associated dynamics. The selected schemes are widely used within the WRF community and have been shown to perform well over different regions. Other physics like the unified Noah land-surface model scheme (Chen & Dudhia, 2001) and Rapid Radiative Transfer Model (RRTMG) schemes (Iacono et al., 2008) were kept constant in all simulations.

The WSM5 microphysics (MP) is a five-class scheme that accounts for hydrometeors such as vapor, cloud ice, cloud water, rain and snow, but allows no supercooled water and has immediate melting of snow below the melting layer, whereas the Goddard (GD) MP scheme is a six-class microphysics with graupel and modifications for ice/water saturation based on Lin et al. (1983). YSU Planetary Boundary Layer is a non-local closure scheme with a parameter that allows enhanced vertical mixing and entrainment of air from above the PBL even in a neutral boundary layer where the vertical gradient of potential temperature is zero (Hong et al., 2006). The YSU is a PBL scheme with stronger boundary layer top entrainment and boundary layer inner mixing than MYJ (Zhang et al., 2012). MYJ is a local closure scheme that predicts turbulent kinetic energy (TKE). MYNN PBL uses local TKE-based vertical mixing in the boundary layer and free atmosphere. In both MYJ and MYNN PBL the eddy diffusion coefficients are derived

from their prognostic turbulent kinetic energy TKE. KF is a mass flux type CU parameterization scheme with updrafts and downdrafts, entrainment, and detrainment of cloud, rain, ice, and snow. It has both deep and shallow convections and uses a Convective Available Potential Energy (CAPE) removal timescale closure. BMJ is a profile adjustment scheme that relaxes both deep and shallow profiles to a reference profile without explicit updraft, downdraft, or cloud entrainment. Both GF and nGF are mass flux schemes that have multiple closures, including CAPE removal, quasi-equilibrium, moisture convergence, and cloud-based ascent. The difference in both schemes is that nGF can trigger mid-level convection and its shallow convection also produces rainfall. Like the KF, the new Tiedtke (nTDK; Tiedtke, 1989; Zhang et al., 2011) is a mass flux scheme with updrafts and downdrafts. Another newly modified scheme is a CAPE removal time-scale simplified Arakawa-Schubert (nSAS) scheme that has momentum transport with a pressure term and new mass flux type shallow convection that is different from the earlier SAS CU. The 27 Physics scheme combinations tested are shown in Table 3.2. Based on the WSM5 microphysics test results, three fewer CU schemes were tested with GD microphysics.

3.3.3 Model Evaluation Method

Various evaluation statistics can be used to assess model performance. However, there is no single statistic that encapsulates all aspects of interest. It is therefore important to consider different performance statistics and to understand the type of information they might provide. In this study, a few statistics of the model outputs are computed to find the optimal physics combinations for long-term simulations. These statistics examine the

strength of the correlation, systematic error, and accuracy of the model in comparison to observation and are detailed below.

One of the statistics used is correlation coefficient (r), a measure of the strength of the linear relationship between model and observations.

$$r = \frac{1}{(n-1)} \sum_{i=1}^{n} \left(\frac{M_i - \bar{M}}{\sigma_M} \right) \left(\frac{O_i - \bar{O}}{\sigma_O} \right) \quad 3.1$$

where *O* represents Observation or Reanalysis, *M* model output, σ standard deviation, and *n* number of data points in the series.

The Mean Bias (B) is another statistics that indicates the mean over or underestimate of predictions. It has the same units as the quantities being considered.

$$B = \frac{1}{n} \sum_{i=1}^{n} (M_i - O_i) \quad 3.2$$

Lastly, the Mean Absolute Error (MAE) statistics that determine the mean error between model and observation regardless of whether it is an over or underestimate. It also has the same units as the quantities being considered;

$$MAE = \frac{1}{n} \sum_{i=1}^{n} |M_i - O_i| \quad 3.3$$

Furthermore, to compare and rank the physics performance based on their statistics a new comparative Model Skill Score (*MSS*) is defined and computed. The first step in computing MSS is to calculate time and space statistics. The space statistics were derived from the time average of the evaluation area (in Figure 3.2) and it quantify the error in the mean patterns. The time statistics are based on comparing the time series of space-averaged values within the same area and quantify errors in phase. Thereafter, the

MSS is calculated from the sum of the normalized (X_{norm}) values of time (t) and space (S) correlation coefficient (r), bias (B) and mean absolute error (MAE).

$$X_{norm} = \frac{X_i - X_{min}}{X_{max} - X_{min}} \qquad \textbf{3.4}$$

$$\text{Such that} \quad 0 \le X_{norm} \le 1$$

Where X could be either time or space averaged r, |B| and MAE, and X_{min} and X_{max} are defined by the worst and best of the 27 compared simulations, respectively.

$$MSS = Sr_{norm} + (1 - |B|_{norm}) + (1 - SMAE_{norm}) + tr_{norm} + (1 - tMAE_{norm}) \qquad \textbf{3.5}$$

$$where \qquad |B|_{norm} = S|B|_{norm} = t|B|_{norm}$$

Simulations with higher *MSS* values perform better while those with lower values have poorer performance. Each of the five normalized terms has values ranging from 0 for the worst to 1 for the best, so the scores for a given variable range between 0 and 5.

Table 3.1: Choice of Regional Physics Parameterization Schemes Used in the Study

Serial	Microphysics (MP)	Planetary Boundary Layer (PBL)	Cumulus convection (CU)
1	WRF single moment 5 (**WSM5**; Hong et al., 2004)	Yonsei University (**YSU**; Hong et al., 2006)	Kain-Fritsch (**KF**; Kain, 2004),
2	Goddard (**GD**; Tao et al., 1989)	Mellor-Yamada-Janjic TKE (**MYJ**; Janjić, 1994)	Betts-Miller-Janjic (**BMJ**; Janjić, 1994, 2000)
3		Mellor-Yamada- Nakanishi-Niino 2.5 level TKE (**MYNN**; (Nakanishi & Niino, 2004, 2006)	Grell-Freitas (**GF**; Grell & Freitas, 2014)
4			New Tiedtke (n**TDK**; Tiedtke, 1989; Zhang et al., 2011)
5			New Simplified Arakawa-Schubert (n**SAS**; Han & Pan, 2011)
6			New Grell-Freitas (**nGF**; in WRFV3.9)

Table 3.2: The 27 different WRF Model Physics Combinations included in the Sensitivity Analysis.

NOTE: The combinations containing the asterisked CU scheme are runs from the newly modified Grell-Freitas in WRFV3.9.

CU / **PBL**	KF	BMJ	GF	nTDK	nSAS	nGF*	
YSU	WSM5	WSM5/GD	WSM5	WSM5/GD	WSM5/GD	WSM5	
MYJ	WSM5	WSM5/GD	WSM5	WSM5/GD	WSM5/GD	WSM5	**MP**
MYNN	WSM5	WSM5/GD	WSM5	WSM5/GD	WSM5/GD	WSM5	

3.4 MODEL SETUP FOR LONG-TERM SIMULATION OF WAM

In addition to the normal (2007) year, the study analyzes composites of wet (2008 and 2010) and dry (2001 and 2011) years simulations of West African Monsoon. The wet and dry years are identified based on their positive and negative departure from normal rainfall, respectively, that is, from the climatological mean annual rainfall (see Figure 3.3).

The model was initialized in February for each year of the five runs. Each run starts from February through to the end of October. Outputs in the initial month are however used as spin-up in all simulations and the analysis focus on March-October as well as the period June-September (JJAS) when the monsoon is fully developed over most parts of the region. Though the choice of the wet and dry years may not be all encompassing to evaluate the performance of the WRF model to reproduce WAM variability, it gives useful insights. Some useful information that can be derived from the selected monsoon years to confirm the robustness in simulating WAM is on its associated precipitation and atmospheric circulation. The monsoon composites will be used to assess the role of strong and weak atmospheric circulations and moisture fluxes that influences the behavior of the complex system.

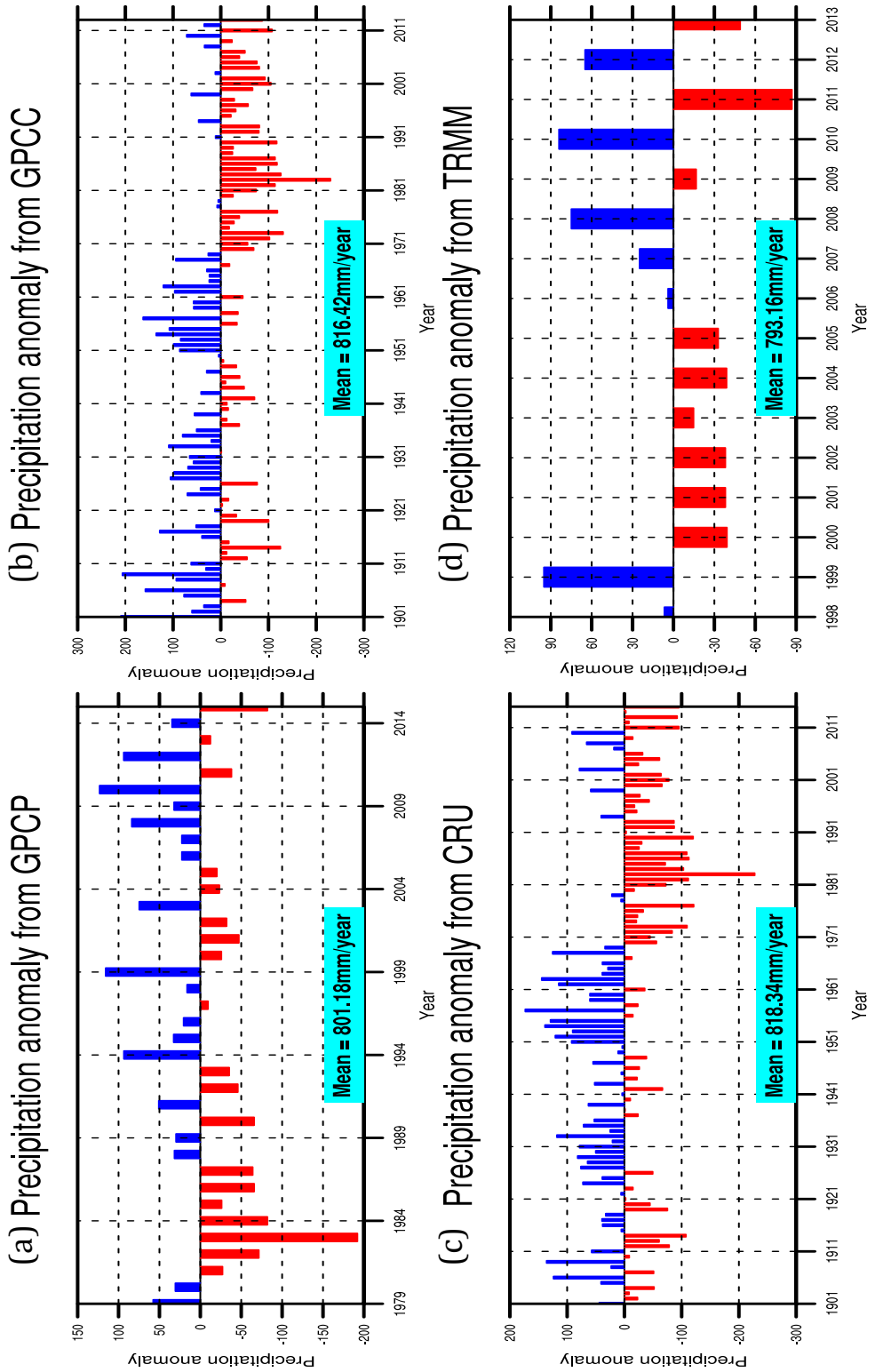

Figure 3.3: Annual Precipitation Anomaly Derived from Different Gridded Observation Datasets.

NOTE: The anomalies are computed from the climatological mean annual rainfall based on the temporal availability of (a) GPCP (1979-2015), (b) GPCC (1901-2012), (c) CRU (1901-2014) and (d) TRMM (1998-2013).

3.5 PSEUDO-GLOBAL WARMING SIMULATION SETUP

The Pseudo-Global Warming (PGW) approach is a dynamic downscaling method that permits regional climate change projections with the use of a regional climate model (Kimura and Kitoh, 2007; Sato et al., 2007; Hara et al., 2008; Rasmussen et al., 2011, 2014; Liu et al., 2017). The PGW method employs initial and lateral boundary conditions that combine 6-hourly reanalysis data and the climate change signals, which are the monthly averaged differences between the current and future climate projections produced by a global climate model (GCM). The method expects the boundary condition mean state to have similar climatology to those of the GCM future climate projections, but the daily evolution is like that of current years. The PGW technique provides the possibility of having a direct comparison between the present year and the PGW year in the context of the interannual variation with the addition of future climatology.

The objective here is to investigate the impact of global warming on precipitation in West Africa during the monsoon period. PGW method employed to directly compare future rainfall amount with that of the current.

To account for interannual variability this aspect of the current study focuses on selective five-year average precipitation. The considered years include wet (2008 and 2010), dry (2001 and 2011) and normal (2007) WAM years. The characteristics of the chosen years are determined by annual precipitation amount during March to October, which encapsulates the monsoon period. To be consistent with the greenhouse gas concentration levels, the WRF model was recompiled to reflect the estimated GHG levels for the middle year of the period 2071-2100 (Table 3.3; IPCC, 2000, 2007, 2014).

Table 3.3: Model Greenhouse Gas Concentration Levels for the Current Climate and Average Value of 2071-2100 (IPCC, 2000, 2007, 2014).

Greenhouse gas	Current	Future (RCP8.5)
Carbon dioxide (CO_2)	379 ppmv	801 ppmv
Methane (CH_4)	1774 ppbv	3564 ppbv
Nitrous oxide (N_2O)	319 ppbv	414 ppbv
Chlorofluorocarbons-11 (CFC-11)	251 ppt	86 ppt
Chlorofluorocarbons-12 (CFC-12)	538 ppt	211 ppt

NOTE: part per million volume = ppmv, part per billion volume = ppbv, and part per thousand = ppt

The numerical study includes three experiments for each present and PGW year. These experiments combines three different WRF model microphysics (MP), Planetary Boundary Layer (PBL) and Cumulus convection (CU) parameterization schemes: Goddard (GD) MP, Mellor–Yamada–Janjic (MYJ) PBL and Bett-Miller-Janjic (BMJ) CU; Weather Research and Forecasting (WRF) model Single-Moment 5-class (WSM5) MP, Mellor–Yamada–Nakanishi–Niino (MYNN) Level 2.5 PBL and new Tiedtke (nTDK) CU; WSM5, Yonsei University (YSU) PBL and new Simplified Arakawa Schubert (nSAS) CU. The choice of the selected combinations is based on results from the first objective of this research.

The first experiment was a retrospective simulation aimed to reproduce the variability and mean state of the current climate within the model domain of 20km. The current climate simulation contains selective years, including 2001, 2007, 2008, 2010 and 2011, each extending from March 01 to October 31. The present climate runs were hindcast runs using 6-hourly ERA-Interim (ERAI, Dee et al., 2011) atmospheric data with soil initialization (soil moisture and temperature) from National Center for Environmental Predictions Final Reanalysis (NCEP-FNL, 2000) (Equation 3.6). The NCEP FNL soil data was kept constant because it is consistent with the unified Noah land surface model. The choice of LSM was shown to be adequate by Gbode et al. (2019).

$$WRF_{Input1} = ERAInterim_{Atmosphere} + FNL_{Soil} \qquad \textbf{3.6}$$

The second simulation closely follows the pseudo-global warming (PGW) approach used in previous studies (Liu et al., 2017; Rasmussen et al., 2014, 2011; Hara et

al., 2008; Kimura & Kitoh, 2007; Sato et al., 2007). Though the approach may not be able to account for extreme events. It, however, allows direct comparison between the current and future climate. These selected 5-year simulations were forced with ERA-Interim, FNL reanalysis plus a climate perturbation from the Community Earth System Model version 1 (CESM1) with the Community Atmospheric Model version 5.2 (CAM5.2) of the Large Ensemble Community Project (LENS) (Kay et al., 2015) (Equation 3.7):

$$WRF_{Input2} = ERAInterim_{Atmosphere} + FNL_{Soil} + \overline{\Delta CESM1\_CAM5.2_{RCP8.5}}^{monthly} \quad \textbf{3.7}$$

where $\overline{\Delta CESM1\_CAM5.2_{RCP8.5}}^{monthly}$ is the simulated climate change signal between two 30-year time-slices (1976-2005 and 2071-2100, respectively) of the LENS 40 member ensemble-mean under the business as usual RCP8.5 scenario, a comparatively high greenhouse gas concentration trajectory (Riahi et al., 2011) with the highest radiative forcing of 8.5 W/m^2:

$$\overline{\Delta CESM1\_CAM5.2_{RCP8.5}}^{monthly} = \overline{CESM1\_CAM5.2_{2071-2100}} - \overline{CESM1\_CAM5.2_{1976-2005}} \quad \textbf{3.8}$$

The perturbed physical fields include horizontal wind, temperature, relative humidity, sea surface temperature (also known as skin temperature in FNL), and soil temperature. First, the change signals are obtained at monthly-average resolution and then these are interpolated to reanalysis times and the model grid when adding them to the analyses.

The LENS CESM1-CAM5.2 is approximately a 1^{o} latitude/longitude with CAM5.2 as its atmospheric component. CESM1_CAM5.2 is a 40-member ensemble of the LENS of fully coupled CESM1 simulations for the current (historical) and future (RCP8.5) periods 1976-2005 and 2071-2100, respectively. Each member was subjected to the same radiative forcing scenario but begins from a slightly different initial atmospheric state created by randomly perturbing temperatures at the level of round-off error (Kay et al., 2015). The ensemble average is used to remove interannual variability from the climate-change signal.

CHAPTER FOUR

RESULTS AND DISCUSSION

4.1 SENSITIVITY OF WRF MODEL PHYSICS TO WAM REGIME

This section presents and discusses the results of the sensitivity study of WRF model physics to WAM features. The purpose of this sensitivity study is to identify best performing WRF model physics combinations by evaluating the performance of the model's physics in simulating the rainfall and temperature characteristics associated with the WAM.

4.1.1 Precipitation Analysis

The diurnal cycle of precipitation is a prominent mode in the convective systems produced during the WA summer monsoon. This has been a focus of most tropical observations and climate simulations (Mori et al., 2004; Zuidema, 2003). It is suggested that modeled diurnal cycle in GCMs is too early in rainfall peak and too strong in the amplitude than observed. This weakness in describing the diurnal cycle is a matter of concern for predicting regional climate variability (Wang et al., 2007).

Figure 4.1 shows the diurnal cycle of precipitation rate averaged over latitudes 5-15^{o}N and longitudes 10^{o}W-10^{o}E for the period 6 August to 30 September 2007. Each of the stacked plots (Fig. 4.1a-f) displays the different combinations of MP and PBL physics. The black and colored lines are the Satellite Rainfall Products (SRPs) and CU simulations, respectively. Both TRMM (reference) and CMORPH SRPs are analyzed and compared with the individual simulations. The peak of diurnal precipitation of the two SRPs occurred at 18hour (Fig. 4.1) in agreement with the findings of Klein et al. (2015).

Some of the simulations reproduced diurnal precipitation peak at 15 hour earlier than the reference. The rainfall peak of nTDK, BMJ and KF occurred at 15 hour whereas that of nSAS, GF and nGF occurred same time with TRMM and CMORPH, suggesting that some CU schemes trigger earlier convective activity. The right peak simulated by some CUs underscores some success made towards a more realistic parameterization of the convective process in nSAS and nGF. However, the differences in model diurnal precipitation emphasize some of the uncertainties inherent in the representation of sub-grid scale convective processes and thus suggest the need to explicitly represent deep convection with a more realistic model dynamics (Prein et al., 2013). Further results show that nGF simulated a delay in the minimum rainfall compared with observed. When compared with other CU schemes, KF and nGF produce more precipitation during the day time and night time, respectively.

Figure 4.2 shows the daily precipitation amount averaged over latitudes 5-15^{o}N and longitudes 10^{o}W-10^{o}E for 6 August to 30 September 2007. The stacked plot is the same as that described in Figure 4.1. In Figure 4.2, the SRPs, including GPCP, precipitation phase quite agree with each other while some physics combinations simulate out of phase relative to the SRPs. For example, combinations of KF and nGFs with WSM5-YSU produced excess daily precipitation amounts for some heavy rainfall events. Other model runs give similar daily precipitation patterns as TRMM but with varying magnitudes. Also, the simulations reproduced the observed wet period in August and dry period in September.

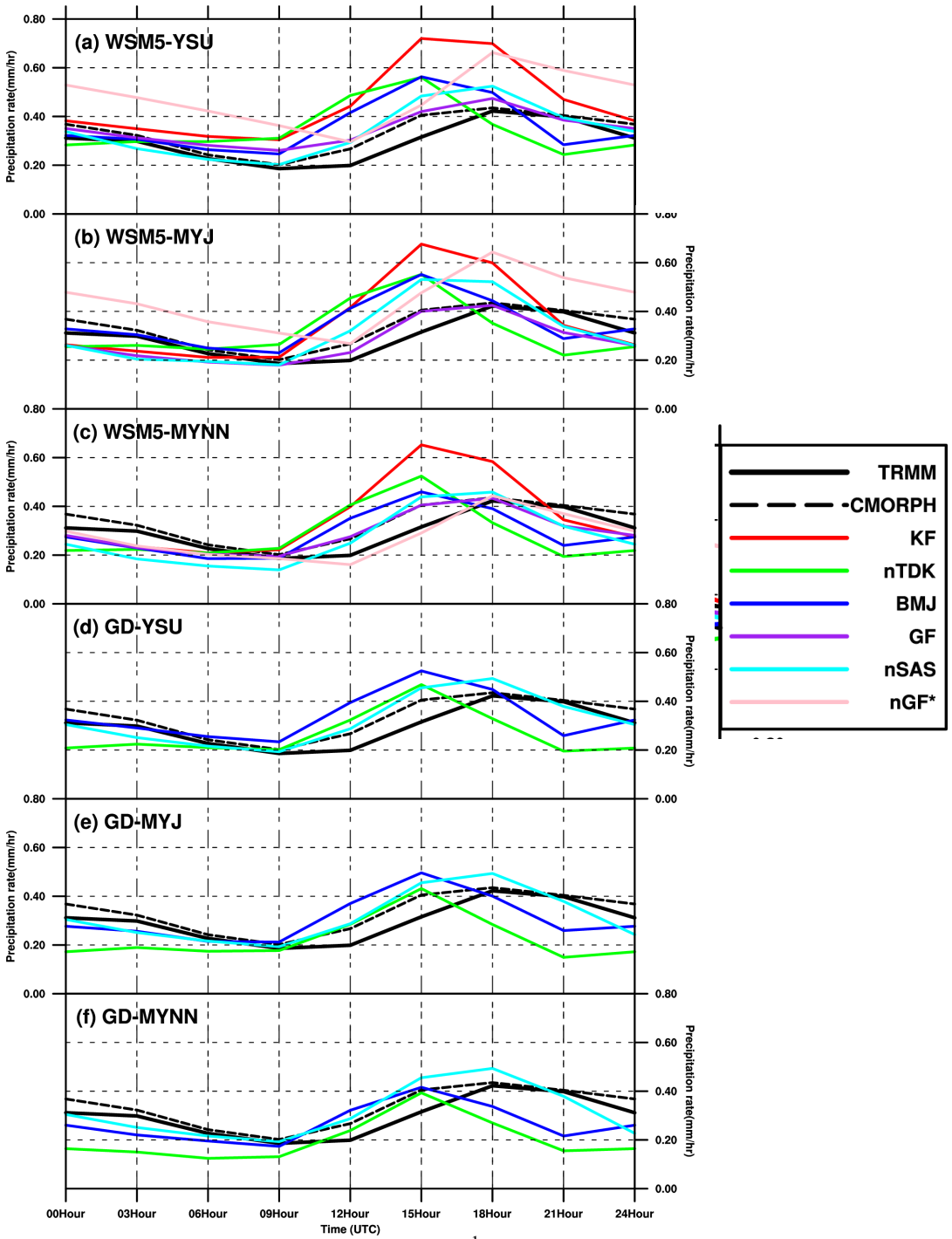

Figure 4.1: Diurnal Cycle of Precipitation (mm hr^{-1}) Averaged over the Evaluation Area (5-15°N and 10°W-10°E).

NOTE: Each stack plot represents the combinations of MP and PBL physics while the lines represents the CU physics and SRPs.

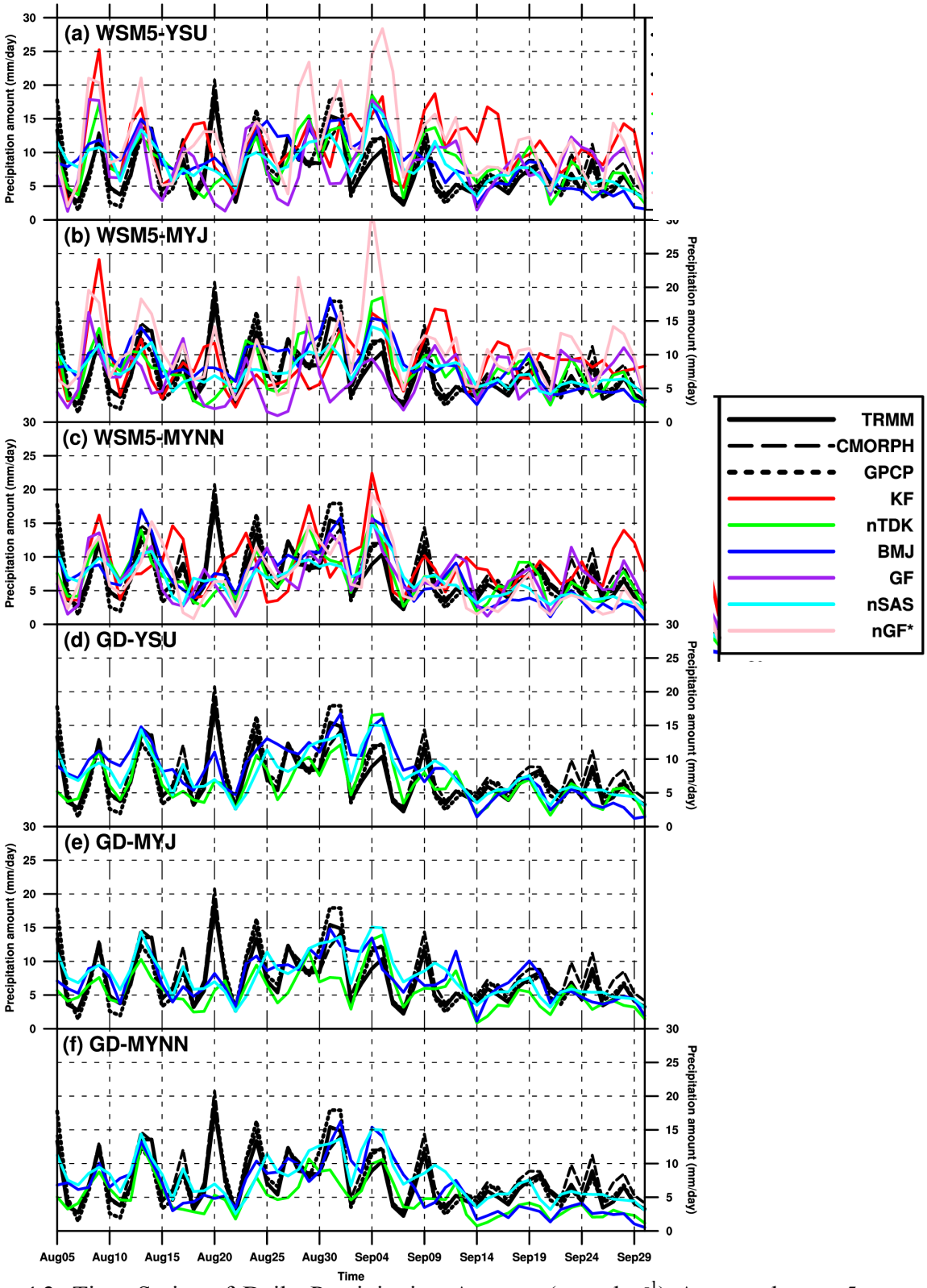

Figure 4.2: Time Series of Daily Precipitation Amount (mm day^{-1}) Averaged over 5-15^{o}N and 10^{o}W-10^{o}E.

NOTE: The stack plot is the same as described in Figure 4.1

The averaged spatial distribution of daily precipitation is presented in Figure 4.3. Only a few of the combinations that performed best relative to the CU schemes are displayed. The SRPs daily precipitation patterns agree with each other. They all showed precipitation maximum cores around the west coast of the region between latitudes 5-15^{o}N and around the Cameroun Mountain. This pattern was also found in most of the model simulations. From the results in Figure 4.3, it can be inferred that the orographic effect of the Cameroun Mountain caused the model to produce intense precipitation maximum around the area. Another agreement is evident in the reduced precipitation amount between longitudes 0-10^{o}W and northward of latitude 7^{o}N. This is pronounced in some runs with nTDK, GF, nGF and KF. The KF CU triggered strong convection and usually unrealistic precipitation events with rotational features that looked like tropical cyclones over land (not shown). This behavior in the KF runs resulted in overestimated daily precipitation amounts.

There were noticeable spatial systematic errors in all simulations (e.g. in Figure 4.4). The error, however, varies in location and magnitude. For example, KF in Figure 4.4a produced wet precipitation bias >10mm day^{-1} between 10-15^{o}N latitude band and dry bias around coastal regions. Other cumulus schemes had moderately wet and dry precipitation biases.

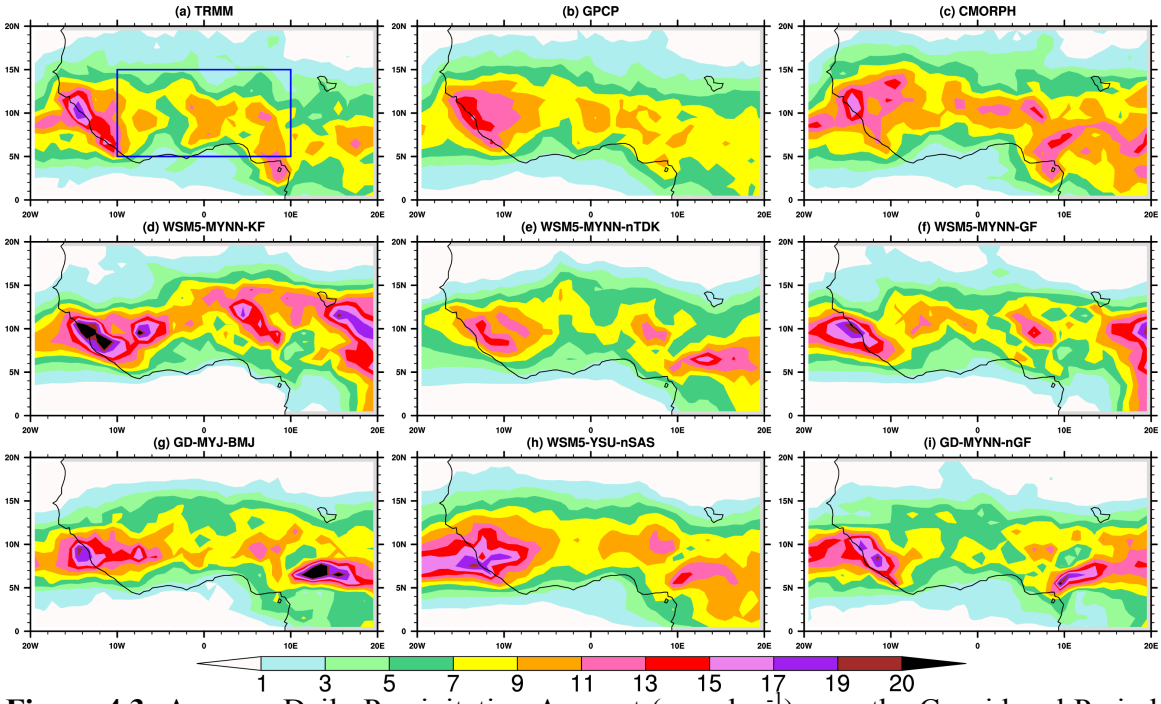

Figure 4.3: Average Daily Precipitation Amount (mm day^{-1}) over the Considered Period Aug-Sep 2007.

NOTE: The presented physics combinations are those that produce the best simulations relative to the choice of CU schemes and reference

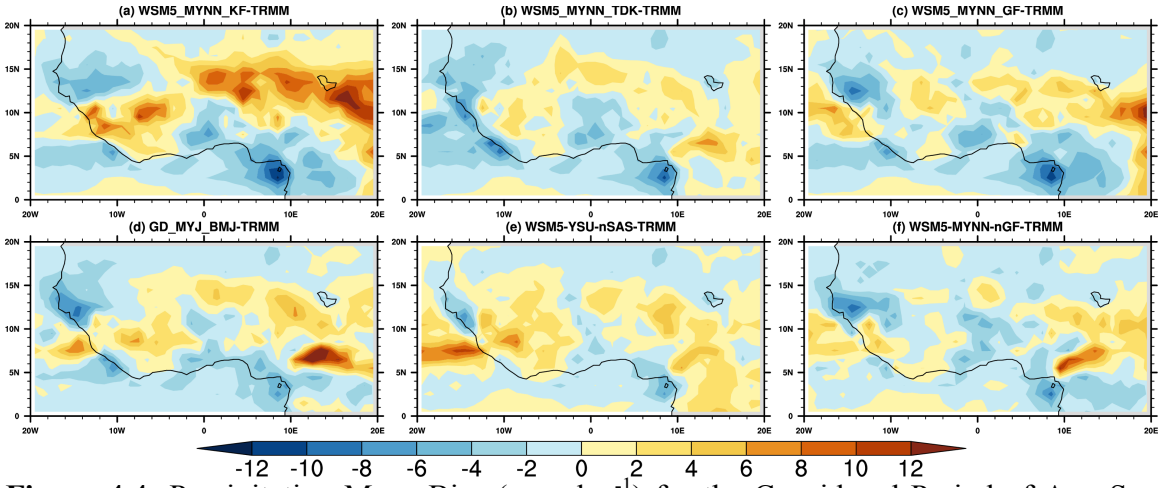

Figure 4.4: Precipitation Mean Bias (mm day^{-1}) for the Considered Period of Aug-Sep 2007

Figure 4.5 shows the time-longitude cross-section (Hovmöller) of daily precipitation that describes the westward propagation of precipitation maxima linked to the activity of the AEWs. Some studies have shown a tight coupling of convective rainfall activity with the African Easterly Waves (AEWs: Diedhiou et al., 1998; Duvel, 1990; Noble et al., 2017; Thorncroft & Blackburn, 1999). All SRPs show more active westward-propagating maxima associated with AEWs in August and less in September. Also inherent in the models is the westward movement of the precipitation maxima but the phase may differ. The AEWs are found to be active all through the considered period in KF and GF but the reduction in the wave activity towards the end of the simulation is more realistic in nTDK, BMJ and nGF. In BMJ, the waves are less organized and appear more like episodic events but nTDK, nSAS and nGF show well-structured linear westward propagation of the precipitation maxima. Similar patterns of well-defined active westward propagation of precipitation maxima in August occur for TRMM, GPCP and CMORPH data.

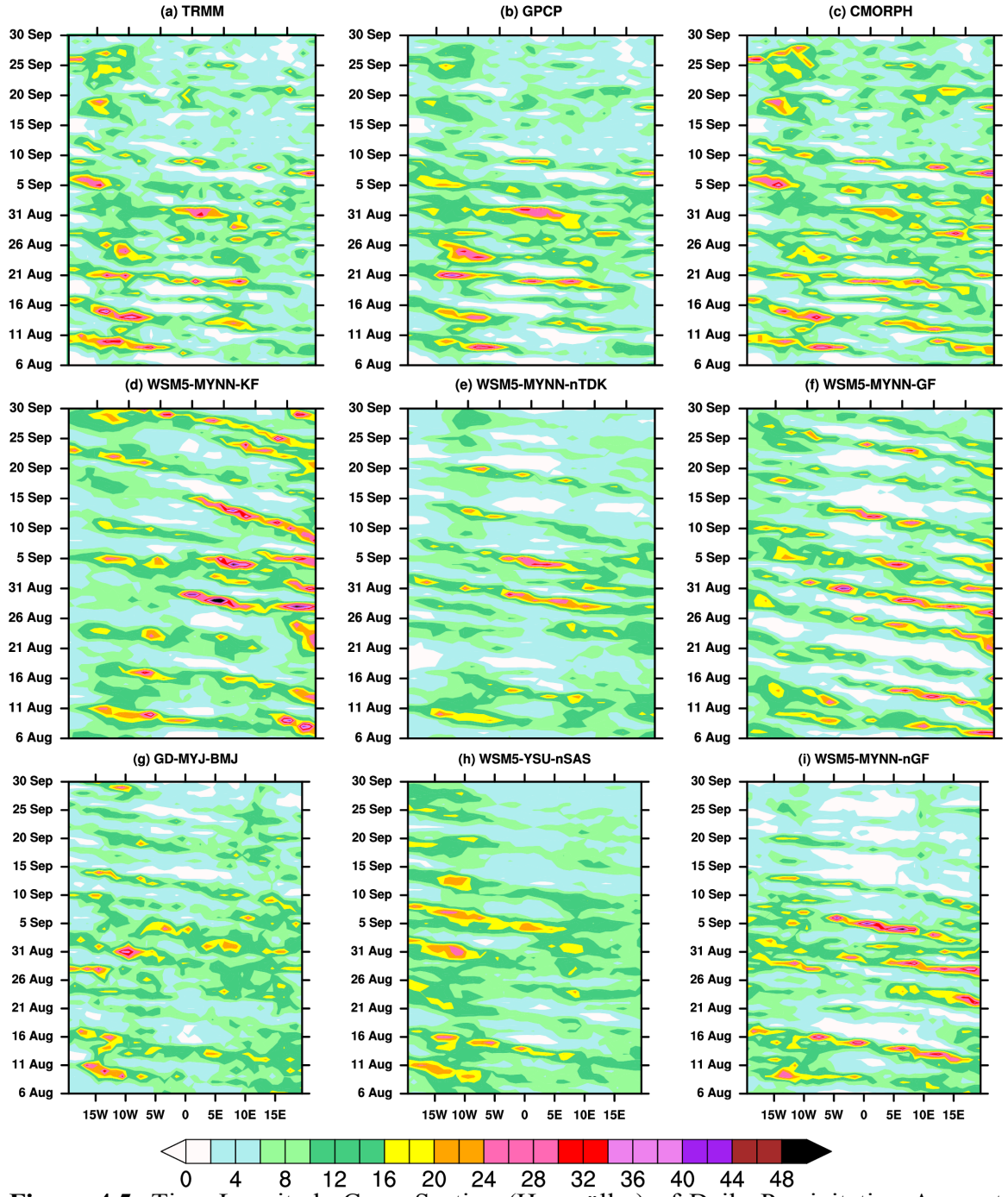

Figure 4.5: Time-Longitude Cross-Section (Hovmöller) of Daily Precipitation Amount (mm day^{-1}) Averaged over 5-15^{o}N

4.1.2 Statistical Analysis of Precipitation

There are different evaluation statistics that can be employed to assess model performance. However, there is no single statistic that addresses all aspects of interest. It is therefore important to consider different performance statistics and to understand the type of information they might provide. As emphasized earlier in Section 3.3.3, the information of interest in this sensitivity study is the correlation, systematic error, and accuracy of the model outputs relative to reference observations.

Figure 4.6 presents the scatter plots of precipitation for both time and space averaged statistics. TRMM was used as the reference observed data to evaluate other SRPs and model precipitation. GPCP and CMORPH agree with TRMM in terms of lesser MAE and stronger correlation both at spatial and temporal scales. Combinations such as nTDK, BMJ and nSAS show high skill with correlations between 0.4 – 0.65 and MAE of < 3 mm day^{-1} in space and time. Most simulations with KF or old GF performed poorly. However, the old GF combined with WSM5-MYNN performed fairly in WRFV3.8.1 while the modified nGF in WRFV3.9 produces a much better simulation when combined with the same MP and PBL schemes, that is, WSM5-MYNN. The improved performance of the nGF underlines the positive effects of its modification.

Comparative Model Skill Score (MSS) for precipitation is computed for all model physics combinations using the sum of the normalized statistics (Table 4.1) of measures in Figure 4.6. Furthermore, Table 4.2 shows the ranking of the different combinations based on the MSS. Each model simulations were ranked from the highest to the lowest. It can be seen from the table that simulations with BMJ, nTDK and nSAS had high MSS compared with those of KF, GF and nGF with low MSS. However, the nGF improved

much with WSM5-MYNN highlighting its advantage over the old GF CU. It is also possible to group the simulations sharing a particular parameterization. For instance, the average group score with GD MP has better skill than that with WSM5 while MYNN PBL group score is found to be higher than other PBLs (not shown). Also, the average group score of nSAS CU runs produces the highest MSS among the selected CU schemes.

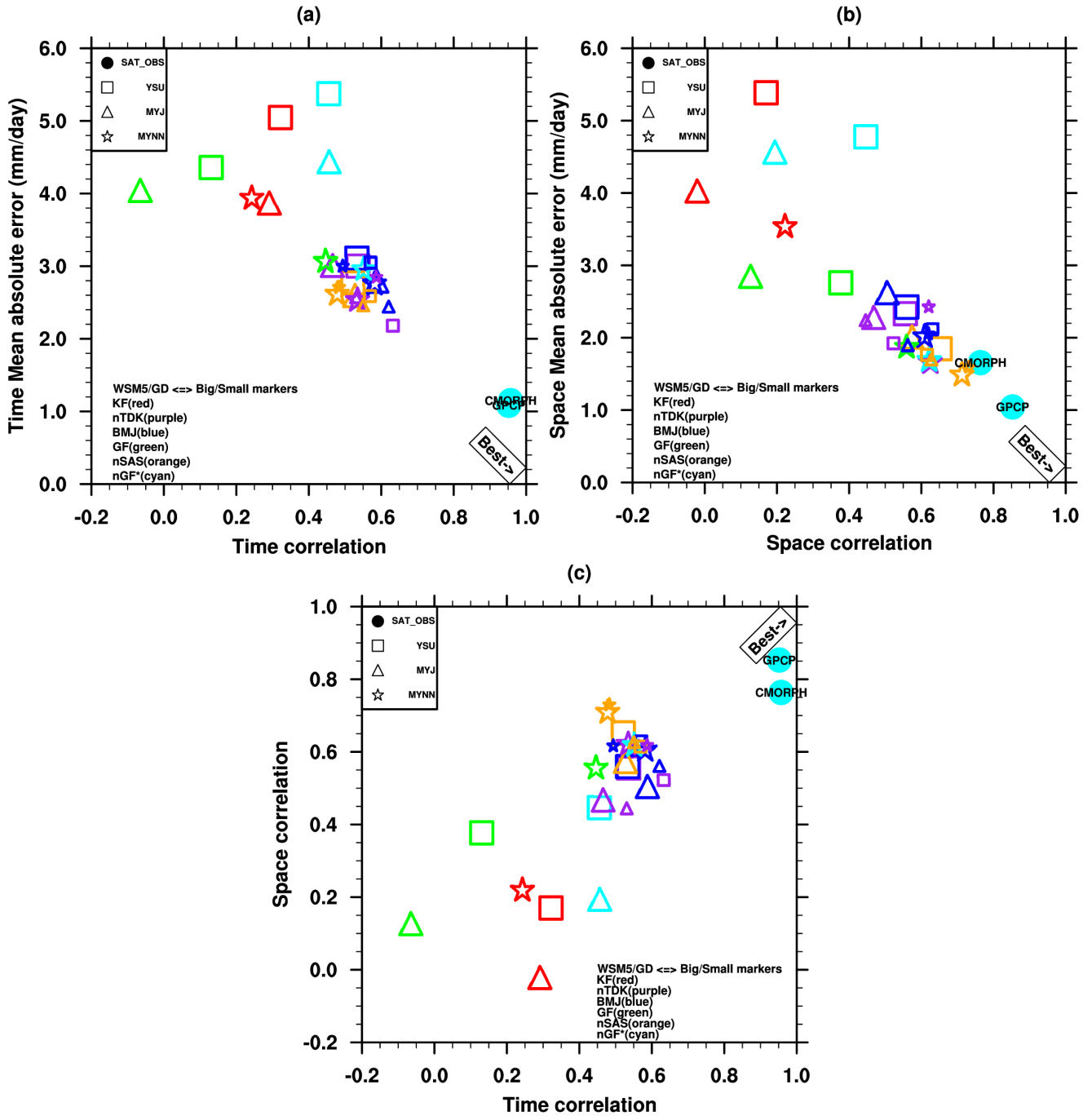

Figure 4.6: Scatter Plots of Precipitation Statistics for (a) Time MAE against Time Correlation, (b) Space MAE against Space Correlation, and (c) Space against Time Correlation.

NOTE: the best bar indicates the direction of the best model and observation. The shapes represent PBL schemes, size of the shapes represents the microphysics, and the colors are the CUs

Table 4.1: Raw and Normalized Statistics of Precipitation Averaged over 5-15^{o}N and 10^{o}W-10^{o}E

MODEL	Raw Statistics					Normalized statistics					MSS
	tr	tMAE	Sr	SMAE	B	tr_{norm}	1-$tMAE_{norm}$	Sr_{norm}	1-$S\|B\|_{norm}$	1-$SMAE_{norm}$	
WSM5-YSU-KF	0.31	5.04	0.14	5.61	55.86	0.55	0.09	0.26	0.07	0.00	0.97
WSM5-YSU-nTDK	0.54	2.95	0.49	2.54	20.36	0.88	0.75	0.83	0.67	0.81	3.95
WSM5-YSU-BMJ	0.56	2.93	0.51	2.56	22.62	0.91	0.76	0.87	0.63	0.80	3.98
WSM5-YSU-GF	0.12	4.36	0.32	2.98	18.41	0.28	0.31	0.56	0.70	0.69	2.54
WSM5-YSU-nSAS	0.51	2.77	0.54	2.26	15.40	0.84	0.81	0.92	0.75	0.88	4.20
WSM5-YSU-nGF	0.43	5.33	0.38	4.93	60.09	0.73	0.00	0.65	0.00	0.18	1.55
WSM5-MYJ-KF	0.29	3.82	-0.02	4.27	25.07	0.53	0.48	0.00	0.59	0.35	1.95
WSM5-MYJ-nTDK	0.45	3.04	0.38	2.53	10.13	0.75	0.72	0.65	0.84	0.81	3.78
WSM5-MYJ-BMJ	0.57	2.86	0.47	2.80	18.76	0.93	0.78	0.80	0.70	0.74	3.94
WSM5-MYJ-GF	-0.07	4.08	0.10	3.10	-6.12	0.00	0.39	0.19	0.91	0.66	2.16
WSM5-MYJ-nSAS	0.50	2.62	0.47	2.36	7.94	0.82	0.86	0.81	0.88	0.86	4.22
WSM5-MYJ-nGF	0.42	4.64	0.19	4.87	48.23	0.72	0.22	0.34	0.20	0.20	1.66
WSM5-MYNN-KF	0.25	3.95	0.16	3.95	23.50	0.47	0.43	0.30	0.62	0.44	2.25
WSM5-MYNN-nTDK	0.52	2.56	0.52	1.99	-1.22	0.86	0.87	0.89	0.99	0.95	4.57
WSM5-MYNN-BMJ	0.59	2.78	0.57	2.25	-2.01	0.95	0.81	0.96	0.98	0.89	4.59
WSM5-MYNN-GF	0.44	3.03	0.48	2.24	-0.89	0.75	0.73	0.81	1.00	0.89	4.17
WSM5-MYNN-nSAS	0.48	2.60	0.59	1.82	-7.46	0.80	0.86	1.00	0.89	1.00	4.55
WSM5-MYNN-nGF	0.53	2.97	0.51	2.10	-7.42	0.87	0.74	0.86	0.89	0.93	4.29
GD-YSU-nTDK	0.62	2.16	0.41	2.24	-8.66	1.00	1.00	0.70	0.87	0.89	4.45
GD-YSU-BMJ	0.57	3.06	0.54	2.40	15.46	0.93	0.72	0.91	0.75	0.85	4.17
GD-YSU-nSAS	0.55	2.61	0.50	2.11	9.10	0.90	0.86	0.85	0.86	0.92	4.40
GD-MYJ-nTDK	0.51	2.62	0.39	2.38	-21.23	0.84	0.86	0.67	0.66	0.85	3.87
GD-MYJ-BMJ	0.61	2.42	0.50	2.21	5.12	0.98	0.92	0.85	0.93	0.90	4.57
GD-MYJ-nSAS	0.54	2.46	0.51	2.09	2.59	0.88	0.91	0.87	0.97	0.93	4.55
GD-MYNN-nTDK	0.58	2.85	0.53	2.58	-31.21	0.95	0.78	0.89	0.49	0.80	3.91
GD-MYNN-BMJ	0.49	2.96	0.57	2.24	-9.46	0.82	0.75	0.97	0.86	0.89	4.28
GD-MYNN-nSAS	0.47	2.66	0.60	1.87	-14.18	0.79	0.84	1.02	0.78	0.99	4.41

Table 4.2: Model Skill Score (MSS) for Precipitation Averaged over 5-15^{o}N and 10^{o}W-10^{o}E

Precipitation Score		
Ranking	**Model**	**MSS(5)**
1	WSM5-MYNN-BMJ	4.59
2	GD-MYJ-BMJ	4.57
3	WSM5-MYNN-nTDK	4.57
4	GD-MYJ-nSAS	4.55
5	WSM5-MYNN-nSAS	4.55
6	GD-YSU-nTDK	4.45
7	GD-MYNN-nSAS	4.41
8	GD-YSU-nSAS	4.40
9	WSM5-MYNN-nGF	4.29
10	GD-MYNN-BMJ	4.28
11	WSM5-MYJ-nSAS	4.22
12	WSM5-YSU-nSAS	4.20
13	WSM5-MYNN-GF	4.17
14	GD-YSU-BMJ	4.17
15	WSM5-YSU-BMJ	3.98
16	WSM5-YSU-nTDK	3.95
17	WSM5-MYJ-BMJ	3.94
18	GD-MYNN-nTDK	3.91
19	GD-MYJ-nTDK	3.87
20	WSM5-MYJ-nTDK	3.78
21	WSM5-YSU-GF	2.54
22	WSM5-MYNN-KF	2.25
23	WSM5-MYJ-GF	2.16
24	WSM5-MYJ-KF	1.95
25	WSM5-MYJ-nGF	1.66
26	WSM5-YSU-nGF	1.55
27	WSM5-YSU-KF	0.97

4.1.3 Surface Temperature Analysis

Similar to the precipitation, the diurnal cycle of surface temperature at 2 meters (T2m) are computed for each of the 27 members runs in Table 3.2. These are compared with ERAI (taken as reference), MERRA, NCEP, and GSAT. Figure 4.7a shows the plot of the modeled and reanalyzed diurnal cycle of T2m compared with ERAI. The biases of the 27 members relative to ERAI are shown in Figure 4.7b. In Figure 4.7a the surface temperature for both model and reanalysis reach their minimum and maximum peak at 06 hour and 15 hour, respectively. However, with the observed minimum and maximum reproduced in all simulations, there exist systematic error between reanalysis and model in Figure 4.7a, therefore, the need for the bias plot in Figure 4.7b.

It is evident in Figure 4.7b that the magnitude of peak in MERRA is earlier at 12 hour compared with other reanalyses. Combinations with YSU produce the highest difference ranging between 0.4 to 0.8^{o}C during early daytime and nighttime. The simulations of MYNN MP are closer to ERAI in the early hours of the day than MYJ, however, both show cold bias during evening and nighttime. Also, T2m responds differently to the combination of CU schemes with MP and PBL. For example, nSAS mostly simulates a warm bias in all combinations while GF reproduces cooling. The cooling in nTDK is obviously stronger with GD than with WSM5, and this cumulus scheme seems to vary more with the selected microphysics than other cumulus options. At night the nGF is warmer than GF but cooler during the daytime.

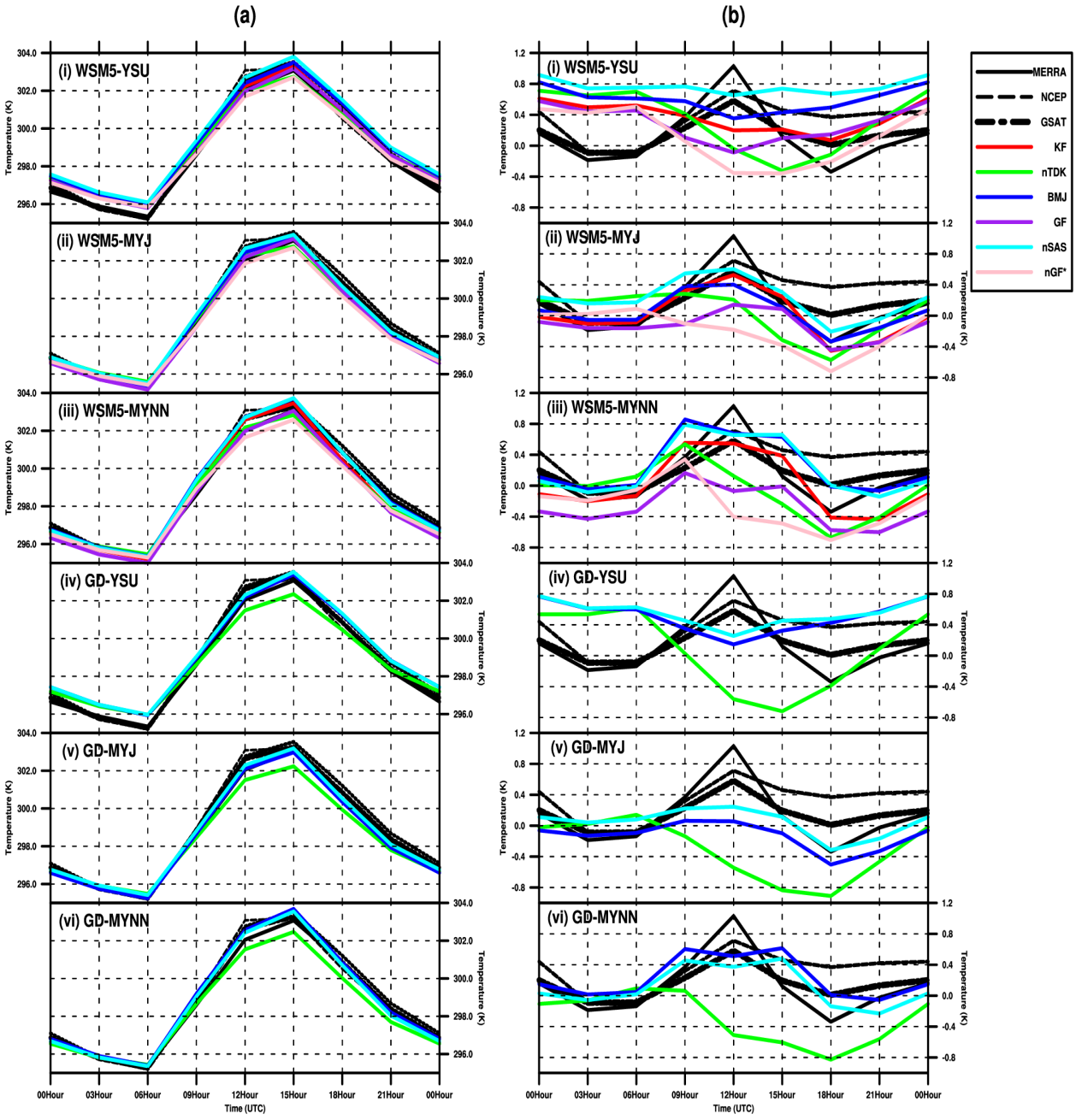

Figure 4.7: Stack Plot of (a) Diurnal Circle of Surface Temperature and (b) Difference with Respect to ERA Reanalysis for Aug-Sep 2007.

NOTE: The stack plot is the same as described in Figure 4.1 and the bias plot was made to clearly see the difference between the model and reference datasets

Figure 4.8, displays the daily-averaged 2 m temperature in the region over the two-month period. The figure shows bias between ERAI and NCEP, MERRA and GSAT, that is, ERAI is mostly cooler than the other reanalysis products. However, the models and reanalysis products have the same pattern of daily T2m. On average, all series tend to fluctuate between ~25 - 26^{o}C in August and thereafter become warmer by 1-2^{o}C in September. The warming marks the end of the monsoon season when the rainband, which tightly coupled with the movement of the Inter-Tropical Discontinuity (ITD), retreats southwards such that cloud cover and precipitation decrease and insolation increases. The magnitude of the daily surface temperature series is higher in YSU PBL simulations but consistently more realistic in MYJ and MYNN. One distinguishing difference between GF and nGF is that GF is out of phase compared with ERAI. This behavior is more pronounced in the month of September where the T2m by GF is found to have cold bias relative to ERAI.

Unlike the highly variable precipitation, the model simulates a more realistic spatial distribution of surface temperature. The strong temperature gradient in the Sahel (above 10^{o}N) was well captured in the model. The cooling over higher grounds such as that of the Cameroun Mountain, Jos plateau and Guinea highland is also clearly reproduced. The temperature over the ocean is better simulated in runs shown here with BMJ and nSAS when compared with ERAI.

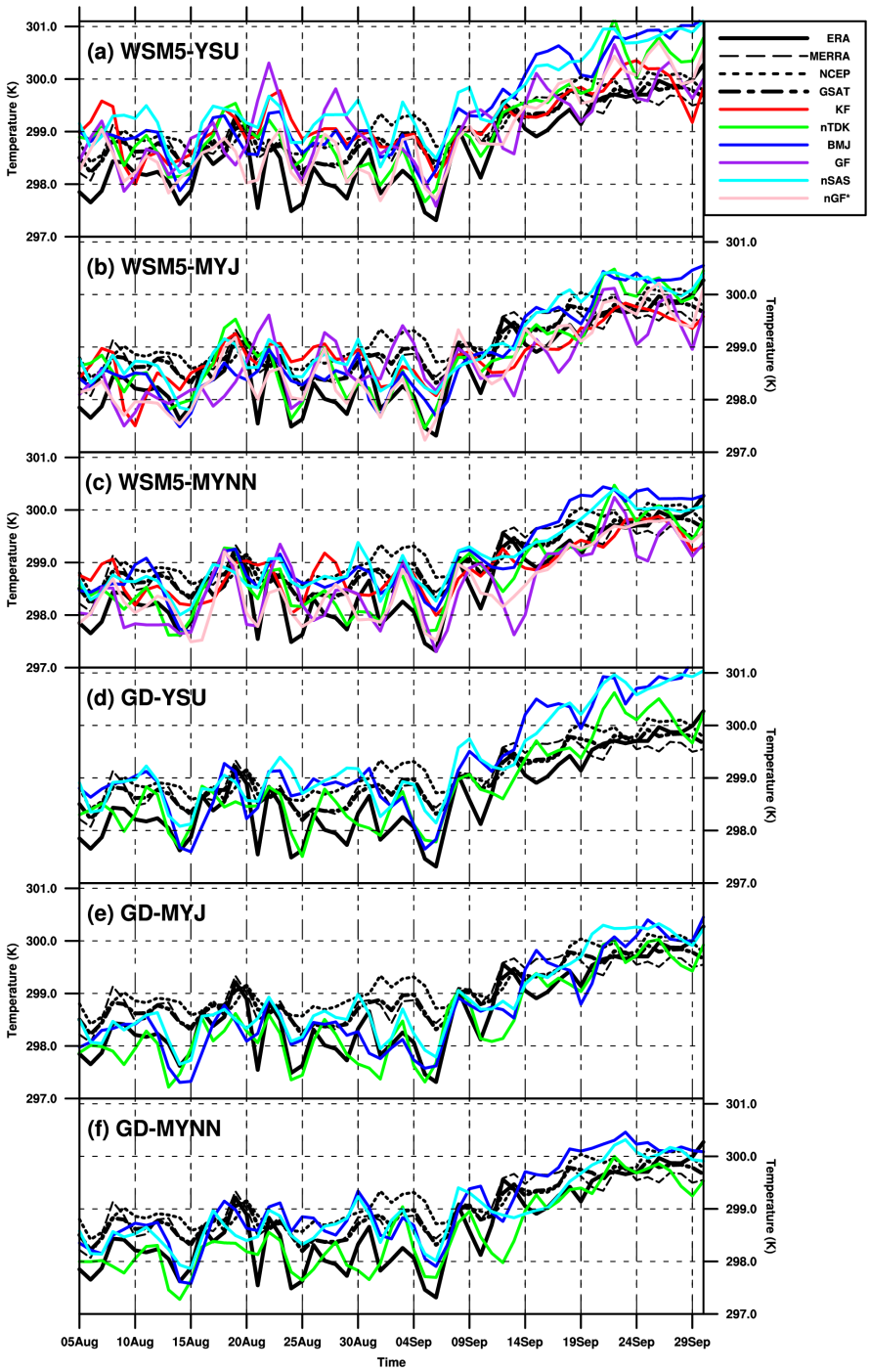

Figure 4.8: Time Series of Daily-Averaged 2 Meters Surface Temperature Averaged over 5-15^{o}N and 10^{o}W-10^{o}E. The Stack Plot is the same as Described in Figure 4.1.

The spatial biases in Figure 4.10 shows that T2m in the model and reanalysis differ from ERAI within the range -3 and 3^{o}C. All reanalyses show a cool bias over the Sahel and warming around the Guinea coast relative to ERAI. Similarly, the models simulate relative coolness in some parts of the Sahel and warm bias near the Guinea coast where, as seen in Figure 4.9, the hot area extends further south than in ERAI. nSAS with WSM5-YSU simulates general warming over a large land area and some parts of the ocean near the equator. nTDK and GF combined with WSM5-MYNN simulate about 1^{o}C cooling over the ocean while KF, BMJ, and nGF reproduce warming of the same magnitude around the equatorial region of the Atlantic Ocean.

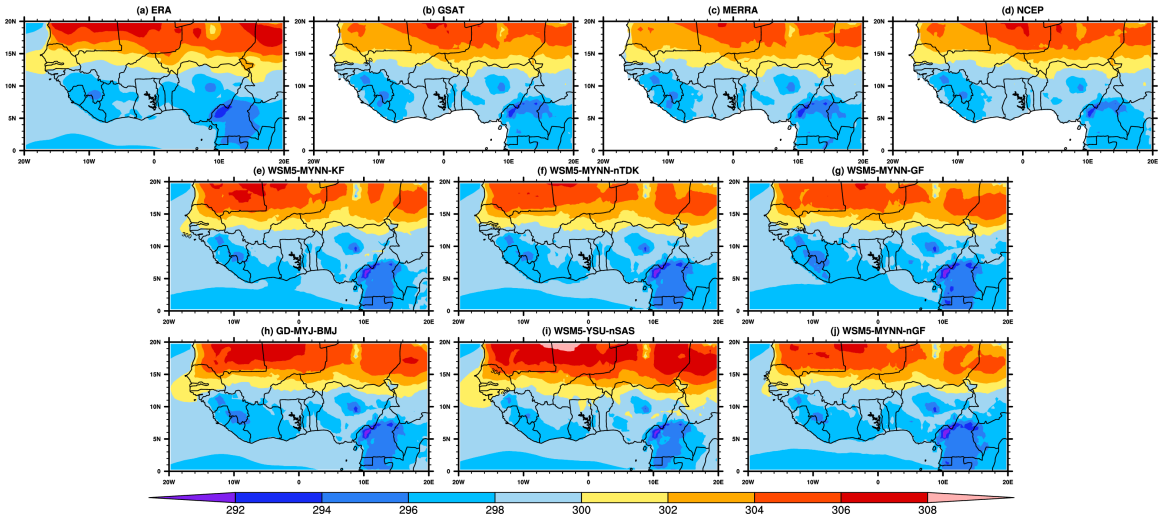

Figure 4.9: Spatial Distribution of 2 Meters Surface Temperature (K) Averaged for the Period of August-September 2007

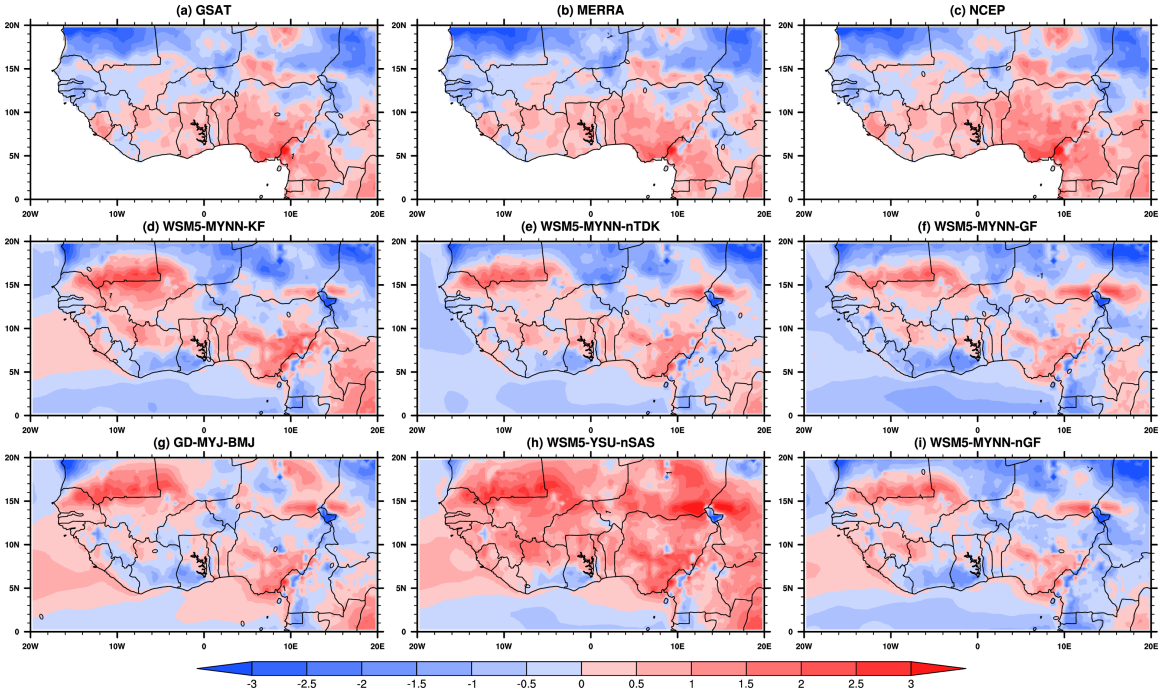

Figure 4.10: Spatial Bias of 2 Meters Surface Temperature (K) Averaged for the Period of August-September 2007

4.1.4 Statistical Analysis of T2m

A similar approach as for precipitation is used to evaluate the surface temperature. Figure 4.11 show that both reanalysis and model simulations compare well with ERAI (reference data). The models perform better in time MAE than in space MAE but better in space correlation than time correlation. The role of the MP scheme is not clearly seen with T2m as both WSM5 (big shapes) and GD (small shapes) MP cluster together in the plot. However, some combinations with YSU (squares) perform poorly both in space and time statistics. For example, in Figure 4.11b, two of nSAS and BMJ simulations combined with YSU produced the highest MAE (>0.7^{o}C). Some MYJ and MYNN have the lowest MAE and higher r in space and time average, respectively. Furthermore, KF or GF CUs perform poorly in the overall simulation (as was seen in precipitation). The nGF and nTDK compete favorably with each other and simulate T2m better. This again underscores the significant improvement in the modified nGF CU, most especially when combined with MYNN PBL.

The MSS, computed from the normalized model statistics in Table 4.3, is used to rank the model's performance based on how well each simulation reproduced T2m. The relative average group score of GD, MYNN and nTDK show higher skill. But, the combinations with WSM5-MYNN-nTDK and GD-MYJ-BMJ are found to rank within the top 3 (Table 4.4) combinations as was seen in the precipitation ranking.

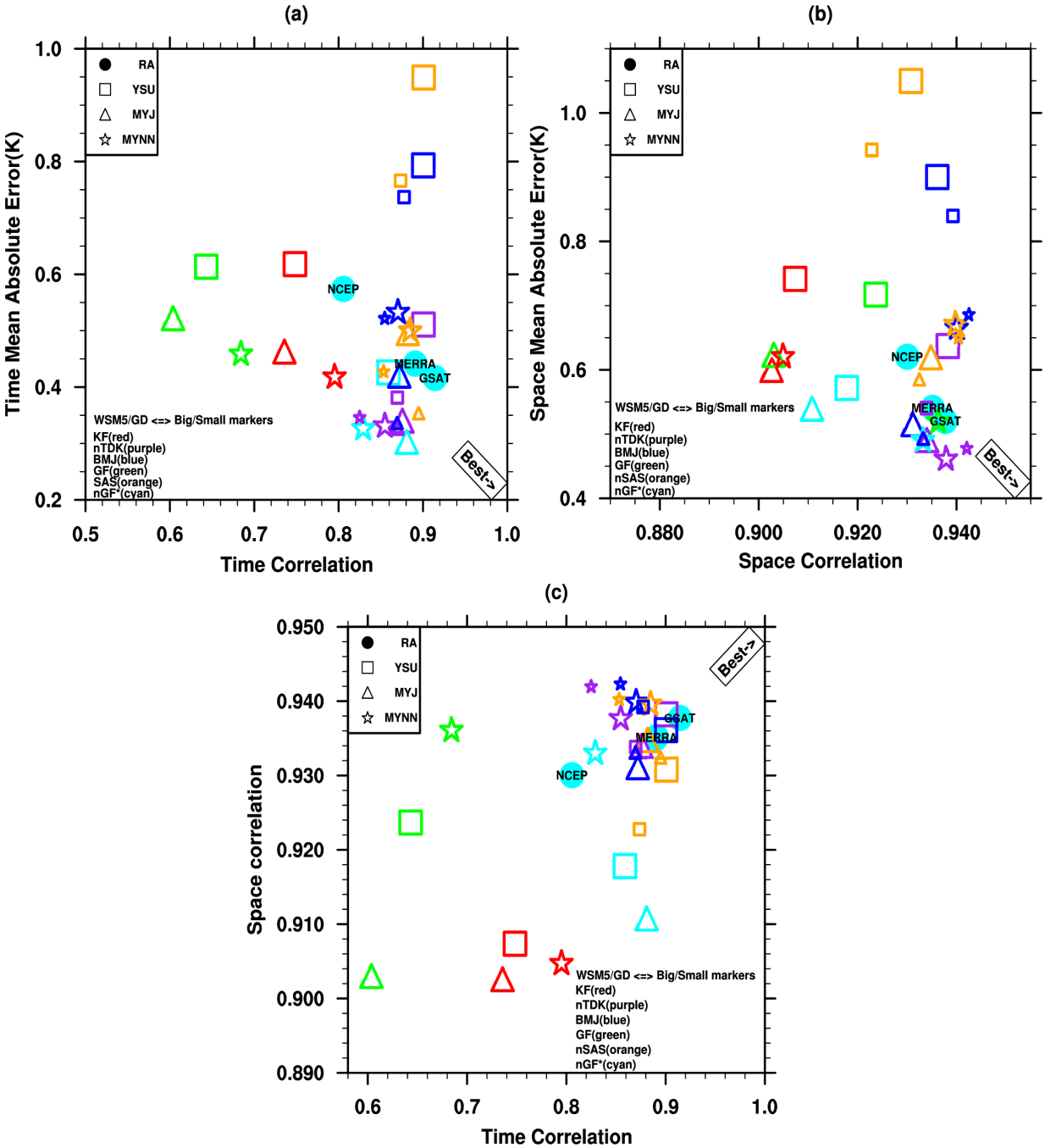

Figure 4.11: Scatter Plots of Surface Temperature at 2 Meters for (a) Time MAE against Time Correlation, (b) Space MAE against Space Correlation, and (c) Space against Time Correlation.

NOTE: Same as precipitation scatter plots the best bar indicates the direction of the best model and observation. The shapes represent PBL schemes, size of the shapes represents the microphysics, and the colors are the CUs

Table 4.3: Raw and Normalized Statistics of Surface Temperature Averaged over 5-15°N and 10°W-10°E

MODEL	Raw Statistics					Normalized statistics					MSS
	tr	tMAE	Sr	SMAE	B	tr_{norm}	1-$tMAE_{norm}$	Sr_{norm}	1-$|B|_{norm}$	1-$SMAE_{norm}$	
WSM5-YSU-KF	0.75	0.62	0.91	0.74	54.81	0.49	0.51	0.13	0.42	0.53	2.08
WSM5-YSU-nTDK	0.90	0.51	0.94	0.64	49.16	1.00	0.68	0.95	0.48	0.70	3.82
WSM5-YSU-BMJ	0.90	0.79	0.94	0.90	77.20	1.00	0.24	0.90	0.19	0.25	2.58
WSM5-YSU-GF	0.64	0.61	0.92	0.72	45.86	0.13	0.52	0.56	0.52	0.57	2.30
WSM5-YSU-nSAS	0.90	0.95	0.93	1.05	94.74	1.00	0.00	0.75	0.00	0.00	1.75
WSM5-YSU-nGF	0.86	0.43	0.92	0.57	28.53	0.86	0.81	0.41	0.70	0.81	3.59
WSM5-MYJ-KF	0.74	0.46	0.90	0.60	21.17	0.44	0.75	0.00	0.78	0.77	2.74
WSM5-MYJ-nTDK	0.88	0.34	0.93	0.49	21.02	0.92	0.94	0.84	0.78	0.95	4.43
WSM5-MYJ-BMJ	0.87	0.42	0.93	0.52	24.70	0.90	0.82	0.76	0.74	0.91	4.14
WSM5-MYJ-GF	0.60	0.52	0.90	0.62	6.75	0.00	0.66	0.01	0.93	0.73	2.33
WSM5-MYJ-nSAS	0.88	0.50	0.93	0.62	42.27	0.94	0.70	0.86	0.56	0.73	3.79
WSM5-MYJ-nGF	0.88	0.30	0.91	0.54	-0.46	0.93	1.00	0.22	1.00	0.87	4.02
WSM5-MYNN-KF	0.80	0.42	0.90	0.62	22.42	0.64	0.82	0.06	0.77	0.73	3.02
WSM5-MYNN-nTDK	0.85	0.33	0.94	0.46	13.27	0.85	0.95	0.94	0.86	1.00	4.60
WSM5-MYNN-BMJ	0.87	0.53	0.94	0.67	46.90	0.90	0.64	1.00	0.51	0.65	3.70
WSM5-MYNN-GF	0.68	0.46	0.94	0.52	-7.48	0.27	0.76	0.90	0.93	0.90	3.75
WSM5-MYNN-nSAS	0.88	0.50	0.94	0.67	44.07	0.95	0.69	0.99	0.54	0.64	3.81
WSM5-MYNN-nGF	0.83	0.33	0.93	0.49	-6.63	0.76	0.96	0.82	0.93	0.95	4.42
GD-YSU-nTDK	0.87	0.38	0.93	0.54	21.83	0.89	0.88	0.84	0.77	0.87	4.25
GD-YSU-BMJ	0.88	0.74	0.94	0.84	67.46	0.92	0.33	0.98	0.29	0.36	2.88
GD-YSU-nSAS	0.87	0.77	0.92	0.94	72.63	0.91	0.28	0.54	0.23	0.18	2.15
GD-MYJ-nTDK	0.87	0.33	0.93	0.49	-14.27	0.90	0.96	0.82	0.85	0.95	4.48
GD-MYJ-BMJ	0.87	0.34	0.93	0.49	6.49	0.89	0.95	0.82	0.94	0.95	4.54
GD-MYJ-nSAS	0.89	0.35	0.93	0.59	24.23	0.98	0.92	0.80	0.75	0.79	4.24
GD-MYNN-nTDK	0.82	0.35	0.94	0.48	-11.49	0.74	0.93	1.05	0.88	0.97	4.58
GD-MYNN-BMJ	0.85	0.52	0.94	0.69	43.52	0.84	0.66	1.06	0.54	0.62	3.73
GD-MYNN-nSAS	0.85	0.43	0.94	0.65	31.51	0.84	0.81	1.01	0.67	0.68	4.00

Table 4.4: Model Skill Score for 2 Meters Surface Temperature Averaged over 5-15^{o}N and 10^{o}W-10^{o}E

2m Temperature Score		
Ranking	**Model**	**MSS(5)**
1	WSM5-MYNN-nTDK	4.60
2	GD-MYNN-nTDK	4.58
3	GD-MYJ-BMJ	4.54
4	GD-MYJ-nTDK	4.48
5	WSM5-MYJ-nTDK	4.43
6	WSM5-MYNN-nGF	4.42
7	GD-YSU-nTDK	4.25
8	GD-MYJ-nSAS	4.24
9	WSM5-MYJ-BMJ	4.14
10	WSM5-MYJ-nGF	4.02
11	GD-MYNN-nSAS	4.00
12	WSM5-YSU-nTDK	3.82
13	WSM5-MYNN-nSAS	3.81
14	WSM5-MYJ-nSAS	3.79
15	WSM5-MYNN-GF	3.75
16	GD-MYNN-BMJ	3.73
17	WSM5-MYNN-BMJ	3.70
18	WSM5-YSU-nGF	3.59
19	WSM5-MYNN-KF	3.02
20	GD-YSU-BMJ	2.88
21	WSM5-MYJ-KF	2.74
22	WSM5-YSU-BMJ	2.58
23	WSM5-MYJ-GF	2.33
24	WSM5-YSU-GF	2.30
25	GD-YSU-nSAS	2.15
26	WSM5-YSU-KF	2.08
27	WSM5-YSU-nSAS	1.75

The physics combinations of WSM5-MYNN-nTDK and GD-MYJ-BMJ are ranked highest (Table 4.5) with the combined statistics of precipitation and surface temperature equally weighted to give a score out of 10. Based on the model rankings some combinations are however found to have good performance (subjectively defined as MSS > 7.5), others moderate and some performed poorly (MSS < 5) with precipitation and surface temperature. This corroborates the conclusion of Flaounas et al. (2011) and Noble et al. (2014) that any evaluation adopted is subjective and could depend on the variable of interest. However, it is notable that the good scheme combinations are probably not separated in a statistically significant way. A comprehensive summary of results in Table 4.5 is further presented in Figure 4.12. This figure shows no significant difference between the MP used as their combinations with the same CU and PBL schemes fall within the same performance category based on the overall MSS. For the CU schemes, all nTDK combination produce good simulations while KF, on the contrary, performs moderately with MYNN and poorly with YSU and MYJ combinations. BMJ and nSAS combinations are both good with MYJ and MYNN and moderate with YSU. Both GF and nGF as stated earlier produce a better simulation only when combined with MYNN. Furthermore, the simulations with MYNN PBL, when combined with CU and MP schemes, have a general advantage over the other two PBL schemes, however, its skill is also reduced when used with the KF CU scheme. On the other hand, MYJ only performs well with BMJ, nSAS and nTDK CU. And the YSU PBL performance is good only when combined with nTDK.

Table 4.5: Overall MSS Ranking for the Combination of 2 Meters Surface Temperature and Precipitation

Precipitation and Temperature Score			
Ranking	**Model**	**MSS(10)**	**REMARK**
1	WSM5-MYNN-nTDK	9.17	
2	GD-MYJ-BMJ	9.11	
3	GD-MYJ-nSAS	8.79	
4	WSM5-MYNN-nGF	8.71	
5	GD-YSU-nTDK	8.70	
6	GD-MYNN-nTDK	8.50	
7	GD-MYNN-nSAS	8.41	
8	WSM5-MYNN-nSAS	8.36	**GOOD**
9	GD-MYJ-nTDK	8.36	
10	WSM5-MYNN-BMJ	8.29	
11	WSM5-MYJ-nTDK	8.21	
12	WSM5-MYJ-BMJ	8.08	
13	WSM5-MYJ-nSAS	8.01	
14	GD-MYNN-BMJ	8.01	
15	WSM5-MYNN-GF	7.93	
16	WSM5-YSU-nTDK	7.76	
17	GD-YSU-BMJ	7.04	
18	WSM5-YSU-BMJ	6.55	
19	GD-YSU-nSAS	6.55	**MODERATE**
20	WSM5-YSU-nSAS	5.95	
21	WSM5-MYJ-nGF	5.68	
22	WSM5-MYNN-KF	5.27	
23	WSM5-YSU-nGF	5.15	
24	WSM5-YSU-GF	4.84	
25	WSM5-MYJ-KF	4.69	**POOR**
26	WSM5-MYJ-GF	4.49	
27	WSM5-YSU-KF	3.04	

CU / **PBL**	KF	BMJ	GF	nTDK	nSAS	nGF*	
YSU	WSM5	WSM5/GD	WSM5	WSM5/GD	WSM5/GD	WSM5	
MYJ	WSM5	WSM5/GD	WSM5	WSM5/GD	WSM5/GD	WSM5	**MP**
MYNN	WSM5	WSM5/GD	WSM5	WSM5/GD	WSM5/GD	WSM5	

Figure 4.12: The 27 Different WRF Model Physics Combinations Included in the Sensitivity Analysis.

NOTE: The combinations containing the asterisked CU scheme are runs from the newly modified Grell-Freitas in WRFV3.9. The figure shows a summary of results in Table 4.5. Green highlights are good combinations while yellow and red are moderate and poor combinations, respectively

However, it is quite important to note that factors such as the initial and lateral boundary conditions may influence the performance of the identified good physics combinations for longer simulations of the WAM regime. This may affect the skill scores of the identified best performing regional physics combination. The effect appears however to be less than one standard deviation from the two-month test when compared with the mean of some eight-month (March-October 2007) tests (not shown). This implies that the model skill score (MSS) of the long-term runs lies within the variability of that found using the same two-month regime from the 8-month runs. Furthermore, the results of this study also point out the schemes that are developed together tend to perform better (e.g. MYJ-BMJ; MYNN-nGF; but less so YSU-nSAS) even though their primary tuning has not been for West Africa.

4.2 RESULTS FROM NORMAL MONSOON YEAR

This section intends to use the identified better performing WRF model physics combination to simulate a long-term West African monsoon period, that is, March to October. Here the analysis will focus on the ability of the identified physics combination to simulate the monsoon rainfall, temperature and wind fields.

4.2.1 Intraseasonal and Interannual Variability

Rainfall is one of the important atmospheric field variables used to explain the intraseasonal and interannual variability of climate over West Africa (e.g. Hulme, 1992; Nicholson, 1989). For instance, the latitudinal evolution of the rainband is well correlated with the displacement of the ITCZ. To place the year 2007 in an interannual context, the

GPCP and model output of the three combinations are used. Time-latitude cross-section that depicts the evolution of monthly rainfall over West Africa (averaged over 10°W-10°E) is plotted for the year 2007 in Figure 4.13. The pattern describes two phases of the rainfall season over the area. The first one corresponds to the beginning of the main rainfall season from April to the end of June over West Africa. This period marks the pre-onset during which only regions in the Guinea coast (i.e. south of 8°N) experience rainfall. Also, the core of rainfall maximum is located at about 5°N latitude in this phase. The second phase is associated with the middle and the end of the main rainfall season when the monsoon is fully developed. The regions concerned are located between 8-18°N. The rainfall maxima shift from 5°N in the first phase to about 10°N in this regime. The nonlinear transition of rainfall from the first to the second regime is described as the "monsoon jump", which is the observed abrupt latitudinal shift of rainfall maximum from the Guinea coast into the Sahel region in June (Hagos & Cook, 2007b; Le Barbé et al., 2002; Lebel et al., 2003; Sultan & Janicot, 2003). The monsoon jump enhances the appearance of the "little dry season" sometimes within July and August in the Guinea coast. During the little dry season, there is a significant reduction of rainfall frequency and amount as well as the encroachment of the tongue-like middle latitude high-pressure system. This period coincides with the northernmost position of the Inter-Tropical Discontinuity (ITD) at about 21-22°N latitudes (Nicholson, 2013; among others).

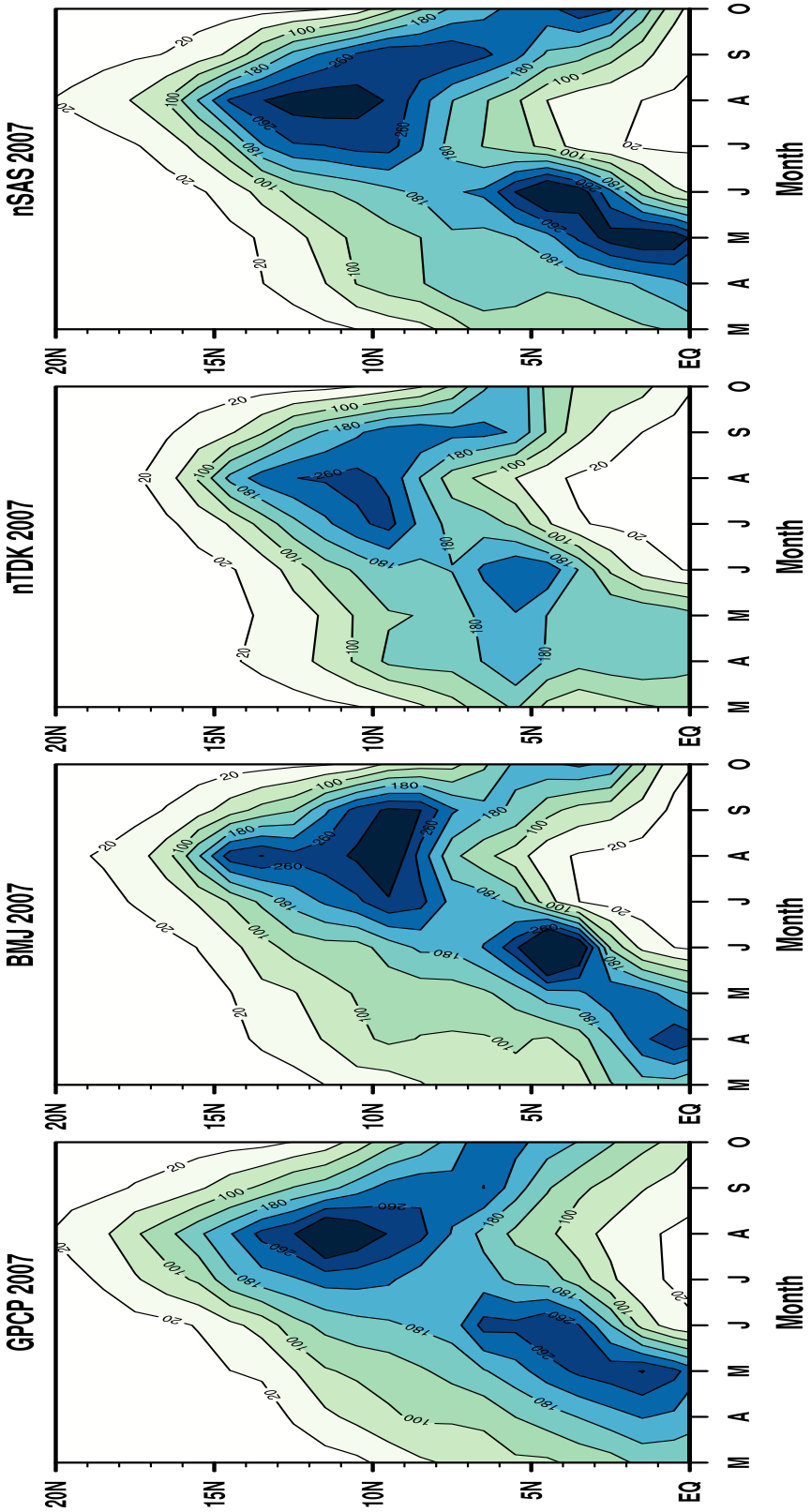

Figure 4.13: Time-Latitude Cross-Section of the Monthly Rainfall Averaged on 10◦W–10◦E in 2007.

The simulated monthly rainfall of 2007 WAM season show similar behavior in comparison with GPCP (Figure 4.13) though slight differences can be seen. The first rainfall season is well marked in the GD-MYJ-BMJ and WSM5-YSU-nSAS, particularly in the latter combinations. Even if, in common, the signal is stronger in the second season, the rainfall distribution pattern is well reproduced in all combinations. Likewise, the combinations can simulate the reduction in rainfall amount within the months of July-August, though, with further northward extent. All datasets clearly show the abrupt shift of maximum precipitation core from 5^{o}N to 10^{o}N latitude. Although, the observed double rainfall season in WSM5-MYNN-nTDK is not as strong, it was able to show the core and monsoon jump. WSM5-YSU-nSAS clearly simulates the 2007 normal monsoon year as observed in GPCP.

4.2.2 Monsoon Flow

Figure 4.14 presents the monthly averaged wind field at 925hPa from March to October for 2007. The black continuous line on Figure 4.14 represents the zero-isoline of the zonal component, which is the westerly component that defines the northernmost position of the monsoon winds. Overland, this isoline characterizes the location of the ITD that marks the meeting zone of the southwesterly moist monsoon winds and the northeasterly dry Harmattan winds. In March the ITD is found just south of 10^{o}N and corresponds to the beginning of the moisture build-up over the Guinea coast region. There is a smooth northward transition of the ITD from March to July during which it attains a maximum latitudinal position around 20^{o}N. The ITD thereafter retreats southwards in August and October, which corresponds to the ending of the monsoon season in the region. The longitudinal extension of the monsoon winds in June, that is, between 15^{o}W and 5^{o}E,

suffices to determine the rainfall onset in most parts of Guinea coast and Savannah climatic zones of the region. Over the Ocean, the Inter-Tropical Convergence Zone (ITCZ), similar to the ITD but different in terms of the airmass characteristics to the north and south of the confluence zone, extends well to the west south of 10^{o}N in June. In July, the ITCZ moves to a mean latitudinal position of 10^{o}N, a quasi-stable state described in Janicot et al. (2008). During this stage, the area of the westerly winds extends largely overland and the Atlantic Ocean between 5^{o}N and 18^{o}N and the ITD reached its northernmost latitude of 20^{o}N. Also, in July, the strength of the westerly winds intensifies over West Africa. The monsoon is fully developed in August and consistent with the high Atlantic Ocean and northernmost position of the Saharan heat low overland (see Figures 4.18; vertical cross-section of Temperature). The presence of the ITCZ around 10^{o}N in August is tightly coupled with the dominant area of vertical ascent and moisture convergence as well as the increased rainfall in the monsoon region (see Figures 4.19; vertical cross section of Omega and rainfall). In September, the area of the westerly winds reduced, and its magnitude decreased significantly. The influx of the moisture-laden westerly winds reduced significantly especially in the western part of the region in October.

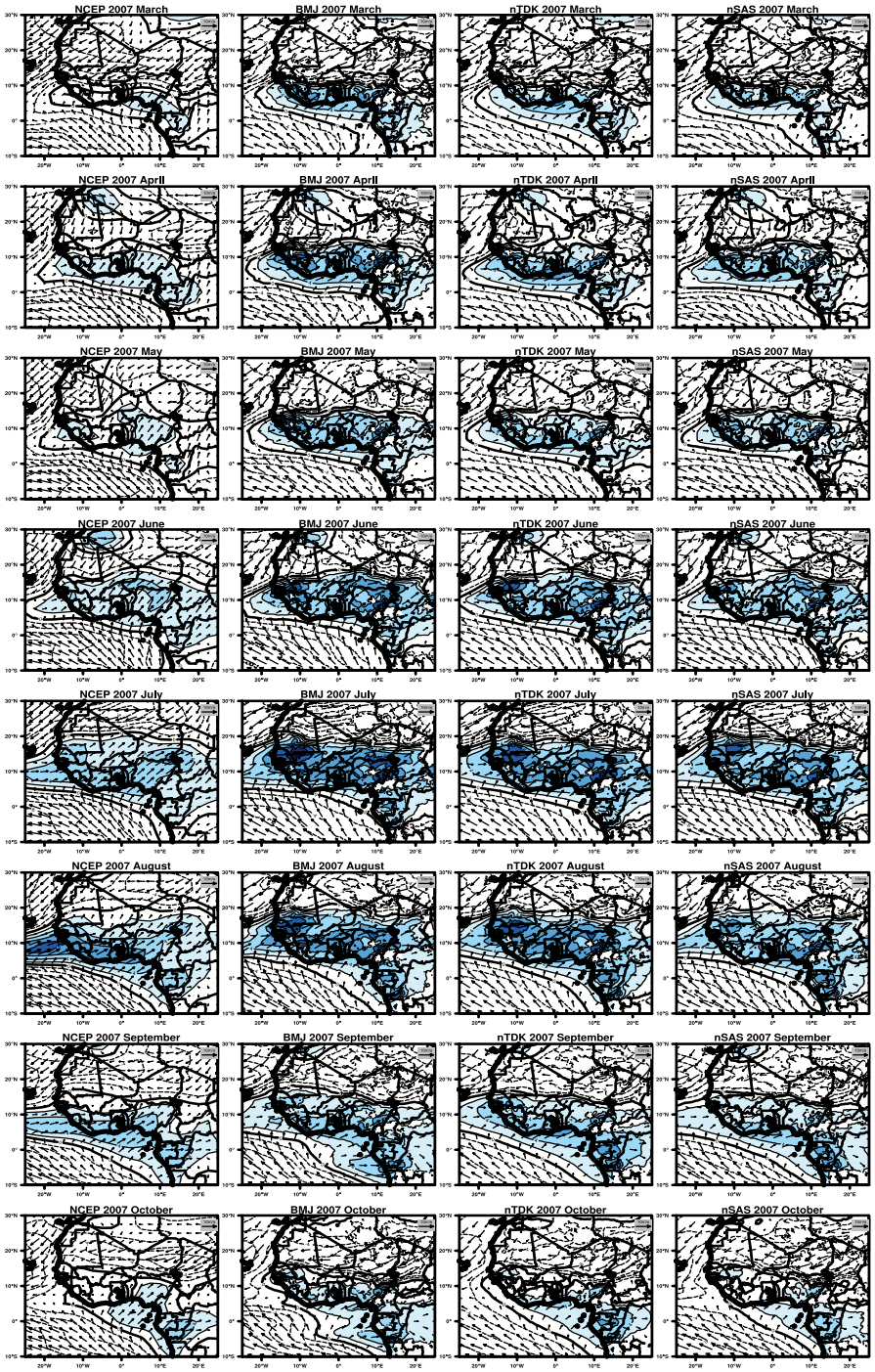

Figure 4.14: Averaged Wind Fields at 925 hPa for March-October Derived from NCEP and Models for 2007.

NOTE: Shaded areas for westerly wind component higher than $2ms^{-1}$. The reference wind vector is displaced as10 ms^{-1}. Each column of the panel plot represents (a) NCEP, (b) GD-MYJ-BMJ, (c) WSM5-MYNN-nTDK, and (d) WSM5-YSU-nSAS, respectively. The rows are plots of Mar-Oct.

The southwesterly winds and local moisture recycling are the two main sources of moisture supply during the WAM season (Eltahir & Gong, 1996; Levermann et al., 2009; Thorncroft et al., 2011). The westerly winds simulated by the models are stronger compared with observation and thus result in a stronger simulation of rainfall between June and August. This highlights the role of the winds as a dominant source of moisture to realize realistic monsoon dynamics when compared with observation. In March, the ITCZ is located around 5^{o}N in WSM5-YSU-nSAS and similar compared with the observed position. In GD-MYJ-BMJ and WSM5-MYNN-nTDK the ITCZ was simulated further north. The simulated ITD transitioned northward from March through July to reach its maximum northernmost latitudinal position of approximately 20^{o}N. In August, the mean position of the simulated ITCZ was also located around 10^{o}N. The area of the simulated westerly winds largely extended further north and intensified significantly. The area coverage of the westerlies is not significantly different in July and August but it weakened in the latter month. In September, all model configurations also reproduced both reduced area coverage and significantly weaker winds. This process continued in October as the ITD retreats further southwards corresponding to the ending of the monsoon season.

4.2.3 Mean Zonal Wind Field

The latitudinal transect of zonal winds averaged on longitudes 10^{o}W and 10^{o}E is shown in Figure 4.15. Apparent are two easterly jets, the mid-tropospheric jet near 650hPa and the upper-tropospheric jet around 150hPa. The mid-tropospheric jet is well known as the African Easterly Jet (AEJ). The AEJ was described as one of the two mid-tropospheric jets situated in the Northern Hemisphere of West Africa (Nicholson & Grist,

2003). This AEJ is induced by thermal contrast between the Atlantic Ocean and hot Sahara and maintained by both dry and moist convection to the north and south, respectively (Thorncroft & Blackburn, 1999; Zhang et al., 2008). The jet is also associated with zones of horizontal (mostly strong in August) and vertical (mostly strong in May to July) shear (Gu & Adler, 2004; Nicholson & Grist, 2003). There has been a focus on the AEJ because of its role in producing African Easterly Waves. The seasonal circle of the AEJ is summarized in Figure 4.15. Also evident in Figure 4.15 are the two upper-tropospheric mid-latitudes westerly jets and a low-level westerly wind maximum proximate to the equator.

In the Northern Hemisphere of West Africa, the AEJ is observed throughout the year (Nicholson & Grist, 2003). The AEJ is also shown to be present during the entire period (March-October) of this study, but in the month where the monsoon is fully established (i.e. in July), the strength reduced. Also, it shifts from around 5^{o}N in March to about 15^{o}N in August and thereafter began to retreat faster in September to about 5^{o}N again in October. The speed of the jet core is $11ms^{-1}$ in July and October and $15ms^{-1}$ in March and June. The height position of the core also changes throughout the months. The core is at 600hPa in March-August, when it is quite strong. It descends to around 700hPa in the month of October, when the jet is relatively weak. On the other hand, the latitudinal location varies between 2^{o} and 17^{o}N in NCEP and 2^{o}-15^{o}N in the model. However, there is a good relationship between modeled and observed wind speed (Figure 4.16) most especially with GD-MYJ-BMJ and WSM5-YSU-nSAS but with varying magnitude ranging from 10-$16ms^{-1}$. The wind speed magnitude of GD-MYJ-BMJ is in most instances stronger than the NCEP while that of WSM5-MYNN-nTDK is weaker. During

the pre-onset, the modeled location of the jet core is higher in April and lower between June and August when the monsoon is fully developed.

The upper-tropospheric jet around 150hPa is well known as the Tropical Easterly Jet (TEJ). Figure 4.17 shows the intensity and mean latitudinal location of the jet averaged between 10^{o}W and 10^{o}E. The TEJ creates a region of strong divergence in the upper-troposphere that aid the development of rain band over West Africa (Nicholson, 2009a; Nicholson & Grist, 2003). The maximum core of the TEJ meridionally displaced between 5^{o}S and 10^{o}N. It weakens and intensifies during the pre-monsoon (March) and monsoon season, respectively, with average speed ranging between 10-25ms^{-1}.

The model physics combinations can accurately simulate the seasonal evolution of TEJ maximum core but with different magnitudes. The magnitude of the jet in WSM5-MYNN-nTDK is closer to that of NCEP. In GD-MYJ-BMJ the jet is intensified and weakens in WSM5-YSU-nSAS relative to NCEP. However, the location of the jet core in the models is in most cases situated further northwards relative to NCEP. Within the model, the latitudinal location of the jet core lies between 10^{o}S and 15^{o}N.

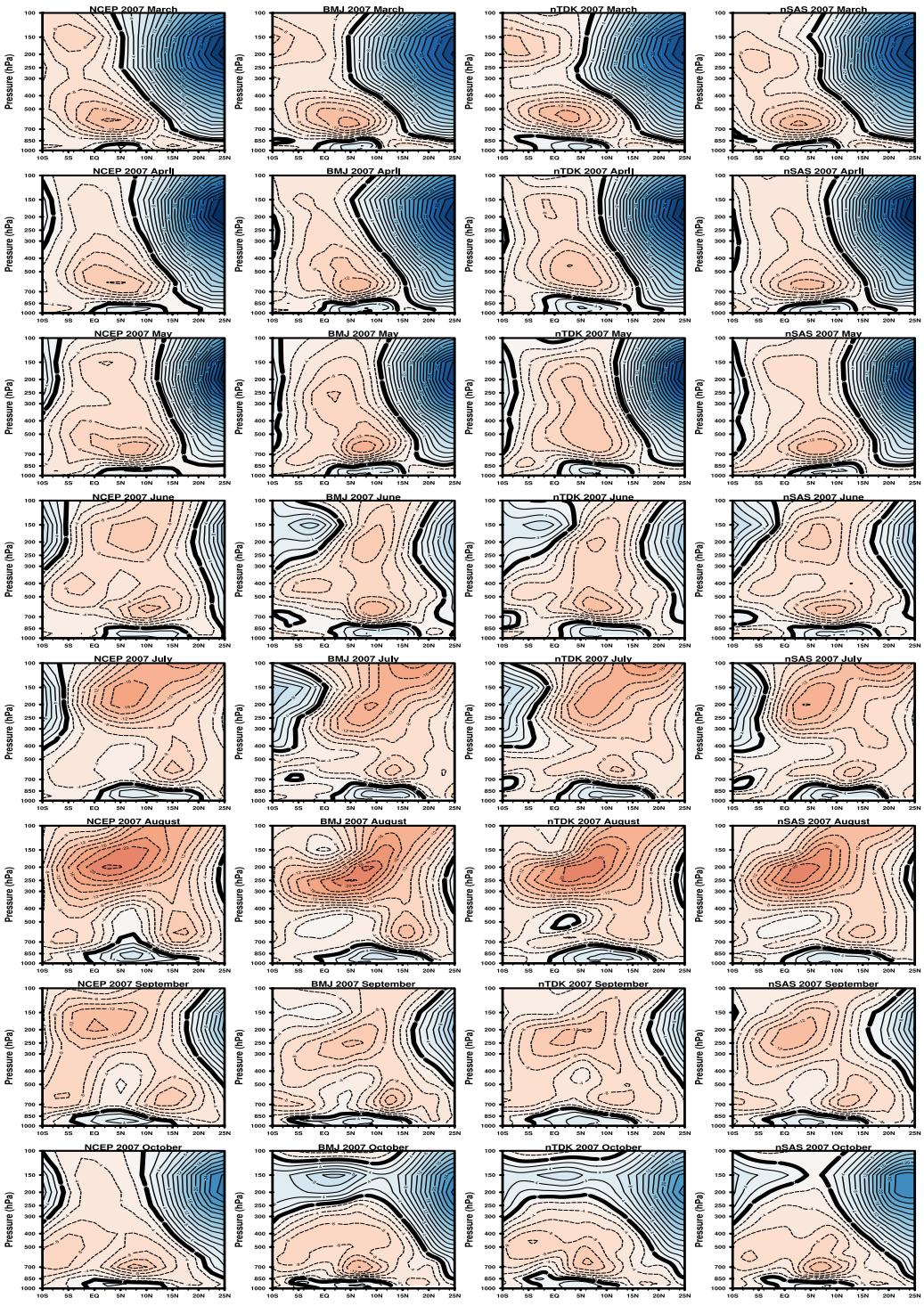

Figure 4.15: Mean Zonal Wind Speed (ms^{-1}) for Mar-Oct, Averaged on $10^{o}W$ and $10^{o}E$ for 2007.

NOTE: Each column of the panel plot represents (a) NCEP, (b) GD-MYJ-BMJ, (c) WSM5-MYNN-nTDK, and (d) WSM5-YSU-nSAS, respectively. The rows are plots of Mar-Oct.

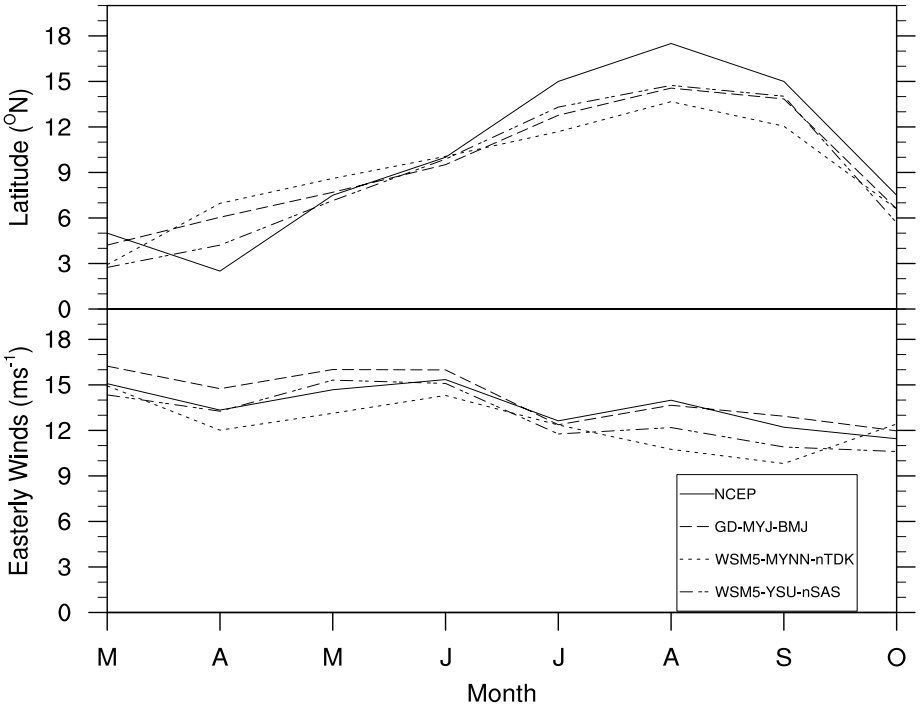

Figure 4.16: Mean Monthly Latitudinal Location and Intensity of AEJ Core Averaged Between 10°W and 10°E Longitudes for Mar-Oct.

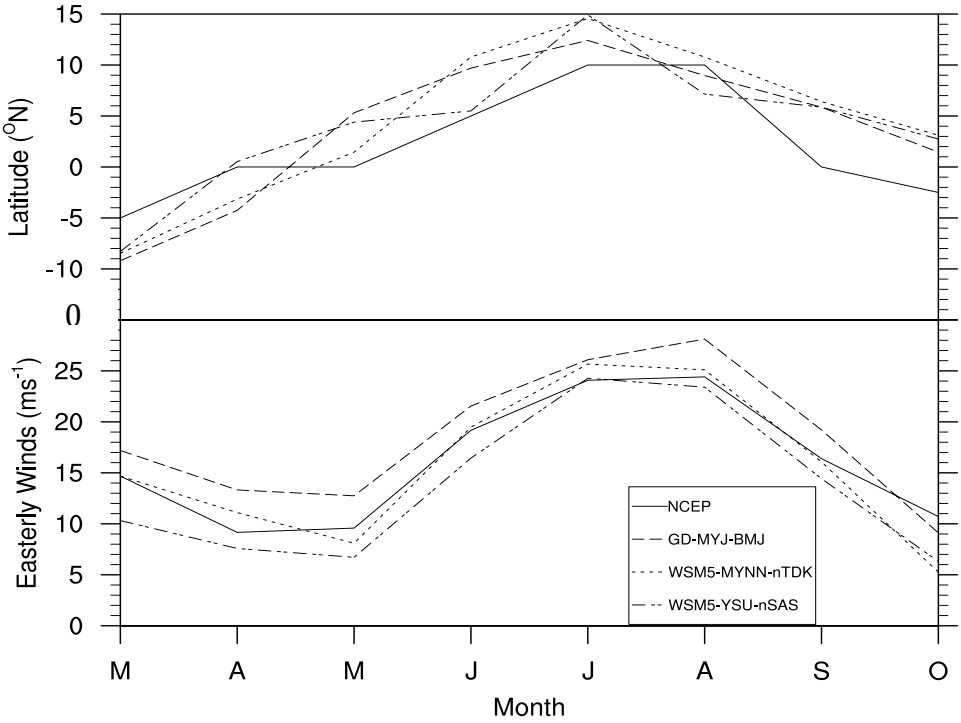

Figure 4.17: Mean Monthly Latitudinal Location and Intensity of TEJ Core Averaged between 10°W and 10°E for Mar-Oct.

4.2.4 Zonal Mean Temperature

The meridional cross-section of zonal mean temperature averaged over 10^{o}W and 10^{o}E during the Mar-Oct period is shown in Figure 4.18. The figure shows that the temperature field is characterized by a maximum in the lower troposphere at latitudes north of 10^{o}N and weak latitudinal gradients in the middle and upper troposphere from 5^{o}S to 25^{o}N. The maximum temperature advances northwards from 12^{o}N in March, when the maximum temperature is 304K, to about 23^{o}N in August, when the maximum temperature is 308K, and thereafter retreats southwards in September and October. The model physics combinations were able to simulate similar patterns. Most interestingly the northward advancement and southward retreat coupled with the maximum temperature is well reproduced by the prescribed model physics treatments.

The presence of the maximum temperature gradient, also known as the heat low (Nicholson, 2009a; Thorncroft et al., 2011), signifies the intense heating of the Sahara and its southern edge. Likewise, the northward advance is associated with the seasonal movement of the sub-Saharan rainband. The reversal of the temperature gradient has been argued to produce the AEJ (Nicholson & Grist, 2003). Nicholson & Grist (2003) also confirmed this assertion by comparing the zonal wind shear and thermal wind between 600 and 250hPa. They found a strong correlation between these two quantities and thus conclude that the reversal of the temperature gradient is responsible for the formation of the AEJ in the Northern Hemisphere.

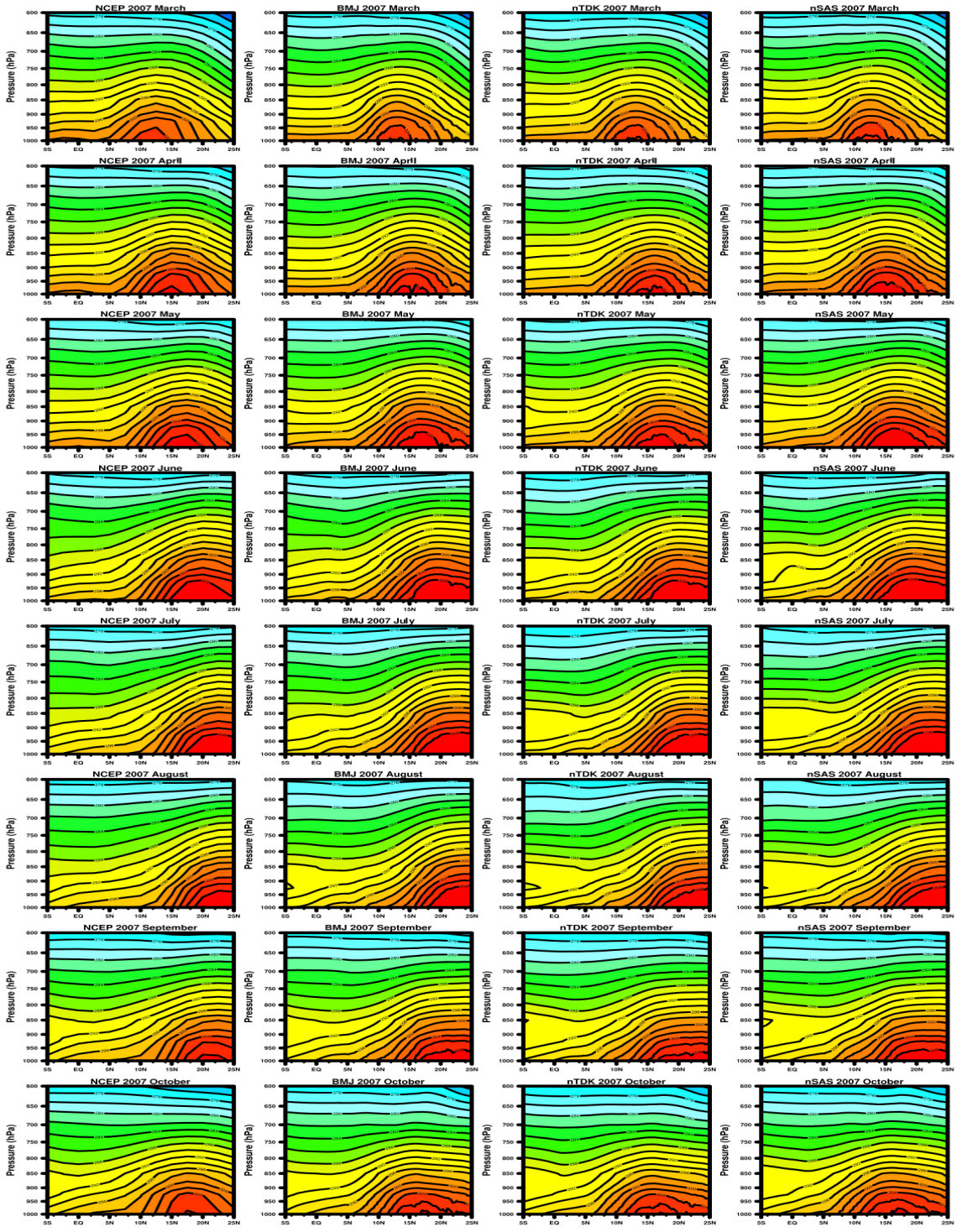

Figure 4.18: Vertical Cross-Section of 2007 Monthly Mean Temperature (K) for Mar-Oct Averaged between 10°W and 10°E

NOTE: Each column represents NCEP, GD-MYJ-BMJ, WSM5-MYNN-nTDK and WSM5-YSU-nSAS, respectively, while the plots in rows are figures from March to October.

4.2.5 Mean Vertical Motion

The stack plots of a vertical cross-section of mean vertical motion and rainfall averaged over 10°W and 10°E in August is shown in Figure 4.19. The figure shows two regions of maximum vertical motion and moisture flux convergence (Nicholson et al., 2008; Thorncroft et al., 2011). In the figure, the primary one lies between the mean position of AEJ (~15°N) and TEJ (~5°N). Thorncroft et al. (2011) described this region to be associated with deep meridional overturning and Nicholson & Grist (2003) as well termed it as the core of the rain band over West Africa. During August, when the monsoon is fully established, the mean location of this deep column of ascent is approximately situated around 10°N, which also corresponds to the area of rainfall maximum as well as the zone C_2 of weather zones (Dhonneur, 1971). This area of maximum moisture flux convergence and ascent is mostly associated with a deep column of moist air and possess relative humidity range of 60-80% in the troposphere (Nicholson, 2009a, 2009b). Nicholson (2008) also showed that the region corresponds with the southerly track of the African Easterly Waves.

On average, the models simulate the dominant area of moisture flux convergence and vertical motion at 12°N. GD-MYJ-BMJ reproduces two rainfall maxima at about 10°N and 13°N, which is likely due to the presence of two cores of vertical ascent zones within the dominant area of moisture flux convergence. The first, shallow ascent, resides in the lower troposphere (i.e. between 600-800hPa) at about 20°N and the second, deep ascent, lies within the mid- and upper troposphere (i.e. within 250-600hPa) at about 13°N. This emphasizes the role of vertical motion driven by convective activity and suggests that shallow vertical ascent with the availability of moisture may be responsible for more

rainfall in the model. Also, within the area of primary vertical motion and moisture flux convergence, WSM5-MYNN-nTDK and WSM5-YSU-nSAS simulate the observed asymmetrical rainfall distribution centered between 11^{o} and 12^{o}N, respectively. In WSM5-MYNN-nTDK, the structure of the vertical ascent appears not to be well defined around the lower atmosphere and thus results in the simulation of lower maximum rainfall amount. The rainfall maximum in WSM5-YSU-nSAS is comparable to that of GPCP, which may be explained by a well-defined structure of the vertical motion in the model that exists from the lower troposphere through to upper troposphere.

Another area of upward motion and moisture flux convergence is associated with the heat low over the Sahara (Nicholson, 2009a; Thorncroft et al., 2011; shown in Figure 4.18). The limit of this ascent is restricted within the low levels (Figure 4.19[upper panels]). Nolan et al. (2007) and Zhang et al. (2008) described this region as the shallow meridional overturning. Although, this area of ascent matches with the northern track of African Easterly Waves (AEW), waves in this path rarely produce rainfall (as shown in the lower panel of Figure 4.19). The rainfall maximum is situated about 8^{o} southwards from the core of this low-level ascent. Also, it marks the convergence zone of the northeasterly Harmattan and the southwesterly monsoon flow, known as the ITD. A region of subsidence separates the rainfall maximum and ITD (upper and lower panels of Figure 4.19), depicting that the ITD is clearly dissociated from the rain band.

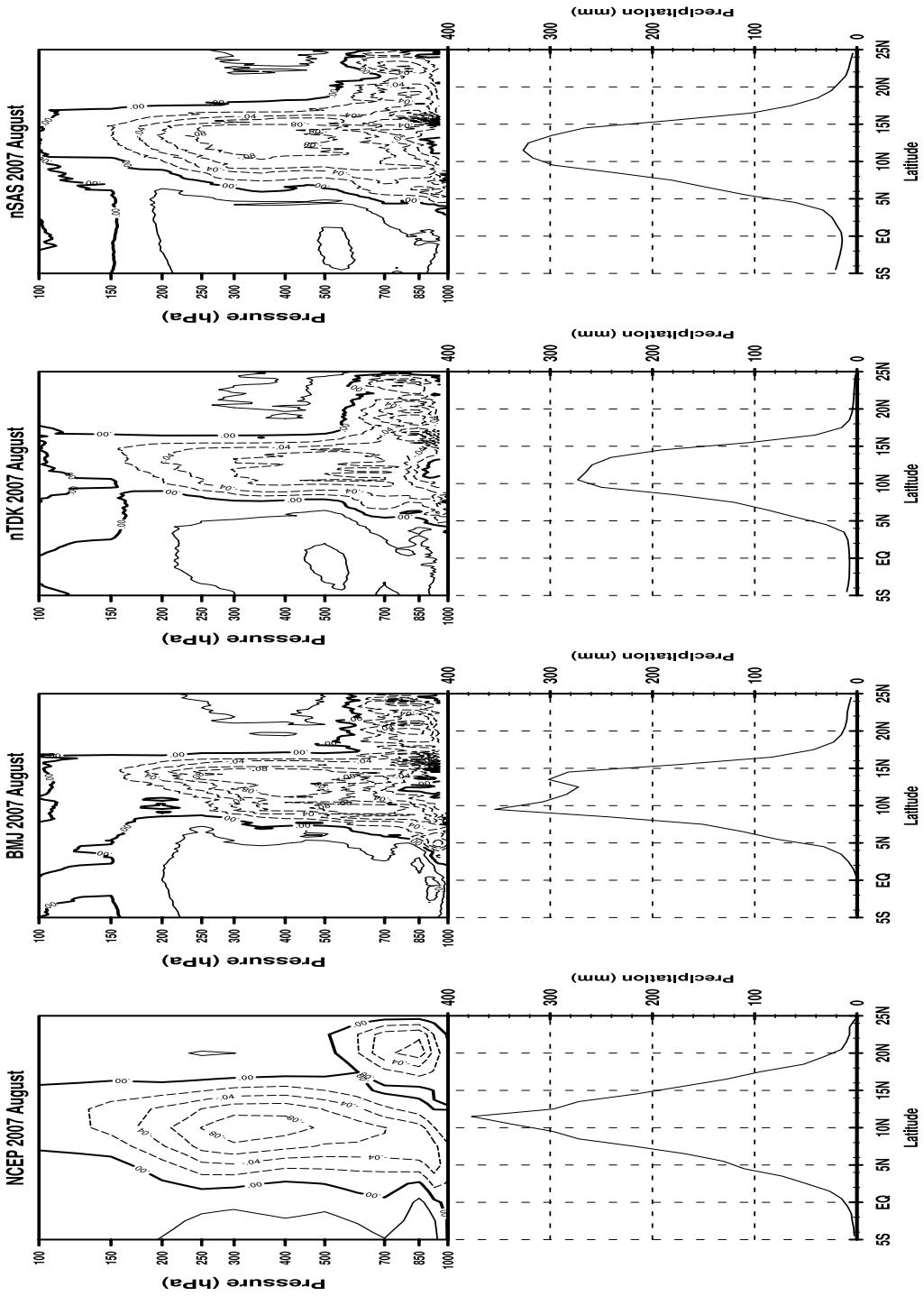

Figure 4.19: Schematic of the Rain Band over West Africa. Top Stack Plots are the Vertical Cross-Section of Mean Vertical Motion (Pa s^{-1}) Derived from NCEP and Models in August.

NOTE: The bottom plots show the mean August rainfall (mm/month) averaged over 10^{o}W to 10^{o}E along latitudes for GPCP and models.

The models reproduced the second region of ascent and moisture flux convergence though with slight differences compared with NCEP. The core of the ascent is located at about 8^{o} and 9^{o} northwards of the rainfall maximum in WSM5-YSU-nSAS and WSM5-MYNN-nTDK, respectively. In GD-MYJ-BMJ the core of the ascent is located at 7^{o} and 11^{o} northwards from the two rainfall maxima, which is due to the presence of two cores of vertical ascent zones within the dominant area of moisture flux convergence. The magnitude of the rainfall maximum simulated in WSM5-YSU-nSAS is comparable to GPCP. South of the dominant ascent and aloft the shallow ascent is prevailing subsidence. Upper panel of Figure 4.19 shows that a region of subsidence separates the rainfall maximum and the ITD, denoting that the ITD is well decoupled from the rain band. This region of subsidence is not clearly present in the models. The two regions of ascent are however found to merge during wet monsoon years (Nicholson, 2008).

4.3 WET AND DRY WAM RAINFALL SEASONS

In this section additional long-term (8months) simulation of the WAM season is performed and analyzed. The focus here is to understand how the WRF model physics influence the characteristics of selected wet (2008 and 2010) and dry (2001 and 2011) WAM years (identified from Figure 3.3), mostly, in term of the amount of observed and simulated rainfall, temperature, specific humidity, and large-scale circulation.

4.3.1 Rainfall Seasonal Cycle

Rainfall is a very important parameter for water-dependent activities that highly varies with time and space in the West African region. For instance, Figure 4.20 presents

the average daily precipitation for each of the climatic zones (Guinea coast, Savannah and Sahel) during the wet and dry year composites. The seasonality of the monthly mean of daily rainfall shows regional variance, thereby highlighting the distinct spatial complexity of the WAM. Figures 4.20a and b shows the well-established two rainfall peaks, which is associated with the meridional migration of the ITD (Nicholson, 2013; among others) and postulated "monsoon jump" (Le Barbé et al., 2002; Sultan & Janicot, 2000), in June and September over the Guinea coast. These peaks are observed for both wet and dry summer monsoon seasons with observations and model outputs. However, there are variations in magnitude most especially during the wet monsoon. In Savannah (Figures 4.20c and d), a single peak is observed. The peak was observed in August (September) for wet (dry) monsoon year. The models reasonably agree in dry years, unlike the wet years where only the WSM5-MYNN-nTDK simulates its peak in September. The more homogeneous Sahel zone showed a single peak in August (Figures 4.20e and f). The WSM5-MYNN-nTDK underestimated the observed precipitation in both monsoon composites while WSM5-YSU-nSAS overestimates the observed precipitation mostly in dry monsoon. However, all the model simulations show good agreement in the Sahel.

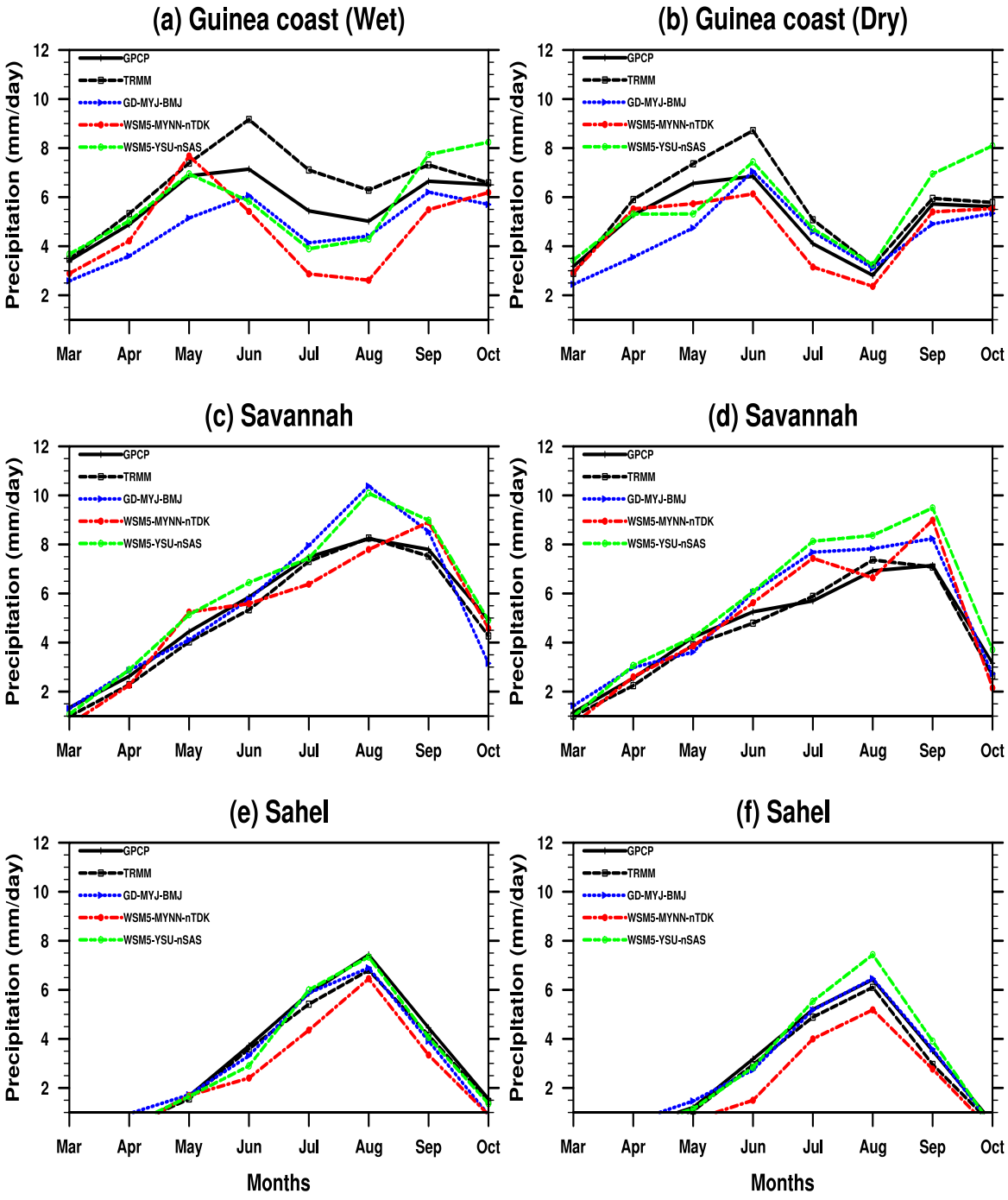

Figure 4.20: Seasonal Cycle of Area-Averaged Precipitation over the Guinea Coast, Savannah, and Sahel Climatic Zones from the Three Experiments, TRMM and GPCP Observation during Wet (a, c and e) and Dry (b, d and f) year's composite.

4.3.2 Rainfall Distribution

The rainfall climatology of wet and dry composites of the West African summer monsoon season is analyzed. Figure 4.21 depicts the spatial distribution of mean rainfall for the period June-September (JJAS) derived from the composites of wet and dry years for GPCP, TRMM, and the three model experiments as well as the model differences relative to the GPCP. During JJAS, the spatial distribution of observed rainfall exhibits a meridional gradient with rainfall decreasing in intensity from the Guinea coast to the Sahel in association with the latitudinal migration of the ITD, which combines with the Saint Helena anticyclonic high pressure to control the monsoon wind that determines the amount of moisture influx into the region (Sultan & Janicot, 2003). The observed localized maxima over the Jos Plateau, Cameroun Mountains and over the west coast of Guinea along 5^{o}-10^{o}N and Fouta-Djallon highlands are reproduced in the wet and dry year composites. Also, over this terrain, the observed rainfall amount is higher in the wet than the dry WAM season (Im et al., 2014; Sultan & Janicot, 2003).

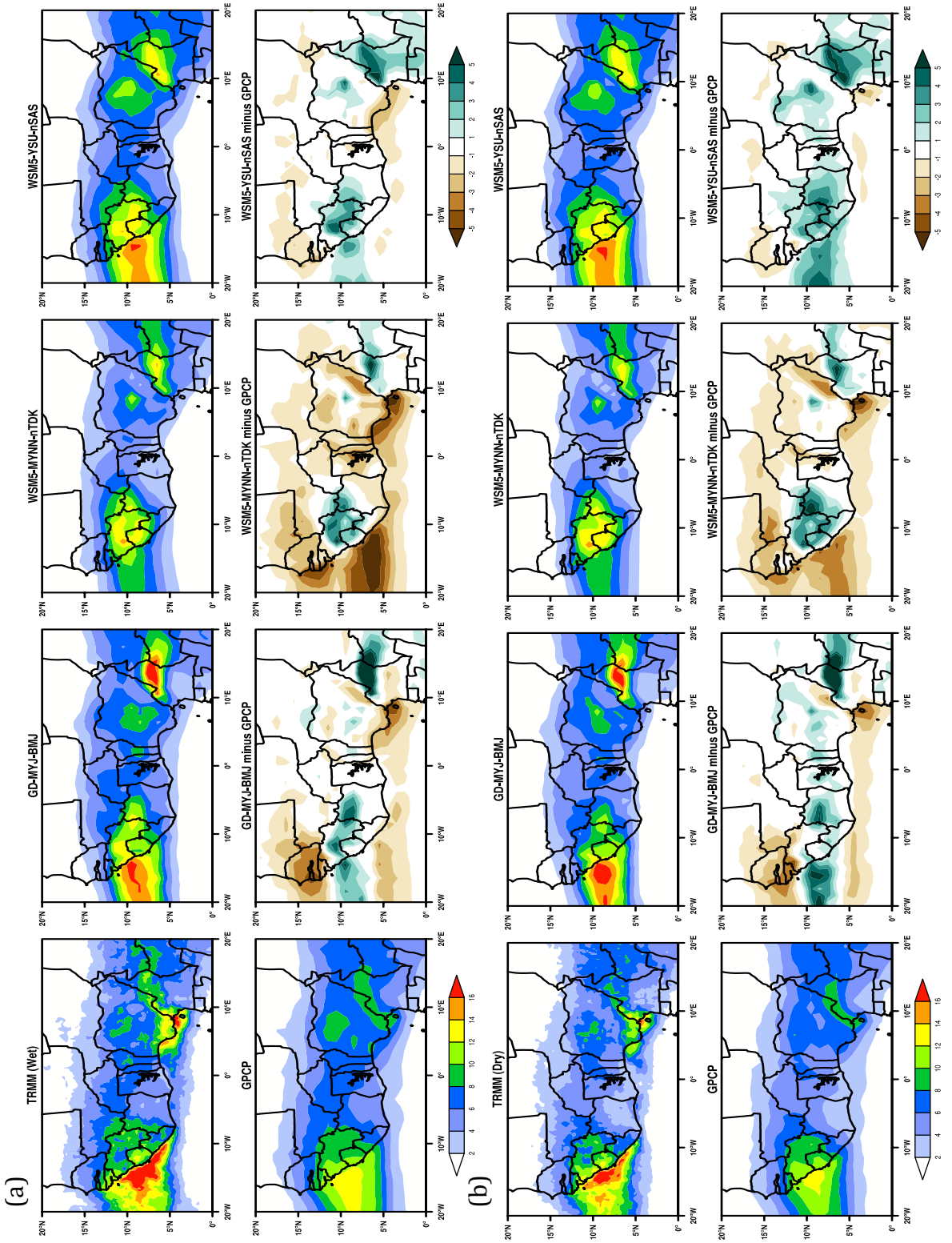

Figure 4.21: Spatial Distribution of Mean (a) Wet Year (2008 and 2010) and (b) Dry Year (2001 and 2011) Composite Boreal Summer (JJAS) Precipitation (mm day^{-1}) from the TRMM and GPCP Observations, Three Experiments, and their Differences with GPCP Observations.

Although both wet and dry composites show similar observed features, they exhibit some difference in spatial magnitudes. During wet WAM year, GD-MYJ-BMJ (bottom panel of Figure 4.21a) overestimates rainfall between 1 and 5mm day^{-1} offshore of the west coast of Guinea, over the Fouta-Djallon and Cameroun Mountains. The same combination shows the dry bias of about 3mm day^{-1} in the western part of the region above 10^{o}N and southern coast of Guinea along 5^{o}N latitude. On the other hand, GD-MYJ-BMJ simulated increased wet bias above 4mm day^{-1} and decreased dry bias below 3mm day^{-1} in dry WAM season (bottom panel of Figure 4.21b). The WSM5-MYNN-nTDK combination simulates extensive spatial coverage of dryness above 4mm day^{-1} over the ocean and 2mm day^{-1} or less in most parts of land areas in the wet WAM season. Also, the combination produces 3-5mm day^{-1} wetness over the Fouta-Djallon, Jos Plateau and Cameroun Mountains. The intensity of the dry (wet) biases decreased (increased) significantly during the dry (wet) WAM season mostly over the Ocean. For the WSM5-YSU-nSAS combination, the model agrees well with the observed spatial pattern by producing much less dry bias of 3mm day^{-1}, compared with other simulations, over some small spatial areas in both wet and dry WAM season, but, it, however, overestimates by more than 3mm day^{-1} over high terrain. Similar to the WSM5-MYNN-nTDK, the magnitude of the dryness (wetness) in the WSM5-YSU-nSAS simulation decreased (increased) during the dry (wet) WAM season. On average, WSM5-MYNN-nTDK simulations are relatively dry, GD-MYJ-BMJ is moderately wet and dry while WSM5-YSU-nSAS are comparatively wet with respect to GPCP.

The common shortcoming in all simulations appears around the Cameroun Mountains, Jos Plateau and over the Fouta-Djallon extending towards the western coast

of Guinea. All models fail to accurately capture the intensity of the localized maximum over these high terrains regardless of the cloud microphysics, cumulus convection and planetary boundary layer schemes used, thus showing a significant dry and wet spatial biases. Such systematic biases displayed in the models are not limited to the simulations of the current study, but appears to be a quite typical error found in many other regional climate simulations over West Africa (Flaounas et al., 2011; Gbode et al., 2019; Im et al., 2014; Klein et al., 2015; Sylla et al., 2009; Zaroug et al., 2013). Differences between the three model combinations can be explained by the difference in the physics used (Gbode et al., 2019; Klein et al., 2015; Nikulin et al., 2012). For instance, both GD-MYJ-BMJ and WSM5-MYNN-nTDK use a local closure PBL scheme, that is, MYJ and MYNN, where the eddy diffusion coefficients are derived from their prognostic Turbulent Kinetic Energy (TKE). Contrarily, WSM5-YSU-nSAS uses a non-local closure scheme with a parameter that allows enhanced vertical mixing and entrainment of air from above the PBL even in a neutral boundary layer where the vertical gradient of potential temperature is zero (Hong et al., 2006). This difference allows the combination with YSU PBL to possess enhanced deep convection and thus produce more spatial wetness relative to other combinations as a result of a stronger water cycle possibly due to increased evaporation associated with a more strongly mixed PBL, which serves as a source for consistent production of more vertical transport by convection into the troposphere (Ulate et al., 2014). Also, the profile adjustment convection scheme (BMJ) appears to produce less fraction of total rainfall (approximately 75% or less) compared with the mass flux nTDK and nSAS CU schemes (not shown), which can produce total rainfall fraction of 80% and above.

To further evaluate the model's ability to reproduce different WAM seasons, the quantitative measure of rainfall produced in the model relative to observations is given in Table 4.6. Table 4.6 presents the total rainfall amount over the three different climatic zones; the bold values indicate cases where wet years are consistent in both observations and models. This was done to examine how well the models can distinguish between wet and dry years. The skill of individual models to distinguish wet and dry years will give more confidence in its ability to show climate change signals in future work. Observed rainfall amounts agree quite well and are consistent for wet and dry years in GPCP and TRMM, however, the latter appears to have more rainfall in the Guinea Coast where the differences are large. GD-MYJ-BMJ skillfully reproduced the selected wet and dry years in the three climatic zones, though, with varying magnitudes. WSM5-MYNN-nTDK failed to reproduce one of the two wet years in Guinea Coast but was however skillful in distinguishing the different WAM seasons over Savannah and Sahel. In WSM5-YSU-nSAS, the model appears to have difficulty in differentiating wet and dry years in the Guinea coast and Sahel regions. The inabilities of some of the models to differentiate the selected WAM seasons suggest that they are unable to reproduce the peak phase of some observed rainfall events (as shown in Figure 4.2). This was also seen clearly in Figure 4.20a where the June peak is missed.

Table 4.6: Total Rainfall for Wet and Dry Monsoon Seasons over the Three Climatic Zones. The Bold Values Indicate Cases where Wet Years are Consistent in Both Observations and Models.

Monsoon	Year	GPCP	TRMM	GD-MYJ-BMJ	WSM5-MYNN-nTDK	WSM5-YSU-nSAS
		Guinea Coast				
Dry	2001	1291.2	1423.5	1069.1	1106.7	1326.0
	2011	1153.7	1311.5	1109.1	1132.2	1385.2
Wet	2008	**1421.6**	**1607.5**	**1136.9**	**1202.4**	**1436.1**
	2010	**1367.0**	**1592.3**	**1174.4**	1076.2	1340.7
		Savannah				
Dry	2001	1155.7	1121.0	1254.0	1135.4	1367.3
	2011	1049.7	1014.9	1224.1	1183.1	1324.8
Wet	2008	**1330.2**	**1260.4**	**1359.8**	**1281.1**	**1405.1**
	2010	**1276.6**	**1184.8**	**1336.4**	**1251.2**	**1461.1**
		Sahel				
Dry	2001	671.6	602.6	652.3	460.9	722.8
	2011	588.4	557.8	621.4	450.3	616.1
Wet	2008	**764.5**	**708.2**	**702.8**	**596.3**	671.0
	2010	**774.4**	**730.3**	**752.4**	**604.7**	**790.8**

One important atmospheric variable that can be used to explain the variability of the West African climate is the rainfall (Hulme, 1992; Nicholson, 1989). Rainfall in the region responds to latitudinal evolution of rain belt, defined by the mean surface position of the ITD, which is tightly coupled with the displacement of the ITCZ over the western coast of West Africa. This interaction gives way to the abrupt northward migration and gradual southward retreat of the rainfall during the monsoon cycle (Hagos & Cook, 2007b; Hernández-Díaz et al., 2013; Le Barbé et al., 2002; Lebel et al., 2003; Nikulin et al., 2012; Sultan & Janicot, 2000). GPCP, TRMM and the three experiments are used to place and compare the composites of wet and dry summer monsoon in an interannual perspective. Time-Latitude cross-sections that display the evolution of the monthly rainfall, averaged between longitudes 10^{o}W and 10^{o}E, over West Africa for the monsoon composites are presented in Figure 4.22. The seasonal migration and retreat of the monsoon are nonlinear, indicated by northward monsoon jump of maximum rainfall.

From GPCP (Figures 4.22a and f), the first major quasi-stationary monsoon core appears near 5^{o}N in mid May for wet and dry years, which corresponds to the onset of the monsoon along the Guinea coast, whereas TRMM (Figure 4.22b and g) shows that the core near the same latitude extends further into June for both composites. All simulation combinations also simulate the core near 5^{o}N but with a different magnitude in May during wet years. This result is consistent with previous findings that both the observations and simulations portray abrupt transitions for the monsoon onset, maximum and retreat with differing intensities (Eltahir & Cuiling Gong, 1996; Im et al., 2014; Sultan & Janicot, 2000; among others). In contrast, the models simulate the core near 5^{o}N later in June for dry composite. The distribution in WSM5-MYNN-nTDK extends from

April to June. The results of the models suggest that the monsoon onset is early (late) in wet (dry) monsoon years around the Guinea coast.

The second high-intensity rain belt jumps towards the Sahel region and the maximum core is observed around 11^{o}N in August, when the monsoon reaches its peak, with differing magnitudes for wet and dry years. In TRMM, the maximum core extends northwards from 9^{o}N to 11^{o}N and the rainfall amount in this phase is less than that in the first phase for both composites. Further, the monsoon retreats toward the Guinea coast around October, which marks the end of the season. During the wet year, all models simulate the maximum rainfall core between 9-10^{o}N in August. In GD-MYJ-BMJ, the core is displaced southwards and that of WSM5-MYNN-nTDK extends to September. For the dry year, the models maintain the mean latitudinal position but simulate an extended maximum rainfall core from July through to September. The core in September linearly extends southwards in WSM5-YSU-nSAS. Also, all simulations reproduce a noticeable core in September as well as southwards displacement of the maximum rainfall core.

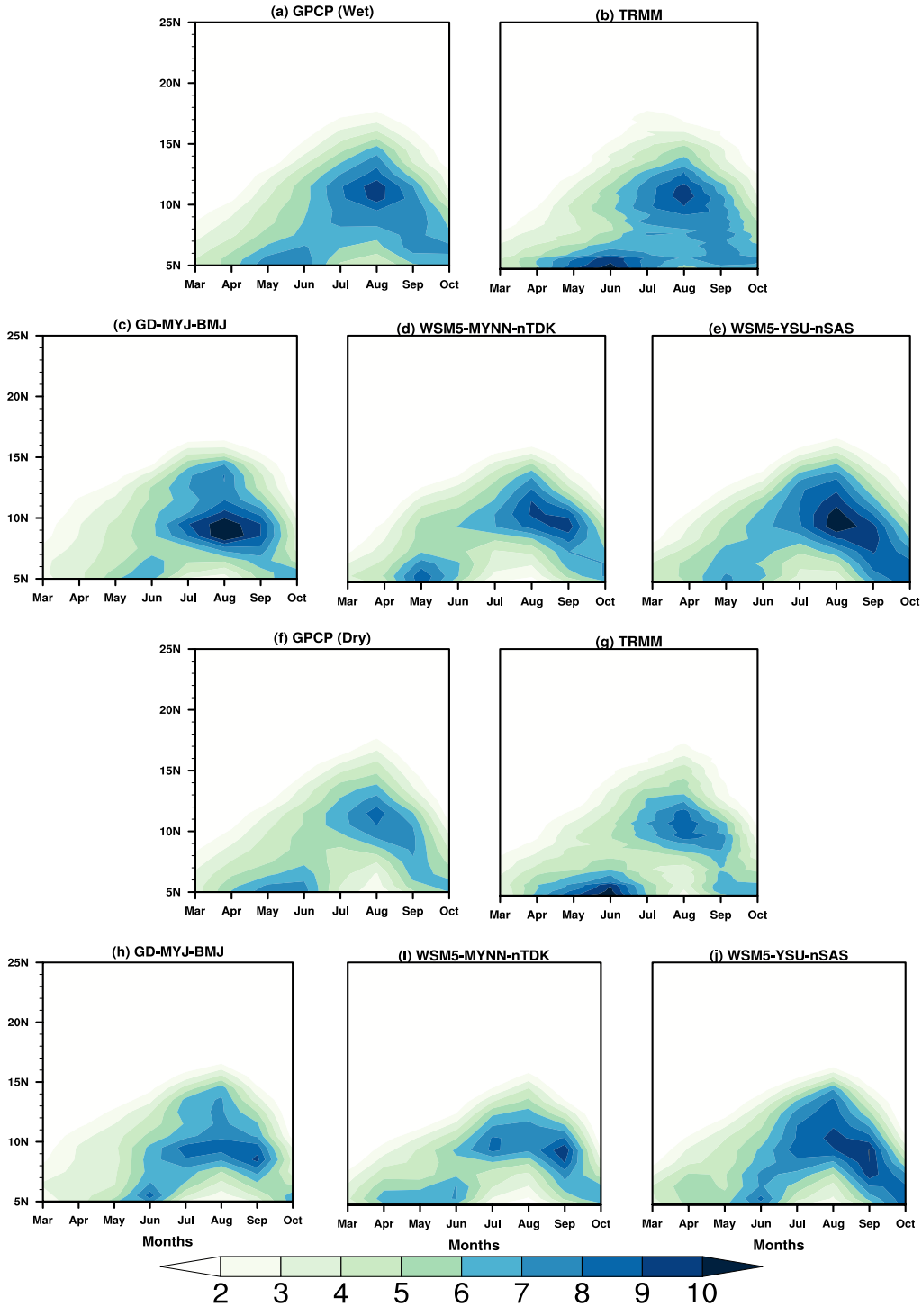

Figure 4.22: Latitude–Time Cross-Section of Monthly Mean Precipitation (mm day^{-1}) Averaged from 10^{o}W to 10^{o}E from TRMM, GPCP Observations and the Three Experiments Averaged over the (a-e) Wet Year (2008 and 2010) and (f-j) Dry Year (2001 and 2011) Composites.

4.3.3 Vertical Structure of Temperature and Humidity

The vertical cross-section of zonal mean temperature averaged over 10^{o}W and 10^{o}E and the patterns of the model bias during June through to September (JJAS) for wet and dry years composite is presented in Figure 4.23. A stratified region of maximum (minimum) temperature dominates the lower (upper) troposphere and a weak stratification at mid-layer. The core of the maximum temperature in the lower atmosphere around latitude 24^{o}N corresponds to the Saharan Heat Low (SHL). This climatological feature appears in both dry and wet years. SHL describes the existence of intense heating of the Sahara (Nicholson, 2009b; Thorncroft et al., 2011). Similarly, the two simulated monsoon composites reasonably replicate the vertical temperature gradient but with varying magnitude (like Figure 4.18). A common characteristic of the models is an overestimation of temperature up to about 4^{o}C over land. This feature intensifies as it extends northwards from 5^{o}N and around 11^{o}N in the lower and mid-troposphere, respectively. This indicates a warm tropospheric bias over the Sahara Desert in the model regardless of the physics difference tested. Also, a compensating cold region resides in the upper atmosphere. These structures are seen in the two composites and they, however, possess wider coverage aside from their intensification in dry years.

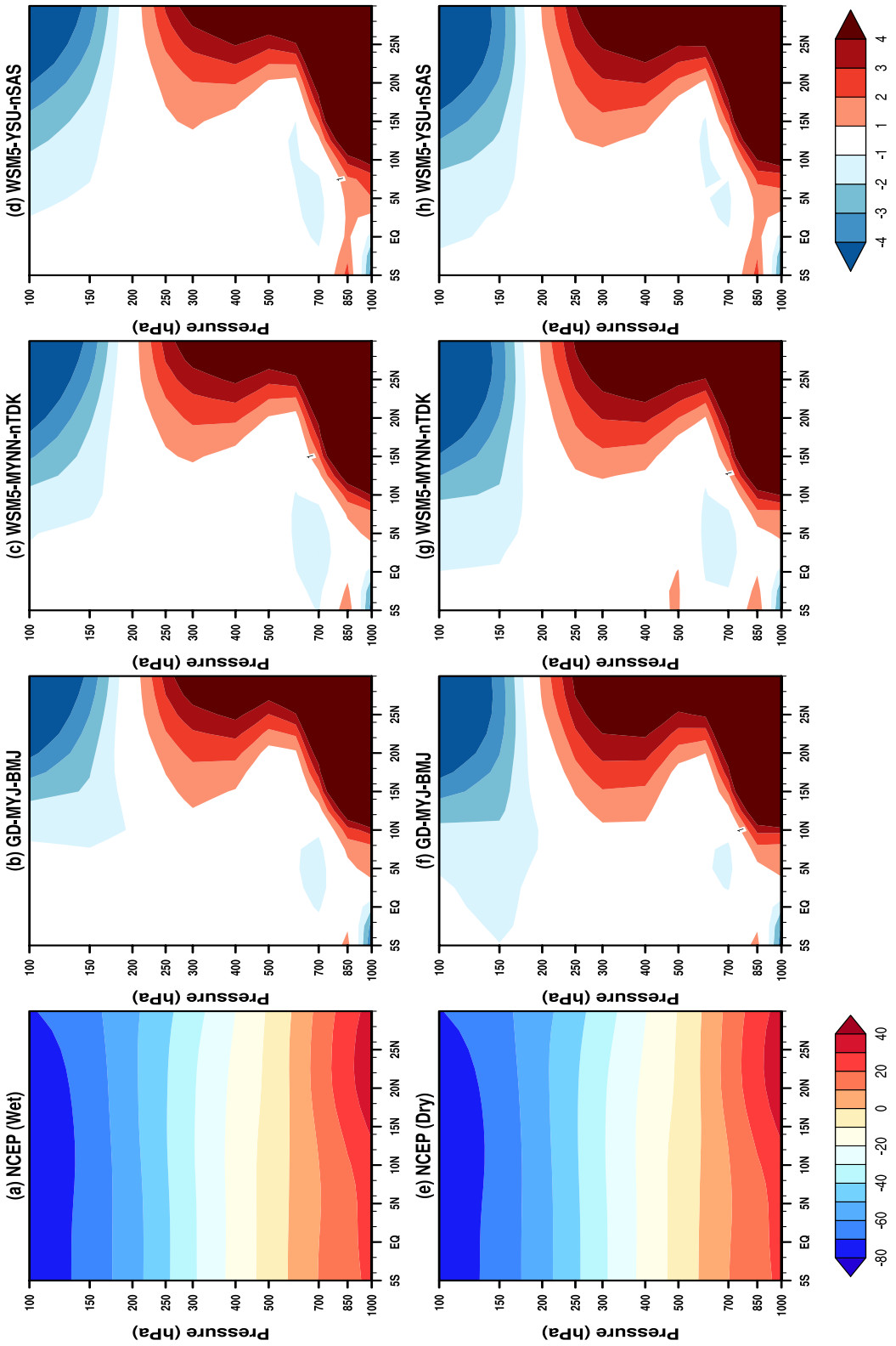

Figure 4.23: Vertical Cross-Section of JJAS Mean Temperature (^{o}C) Averaged over 10^{o}W–10^{o}E from NCEP, and the Differences between the Three Experiments and NCEP for Wet Year (2008 and 2010) (Top Panels) and Dry Year (2001 and 2011) (Bottom Panels) Composites.

Figure 4.24 depicts the vertical cross-section of JJAS mean specific humidity averaged over longitudes 10^{o}W-10^{o}E and the differences between the three model experiments for wet and dry composites. Unlike temperature that is isothermal along latitudes, specific humidity decreases with increasing latitudes. In JJAS the mean core of maximum is situated at about latitude 10^{o}N. This characteristic is peculiar in both wet and dry composites. All simulations underestimate (overestimate) atmospheric moisture over the ocean (land) and Sahel region. This explains the overestimation of rainfall over the expected region of maxima and other areas of West Africa (as shown in Figure 4.21). The models also overestimated the maximum at 10^{o}N with other similar bias patterns over ocean and land areas for wet and dry composites. A warm bias over land areas can, however, enhance the excessive moisture that can lead to higher moist static energy, which could cause an increase in the convective available potential energy and thus create a favorable environment for induced convection (Eltahir, 1998; Findell & Eltahir, 2003).

4.3.4 Large-Scale Circulation

The model performance in reproducing the large-scale circulation is assessed at three levels to gain useful insight about the simulated three-dimensional dynamical structure of the WAM system. Figure 4.25 displays wind vectors at 850, 650 and 150hPa averaged for August derived from the three simulations driven by ERA-Interim (and NCEP FNL soil only) as well as the NCEP reanalysis. To conserve the properties of dynamic fields and reduce excessive cancellation effects only the results of August, which represents the peak of WAM activity, is presented for both wet and dry composites instead of the mean JJAS.

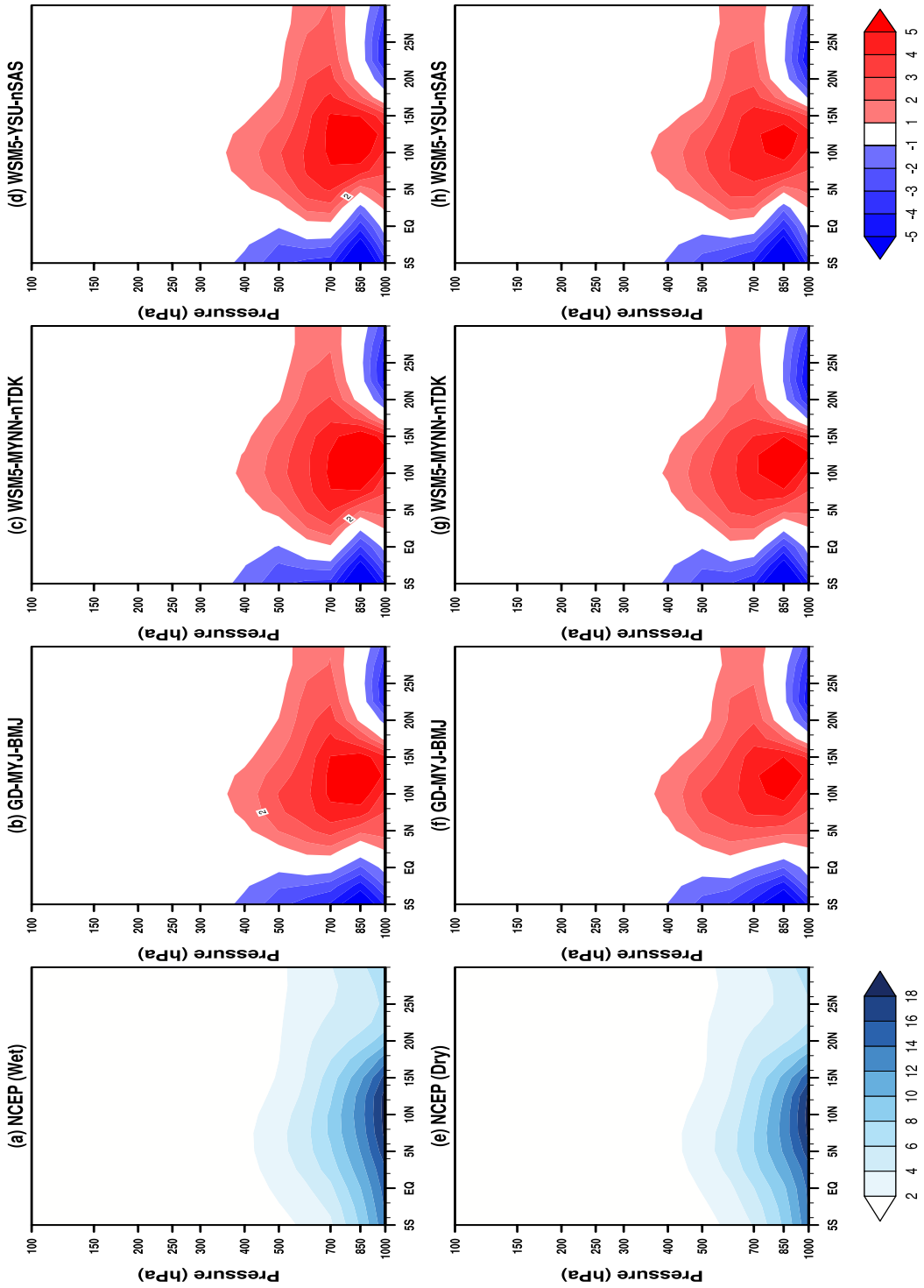

Figure 4.24: Vertical Cross-Section of JJAS Mean Specific Humidity (g kg^{-1}) Averaged over 10°W–10°E from NCEP, and the Differences between the Three Experiments and NCEP for Wet Year (2008 and 2010) (Top Panels) and Dry Year (2001 and 2011) (Bottom Panels) Composites.

At low levels (850hPa; top plots of Figure 4.25a and b), the NCEP reanalysis shows that a westerly monsoon flow dominates the Guinea coast and Savannah zones. This flow transports moisture from the Atlantic Ocean into the region. North of 20^{o}N the winds are predominantly north easterlies that carry dry and dusty air into the region. Where the two trade winds meet overland denotes the ITD position. The simulations all reproduce these observed features at low levels except for WSM5-MYNN-nTDK, which simulated stronger westerly monsoon flow in the wet season along the Guinea coast. In the wet WAM composite, WSM5-MYNN-nTDK and WSM5-YSU-nSAS simulations agree well with the observed monsoon flow, though WSM5-MYNN-nTDK simulates much stronger winds around the Cameroun Mountains. For GD-MYJ-BMJ, the wind magnitude is also high over the Cameroun Mountains and the moisture influx is less due to easterlies along the south coast, which weakens the monsoonal flow. Also, the GD-MYJ-BMJ and WSM5-MYNN-nTDK simulations reproduce the westerly monsoon flow further north. For the dry composite, there is a general increase in winds over the Cameroun Mountains. GD-MYJ-BMJ simulates an anticyclonic flow over the southwestern coast of the region. Likewise, the moisture flux extends further inland in all simulations.

At middle levels (650hPa), strong easterly flow associated with the AEJ dominates (middle plots of Figure 4.25a and b). All simulations capture the major characteristics of the flow patterns at this level as they agree well with the observed maximum intensity and average location of maximum in NCEP. However, the simulations were unable to simulate the observed weak easterlies along the south coast of the region. During wet years easterly winds are weaker which is necessary to allow more

influx of moisture into the region that favors convective activity (Dezfuli & Nicholson, 2011; Grist & Nicholson, 2001). Though GD-MYJ-BMJ simulates stronger easterlies over the Guinea coast, it reproduces a better zonal band of AEJ. In WSM5-MYNN-nTDK and WSM5-YSU-nSAS, the intensity of the AEJ belt decreases eastward. For dry years, the observed and modeled AEJ intensifies and there is a noticeable increase in coastal easterlies. The meridional extent of the AEJ belt increases in all simulations. WSM5-MYNN-nTDK exhibits the strongest winds and extends southwards to the coast of the region. This causes the depth of the low-level moisture flux to decrease and in turn, bring about a reduction in rainfall amount (as shown in Figure 4.21).

Finally, at upper-level (150hPa), there is a strong wide zonal band of easterlies associated with the TEJ, which is caused as a result of mass outflow around the Himalayas. This zonal band of easterlies extends across the Guinea region. Also, noticeable is westerly winds north of the WAM domain. The strong upper tropospheric flows and the resultant divergence are consistent with the simulated low-level convergence, which enhance the rising motion of moist and warm air from near the surface (see Figure 4.19). The simulations can reproduce these two major observed features of the upper-level flow. Further, the simulations reproduce the observed TEJ intensification during the wet year and weakening in the dry year. This suggests that the model can allow the mass outflow from the Himalayas to propagate into it at the southeastern corner of the model domain but at higher magnitudes most especially in dry years. The TEJ is described to play a role in the development of the rain belt over West Africa (Nicholson, 2009a; Nicholson & Grist, 2003).

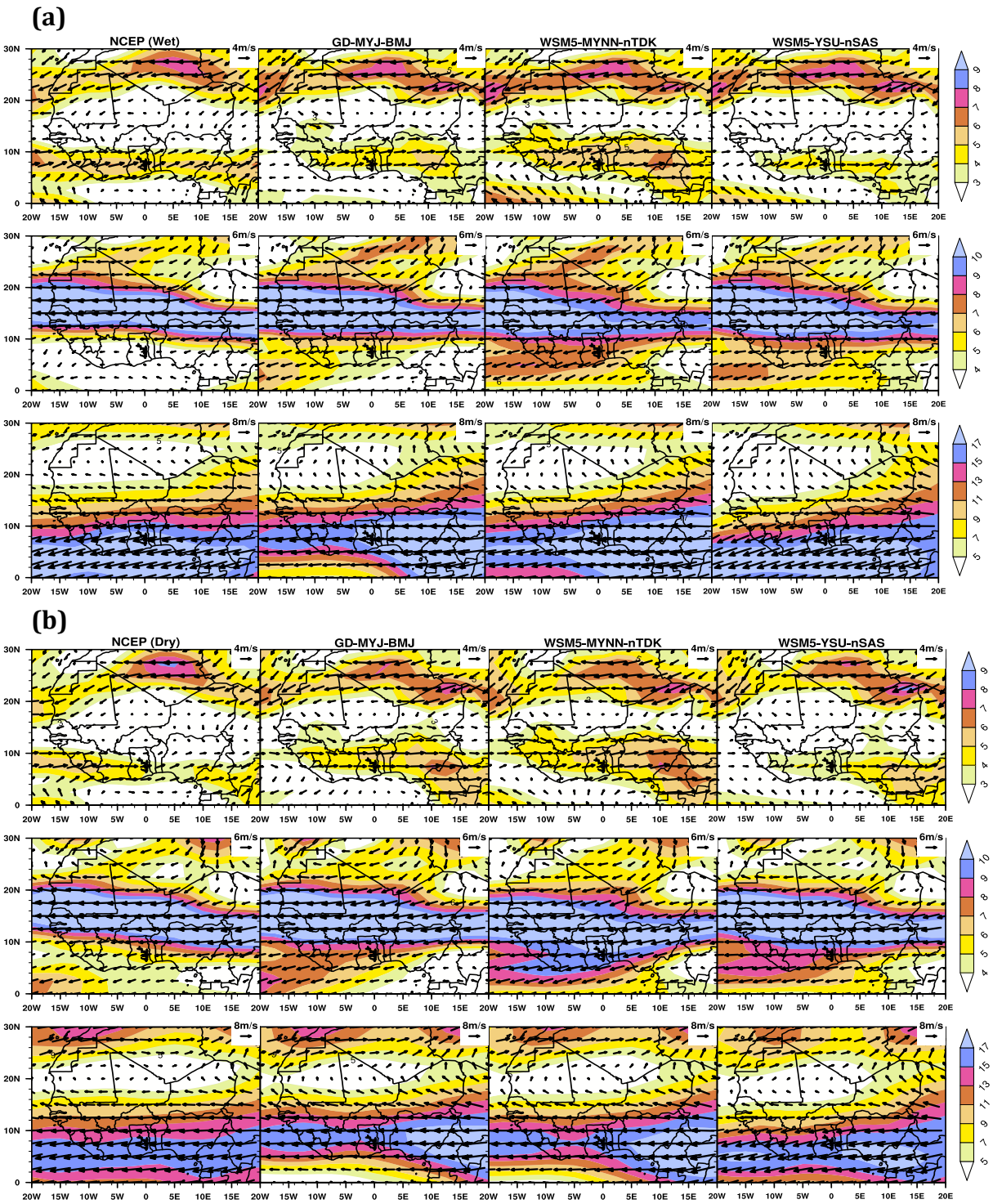

Figure 4.25: Spatial Distribution of Wind Vectors at 850 (Top), 650 (Middle), and 150 hPa (Bottom) Averaged for August from the Three Simulations and NCEP.

NOTE: The color shading indicates the magnitude of the wind (m s^{-1}) for (a) wet year (2008 and 2010) and (b) dry year (2001 and 2011) composites.

Figure 4.26 depicts the vertical structure of the zonal wind averaged from 10°W and 10°E longitudes for August. The vertical structure portrays the stratified behavior of the atmospheric circulation with three major components. The prevailing westerly flow up to 850hPa describes the monsoon flow and the two easterly maxima centered on 650hPa and 200hPa describe the AEJ and TEJ, respectively. The westerly monsoon flow dominates between the equator and beyond 15°N. The position and intensity of the monsoon flow is an important factor that determines the magnitude and spatial distribution of rainfall in the region. From NCEP the depth of the monsoon extends further upwards and its core shifts northward in wet year contrary to the dry year. All simulations reproduce this characteristic but with a broader zonal extent. However, the strength of the simulated monsoon flow for both composites is comparable with the reanalysis.

The AEJ is a paramount feature of the WAM dynamics and it is associated with strong baroclinic atmospheric conditions caused by the strong meridional surface temperature gradient and moisture between the Sahara and equatorial Africa (Cook, 1999; Newell & Kidson, 1984; Thorncroft et al., 2003; Thorncroft & Blackburn, 1999). All simulations reasonably reproduce the mean position of the AEJ centered on 650hPa for wet and dry composites. Also, all the simulations reproduced intensified AEJ in the dry year as well as a shift of the jet core southwards from the average latitudinal position of 15°N.

Considering the TEJ, all simulations reasonably reproduce the strength, depth and latitudinal position compared with NCEP composites. The models also simulate the downward extension of the jet core in a dry year.

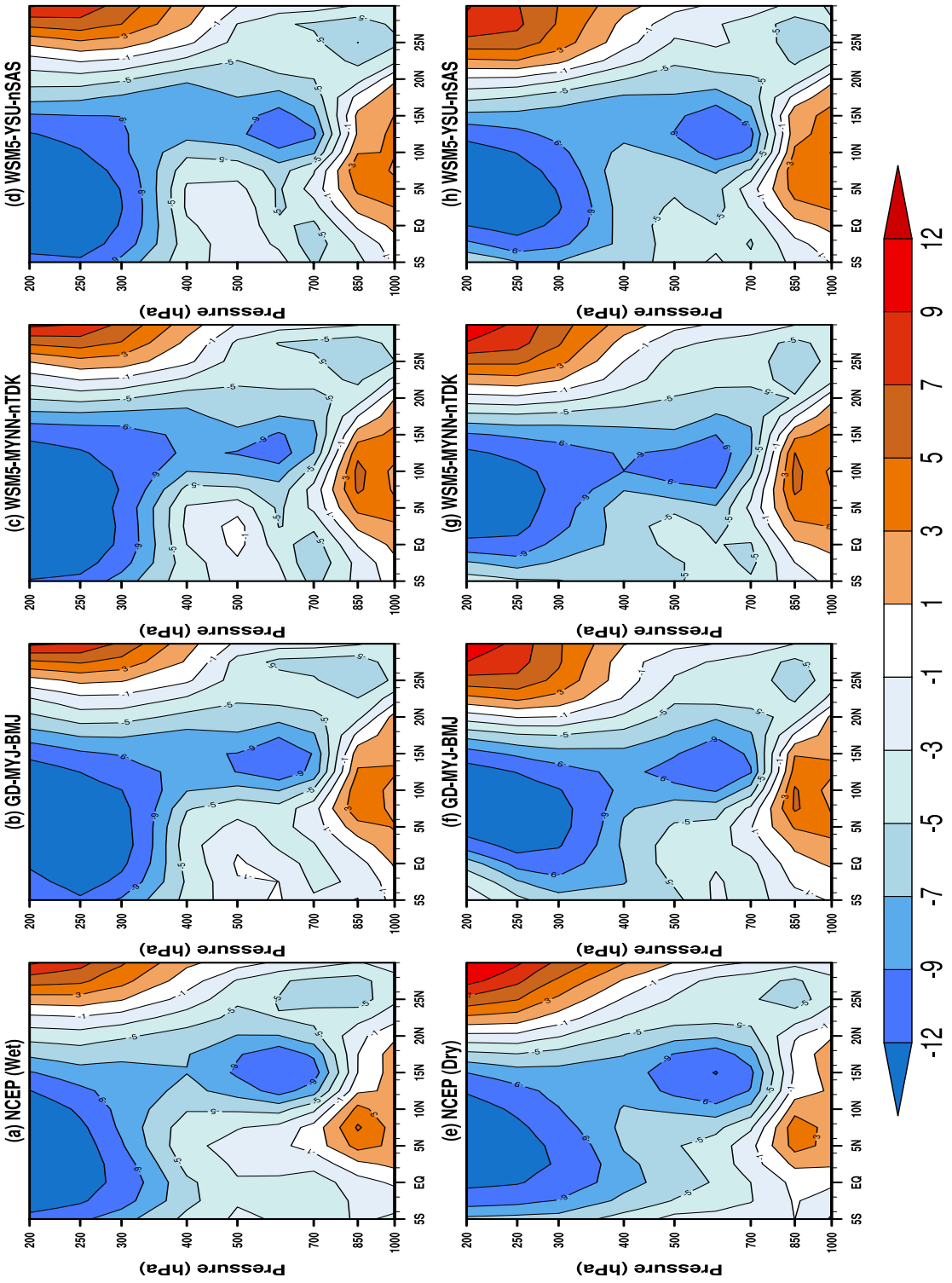

Figure 4.26: Vertical Cross-Section of Zonal Wind (m s^{-1}) Averaged from Longitude 10°W to 10°E for August from NCEP and the Three Experiments for Wet Year (2008 and 2010) (Top Panels) and Dry Year (2001 and 2011) (Bottom Panels) Composites.

Figure 4.27 presents the vertical cross-section of mean vertical motion averaged along longitudes 10^{o}W and 10^{o}E in the month of August. The figure clearly defines the described two regions of vertical ascent (Nicholson, 2009a). The first region of ascent (blue) lies between the mean latitudinal position of AEJ (~15^{o}N) and TEJ (~5^{o}N), while the second shallow region of vertical ascent resides around the surface position of the ITD and center of the Saharan heat low. The vertical ascent shows strong sensitivity to the choice of physics options, most especially the PBL and convection schemes as found in a preliminary study (Gbode et al., 2019). Irrespective of the disparities in the simulated shape and magnitude, two locations of strong ascending motion are reproduced in the wet and dry year simulation when compared with reanalysis. The depth of the major region of ascent extends beyond 200hPa with its core positioned around 10^{o}N. This region is related to convective activity and it corresponds to the latitudinal position of maximum rainfall amount (Nicholson, 2009b).

All simulations are able to reproduce this ascent but with different meridional width. However, the structure of WSM5-YSU-nSAS appears to agree well with the reanalysis. During wet years, when the ascent is strongest, the meridional width broadens and shifts slightly northwards. In a dry year, when the ascent is usually weak, it is narrow with a southward displacement and its core extends to about 300hPa. WSM5-MYNN-nTDK has a shallower southern extension of ascent core, which makes it underestimate rainfall most especially within the zonal band of 5^{o}N to 10^{o}N (see Figure 4.21). While the WSM5-MYNN-nTDK simulation shows underestimation, the WSM5-YSU-nSAS overestimates the rainfall distribution.

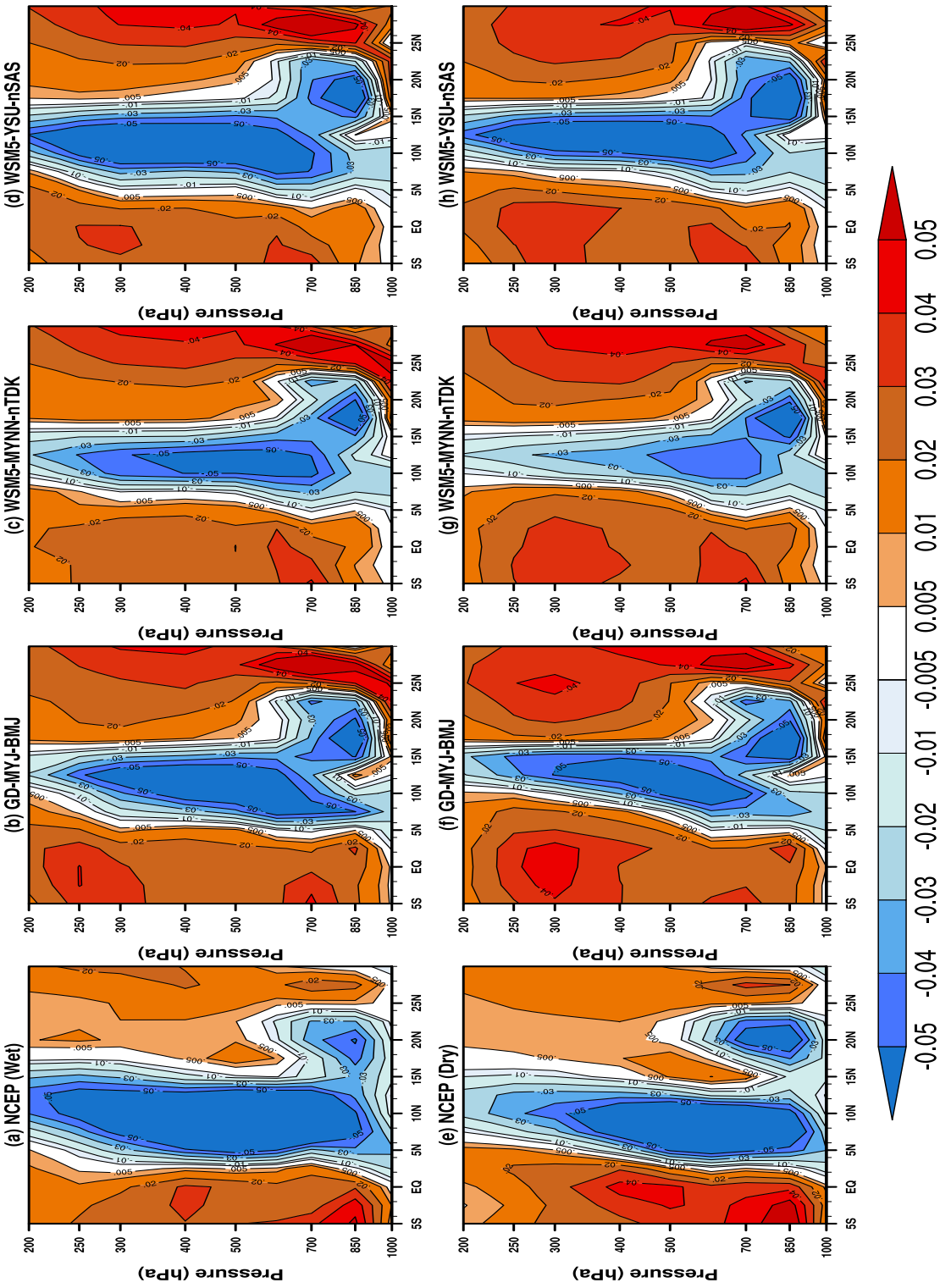

Figure 4.27: Vertical Cross-Section of Omega (Pa s^{-1}) Averaged from Longitude 10°W to 10°E for August from NCEP and the Three Experiments for (a) Wet Year (2008 and 2010) and (b) Dry Year (2001 and 2011) Composites.

The ascending motion is strongest in WSM5-YSU-nSAS, followed by GD-MYJ-BMJ and WSM5-MYNN-nTDK during wet and dry years. Its strength is more in WSM5-YSU-nSAS in the dry years. This result strongly impacts the simulated rainfall amount and distribution, that is, consistent with the overestimated rainfall in WSM5-YSU-nSAS, moderate distribution in GD-MYJ-BMJ and underestimation in WSM5-MYNN-nTDK. This impact is clearly seen over the west coast of the region.

4.4 CHARACTERISTICS OF WAM IN A WARMING CLIMATE

In this section three of the identified WRF model physics combinations is applied to examine the impact of the warming climate on the characteristics of WAM. Pseudo-Global warming approach, which is a dynamic downscaling method that permits regional climate change projections with the use of a regional climate model (Hara et al., 2008; Kimura & Kitoh, 2007; Liu et al., 2017; Rasmussen et al., 2014, 2011; Sato et al., 2007), is employed. The purpose of this study is to assess the possible future changes that could occur in the context of climate change and variability.

4.4.1 Climate Perturbation Analysis

This section presents the climate signals produced from the difference between the two climate periods, that is, current (1976-2005) and future (2071-2100). The climate signals are derived from the RCP8.5 LENS CESMv1-CAMv5.2 GCM output and combined with the 6-hourly reanalysis for model initial and boundary value conditions. As mentioned earlier the perturbed parameters include horizontal wind, temperature, and relative humidity.

Figure 4.28 shows the spatial distribution of the surface air temperature bias derived from the difference between the two climate periods for the month of January through to December. The figure describes how the surface air temperatures vary and evolve between the two climate periods. Generally, the values of temperature changes are positive and range between 1-6^{o}C across most months except for September where the upper limit of change is approximately less than 5^{o}C. Weak temperature gradient exists over the Ocean while steep gradient exists over the entire continent. In January, widespread of high temperature between 4.5-6^{o}C dominates north of latitude 10^{o}N over land. This pattern intensifies in February thereby creating a belt of high temperature changes (i.e. 6^{o}C and above, as shown in Figure 4.28b) within the zone north of 5^{o} to 10^{o}N. In March, the widely spread temperature difference becomes more stratified and significantly weakens (strengthens) over the eastern (western) Sahel region. This evolution progress further from March through to July and August, where a distinct region of maximum warming reside mostly around western Sahel and minimum around the eastern Sahel, which is obvious in August (Figure 4.28). The maxima in the western Sahel weakens in September as minimum values advance in the area from the eastern region. Warming reappears between the latitude bands of 15-20^{o}N in October. This warming intensifies in November where temperature difference of about 6^{o}C dominates most land areas to the north of 15^{o}N. In December, the values reduced slightly and extend southwards of the West African region (Figure 4.28l).

Figure 4.29 presents the spatial distribution of relative humidity change between the two climate periods for the month of January through to December. Expected changes in this parameter range from -10% to 10% across land areas. Over the Ocean, relative

humidity difference as high as 8% or less exist. The evolution of the relative humidity is tightly coupled with the spatial distribution of temperature change found in Figure 4.28, which is expected because the two parameters depend on each other, that is, high temperature will result in low relative humidity and vice versa for the same amount of water vapor in the atmosphere at a fixed pressure level. For example, regions of dryness correspond with a region of intense warming in the western Sahel. In January and February, there exist a zonal positive bias close to the Atlantic coast. Based on relative humidity, the continent appears to be dryer in the future projection from the month of March through to August, during which the WAM appears and dominates the West African region. In March, a region of dry maxima emerges, which becomes well defined in May as it intensifies and progress north approximately from latitude 11^{o}N to 16^{o}N in August. In October, lies a region of wetness centered along 15^{o}N. This positive bias region weakens and advances southwards in November and even further in December.

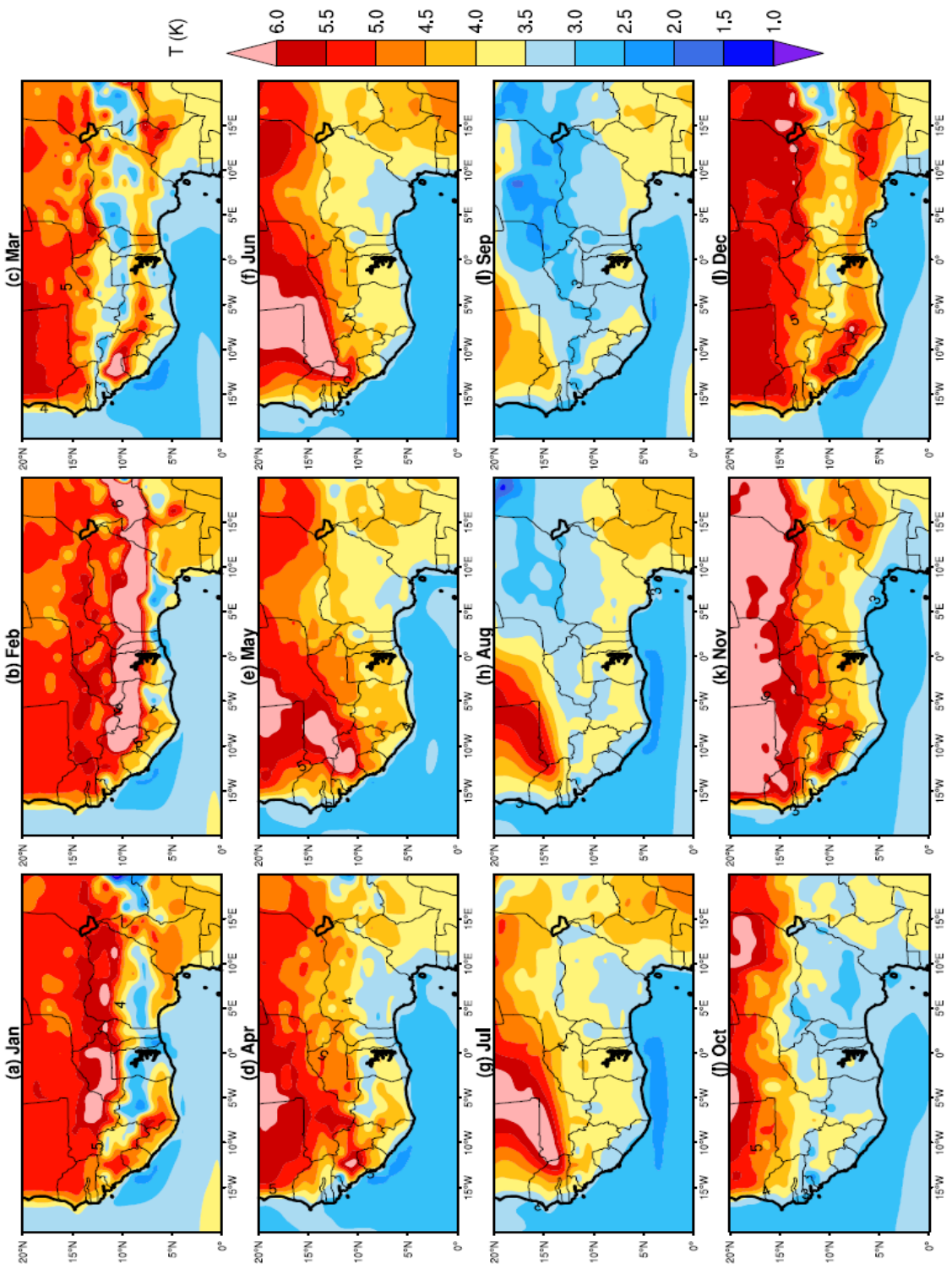

Figure 4.28: Spatial Distribution of Surface Air Temperature Changes Derived from the Difference between the Current (1976-2005) and Future (2071-2100) Climate.

NOTE: The LENS CESMv1-CAMv5.2 40-member ensemble of historical and RCP8.5 was used to produce the climate perturbation.

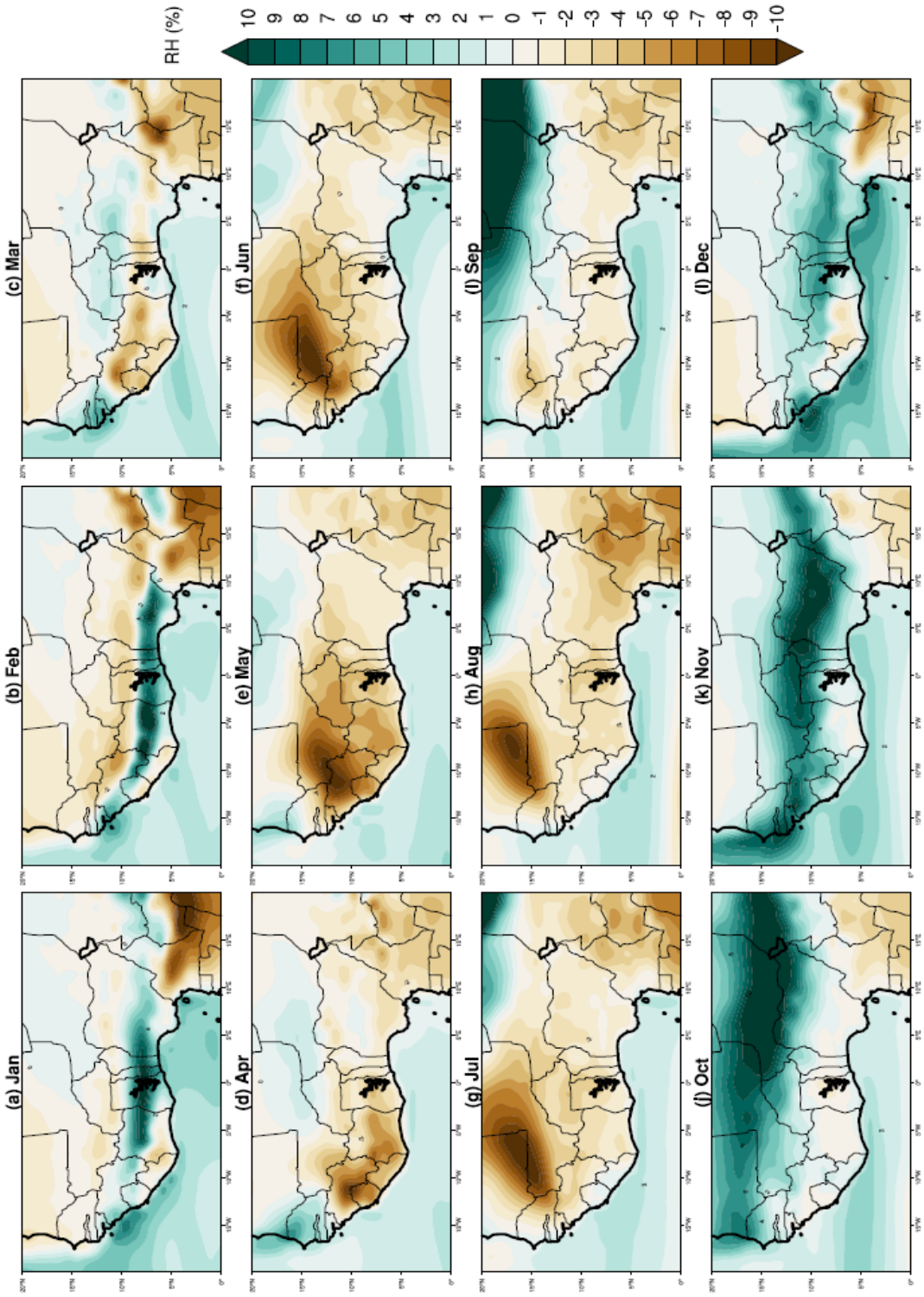

Figure 4.29: Spatial Distribution of Near Surface Relative Humidity Changes Derived from the Difference between the Current (1976-2005) and Future (2071-2100) Climate.

NOTE: The LENS CESMv1-CAMv5.2 40member ensemble of historical and RCP8.5 was used to produce the climate perturbation.

The differences in wind vector and speed (filled contour), temperature (red contour) and relative humidity (blue contour) at 850mb pressure level are presented in Figure 4.30. At this pressure level, northeasterly trade winds usually dominate the months of January to March as well as in October to December while the south easterlies trade winds appear in April and dominate through to September. Wind speed bias of about $1.2ms^{-1}$ exists between the two climates epoch. Away from the monsoon months, that is, January-February and October-December (Figures 4.30 a, b and j-l) the difference are negative mostly over the Ocean and wider land area. Positive wind speed change appears in March through to September, when it becomes enhanced and widely spread over land area. While months order than the WAM months has south westerly wind flow bias consequent to weak north easterlies in the future climate, there exist northwesterly winds to the south of $10^{o}N$ during the monsoon months. As found in Figures 4.28 and 4.29, regions of positive temperature differences coincide with the region of low relative humidity changes. Likewise, areas of positive wind speed biases correspond with warm areas while negative values are associated with positive relative humidity biases.

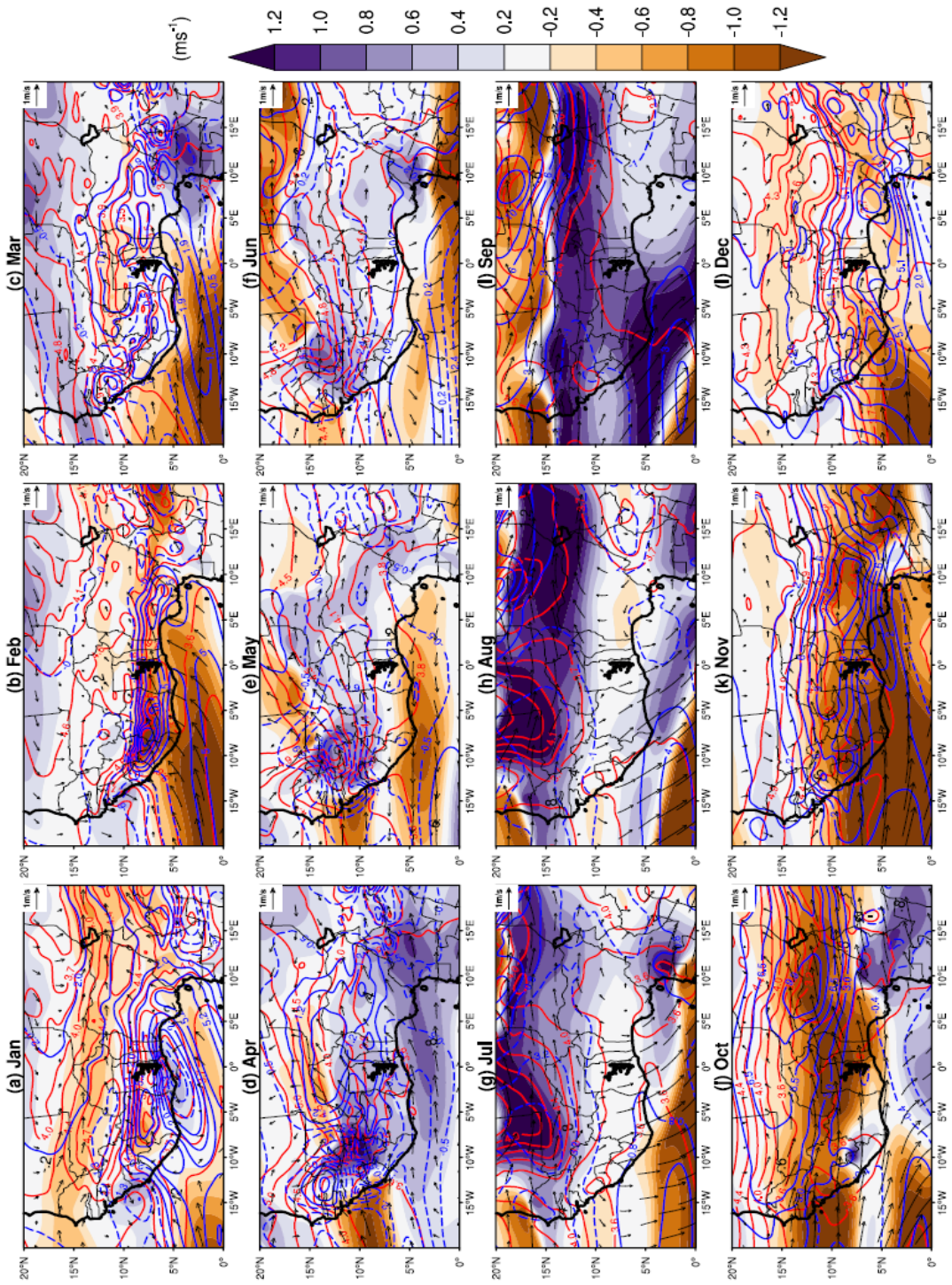

Figure 4.30: Spatial Distribution of Change in Wind Speed, Temperature, Relative Humidity and Wind Flow at 850mb.

NOTE: The changes are derived from the difference between the current (1976-2005) and future (2071-2100) climates. The filled, red and blue contours represent wind speed, temperature and relative humidity, respectively. Wind vector of $1ms^{-1}$ is used as the reference wind change.

At 600mb, where the AEJ resides, the winds are usually easterlies and they intensify as they evolve from January to August, where the AEJ attains its maximum latitudinal position of approximately 16^{o}N, thereafter recedes and weakens in September and beyond. The wind speed bias approximately ranges from -2.5ms^{-1} to 2.5ms^{-1} (Figure 4.31). Also, in the same figure regions of strong moisture and temperature gradients correspond with each other. A clearer coupling is the negative relative humidity difference that corresponds with the region of maximum temperature change in April to August (Figures 4.31 d-h). The wind speed in the future climate appears to be weak relative to the current climate during the months of January to March, mostly over the Sahel in March. Similarly, the winds are also weak in the months of September to December in the future climate. In March, positive wind speed difference begins to surface. This feature further intensifies in April and dominates the entire West African region from May to July. In August, the positive difference weakens and moves further north as the negative values begin to emerge over the Ocean and eastern corner of the region (Figure 4.31h). The negative wind speed difference strengthens and dominates the larger land area in September before becoming less strengthened in the following months. The wind vector at this level are consistent with the easterly flow by producing easterly biases, most especially during the monsoon periods, but westerlies are found around regions with negative wind speed values when the future wind speed is weak.

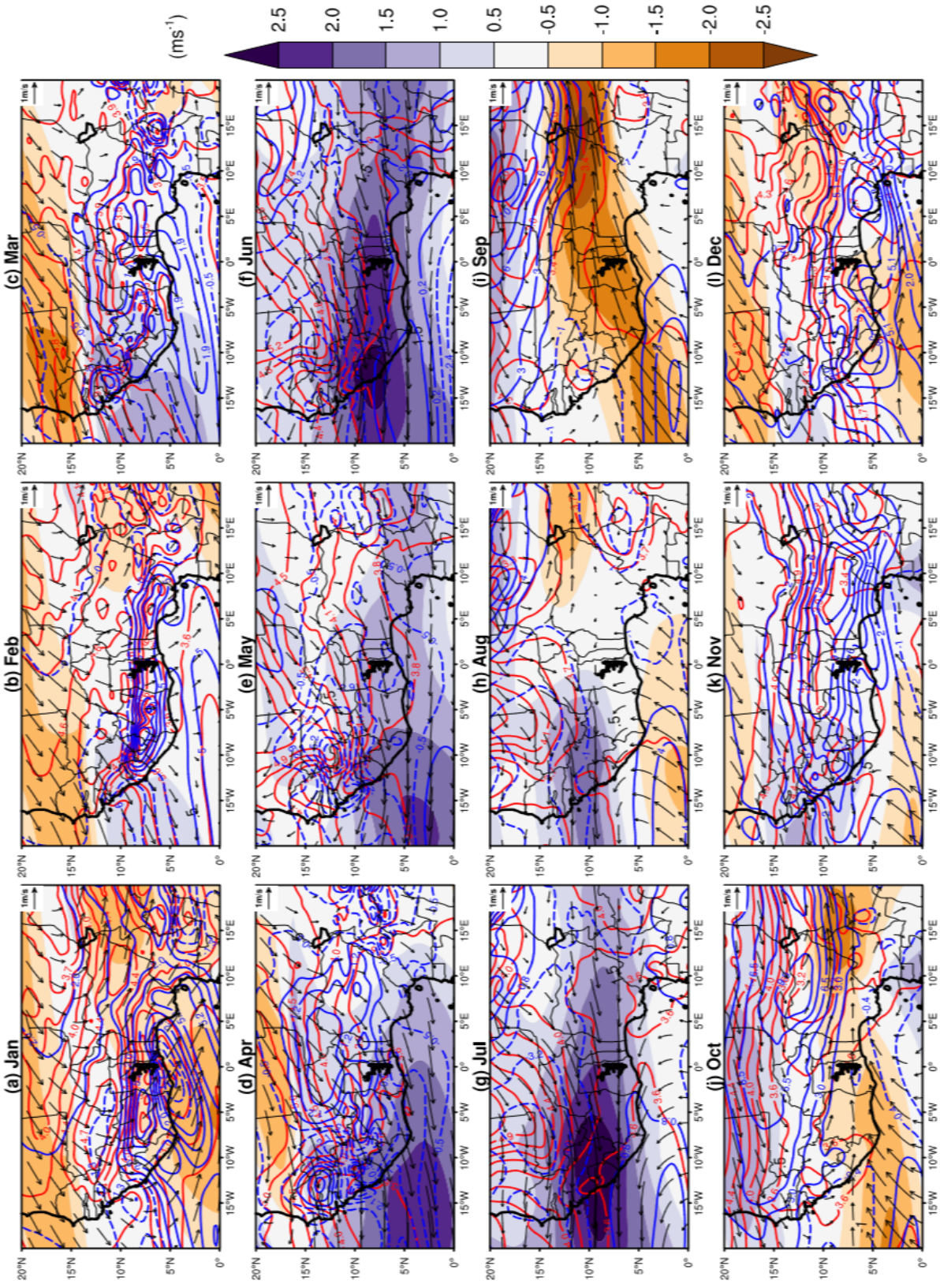

Figure 4.31: Same as Figure 4.30 but for 600mb Pressure Level

Another pressure level critical to the West African climate system is the 150mb where the TEJ dominates. At this upper tropospheric level, the winds are predominantly westerlies in January-March and October-December. In April, the easterlies begin to emerge gradually from the southern coast of the region before becoming prevalent in May through to September. Winds found at this level is stronger compared with that at 600mb. The difference between the current and future climate obtained from the CESM could reach about $10ms^{-1}$ (Figure 4.32). Far north, the wind vector changes are mostly westerlies but easterlies to the south and over areas closer to the coast in January-March. The westerlies intensify in May to June but weaken over land areas in July. In August and September, the easterlies in the future climate appear to be stronger than the current climate. This could possibly result in a stronger TEJ and suppressed AEJ and thus produce more rainfall because of enhanced low-level monsoon flow. Generally, the future climate is warmer than the current climate and the temperature difference can reach 5.2 ^{O}C. Also, the future climate can be dryer in terms of relative humidity compared with the current climate, most especially in the dry season months over Sahel region, however, positive biases reaching 6% can also be found over ocean and land areas across the months.

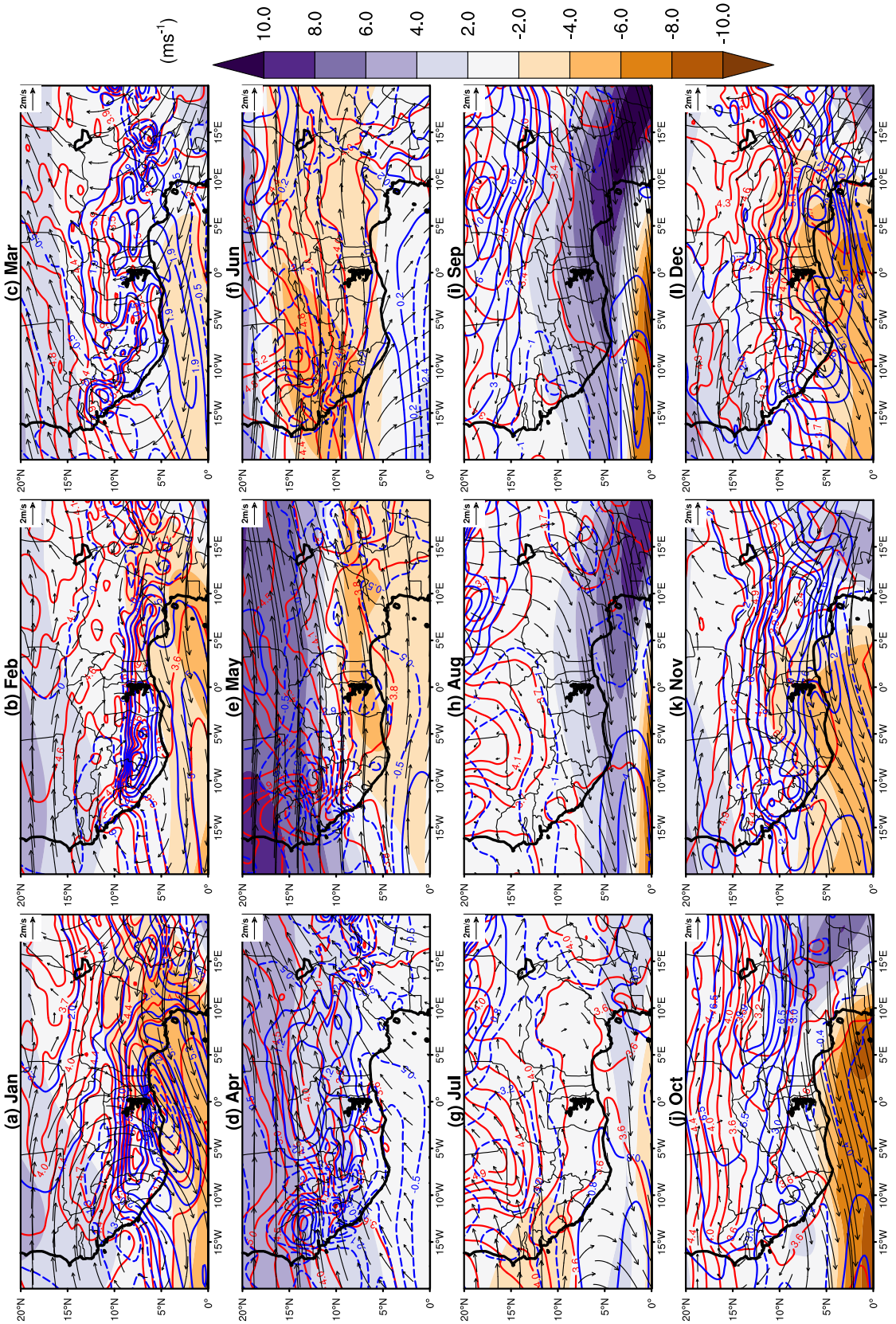

Figure 4.32: Same as Figure 4.30 but for 150mb Pressure Level.

4.4.2 Temperature Characteristics

Figure 4.33 shows the mean surface air temperature averaged during the period JJAS for ERAI reanalysis and model outputs (i.e. present and future runs). In this panel, Figure 4.33a-b shows the current and future runs from CESM, 4.33c depicts ERAI, 4.33d-f show the present climate runs, 4.33g-i show the PGW runs and 4.33j-l depicts the difference between PGW and present climate during JJAS. The boxplot below 4.33c shows the statistics of the 2meter temperature from March to October over the area within latitudes 5-15^{o}N and longitudes 10^{o}W-10^{o}E.

The reanalysis shows observed temperature range between 20-36^{o}C with a strong gradient in the Sahel. This gradient is associated with the Saharan heat low defined by the mean position of the ITD and low-pressure center, mostly in August when the monsoon is fully developed (Nicholson, 2013). Also, surface air temperature over complex orographic terrains is cooler relative to the desert and nearby land areas. During the 20th century (Figure 4.33a), CESM simulates similar distribution as observed but cooler temperatures over complex terrains, mostly over the Cameroun Mountains and Fouta Jallon highlands. In the future runs (Figure 4.33b), the model output is warmer over the complex terrains and even higher temperatures of about 40^{o}C over the Sahel. The present runs of the WRF model (Figure 4.33d-f) also agree with the reanalyzed temperature gradient but with some biases mostly in the Sahara desert region. Simulated air temperature in the PGW runs, generally, shows warming across the entire domain and ocean (4.33g-i). The maximum value exceeds 40^{o}C over the desert area. Relative to the present climate, the PGW runs are 5^{o}C warmer. In GD-MYJ-BMJ8.5 and WSM5-YSU-nSAS8.5 there is uniform warming of 4^{o}C from the coast upward to about 15^{o}N latitude

followed by a northward gradient. Similar warming pattern is found in WSM5-MYNN-nTDK8.5 but restricted only to about 10°N. Over the ocean, the magnitude of warming is lesser perhaps due to its high heat retention capacity.

The box-percentile plot at the bottom left corner of Figure 4.33 shows the distribution of the temperature values during the period of March to October for the area enclosed within latitudes 5°-15°N and longitudes 10°W-10°E. The values of ERAI range between 25°-31°C with the mean being 27.9°C. The distribution of the current climate simulation agrees with ERAI with values ranging from 24°-31.5°C. Relative to the WRF simulations, CESM simulates lower temperatures during the current and future runs. GD-MYJ-BMJ distribution simulates average values closer to that of the ERAI. WSM5-MYNN-nTDK simulates a lower mean of about 0.4°C while the WSM5-YSU-nSAS simulates warming of about 0.6°C relative to ERAI. Results of the PGW runs show a wider range of temperature (28°-36°C) and a significant shift in the mean. The average difference in the mean between the PGW and current is approximately 4°C. The warming is generally found in all three simulations. Though the WSM5-YSU-nSAS8.5 shows higher mean and range, the difference in mean between the current climate remains at 4°C. This could explain the higher values of precipitation amount found in the combination (Table 4.7 and Figure 4.35) as the increasing temperature will favor surface evaporation, which in turn will enhance convective activity. The temperature range of WSM5-MYNN-nTDK8.5 is smaller compared with that of GD-MYJ-BMJ8.5 but the two combinations have almost the same mean value.

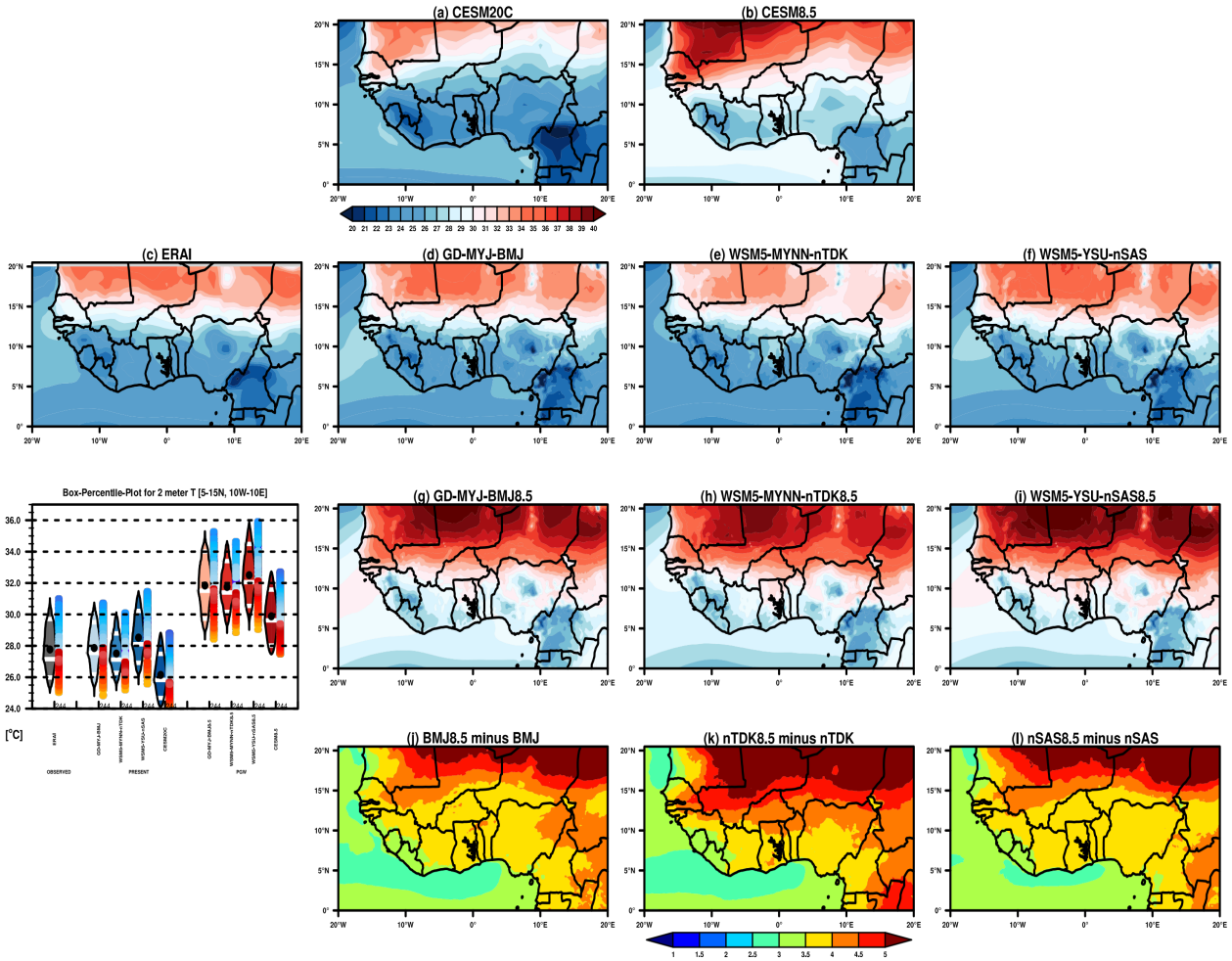

Figure 4.33: Average Surface Air Temperature during the Period JJAS for ERAI Reanalysis and Model Outputs (i.e. Present and Future Runs).

NOTE: Panels 4.33a-b shows the current (20th Century) and future (2071-2100) runs from CESM, 4.33c depicts ERAI, 4.33d-f show the present climate runs, 4.33g-i shows the PGW runs and 4.33j-l depicts the difference between PGW and present climate during JJAS. The boxplot below 4.33c shows the statistics of the 2meter temperature from March to October over the area within latitudes 5-15°N and longitudes 10°W-10°E. Values in the WRF model plots are averages derived from the selected five years (i.e. 2001, 2007, 2008, 2010 and 2011).

Further analysis of the probability distribution shows that the surface air temperature averaged over 0-20^{o}N and 20^{o}W-20^{o}E vary from about 24^{o}C - 31^{o}C and 27^{o}C – 35.3^{o}C for the current and future climate, respectively, with two density maxima (Figure 4.34). These density maxima could be associated with pre-monsoon, when the temperatures are usually high as a result of clear sky conditions that allow more insolation to reach the surface, and post-monsoon periods, when the temperatures are usually low as a results of frequent convective activities that bring about cloudy conditions which prevents incoming radiation from reaching the surface. The observed density (grey line, i.e. ERAI) corresponding to the low (high) temperature maxima is higher (lower). CEMS simulates lower temperatures compared with ERAI and WRF current and PGW runs. The three model experiments also reproduced the observed distribution with varying density. For example, the density of low temperature values in WSM5-MYNN-nTDK is higher compared with that of GD-MYJ-BMJ and WSM5-YSU-nSAS. During the last climate regime of the 21st Century (2071-2100), both GCM and RCMs simulate a significant increase in temperature. Temperatures in the WRF runs are expected to increase more compared with the GCM. The upper bound shift in temperature could reach 3^{o}-4^{o}C.

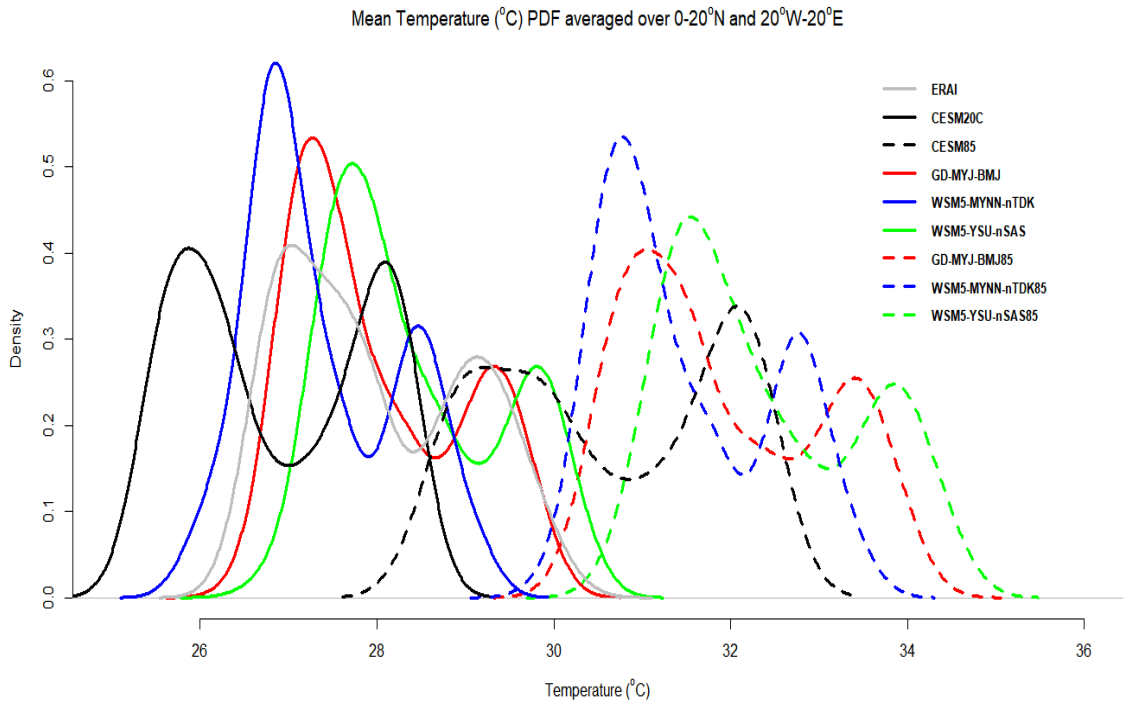

Figure 4.34: Probability Density Function of Observed and Simulated Daily Mean Temperature Averaged over the 0-20°N and 20°W-20°E Domain.

NOTE: ERAI and WRF outputs are derived from the average of the selected five years while CESM20C and CESM85 are derived for the period 1976-2005 and 2071-2100, respectively.

4.4.3 Precipitation Characteristics

The observed average daily precipitation amount and the modeled values for present and future simulations during the period JJAS is presented in Figure 4.35. Also, the bottom boxplot plot of Figure 4.35 shows the statistics of the daily precipitation distribution from March to October over the area of latitudes 5-15N and longitudes 10W-10E. GPCP and TRMM (in Figure 4.35a and b) show average daily rainfall values reaching 14mm day^{-1} and 16mm day^{-1}, respectively. Both observation products agree in terms of producing maximum values over complex orographic terrains and minimum in other land areas. CESM simulates values of 16mm day^{-1} in the 20^{th} Century and RCP8.5 (Figure 4.35c and d) in agreement with TRMM but the GCM however show deficiencies in reproducing the observed maximum over the complex terrains of Jos Plateau and the southeast orientation pattern over the Cameroun Mountains, this points out the limitations of the GCM to reproduce certain features due to its coarse horizontal resolution that makes it difficult to properly capture atmospheric phenomena at smaller horizontal scales than its grid.

Consistent in observations and WRF simulations is the band of maximum daily average rainfall sitting, on average, along latitude 10^{o}N. Also, the RCM runs agree with observations as they simulate the climatological precipitation maxima over complex orographic terrains of Cameroun Mountains, Jos Plateau, and Fouta Djallon highlands with extension towards the western coast of West Africa. In the present year simulations, GD-MYJ-BMJ also reproduces the magnitude of 16mm day^{-1} over the Cameroun Mountain and the western coast of the monsoon region (Figure 4.35e). For WSM5-MYNN-nTDK and WSM5-YSU-nSAS (Figure 4.35i and m) runs the simulated

magnitude could be 15mm day^{-1} or less. The PGW runs shows an increase in daily precipitation relative to the present climate runs, most especially over complex orographic terrains and over the west coast of West Africa. While the simulated values of GD-MYJ-BMJ8.5 and WSM5-YSU-nSAS8.5 could be greater than 17mm day^{-1}, that of WSM5-MYNN-nTDK8.5 only simulates maximum of 15mm day^{-1} (Figure 4.35f, j, and n).

Although the models agree with the observation patterns, there exist some systematic errors. The degree of these errors is quantitatively assessed, firstly, by taking the difference between current runs and GPCP (Figure 4.35g, k, and o). The results show wetness of about 5mm day^{-1} over complex terrain and other land areas. In contrast, dryness (less than -5mm day^{-1}) is simulated over the western Sahel and along the southern coast of the monsoon region as well as ocean areas. Secondly, by computing the difference between PGW and current climate runs which shows general wetness of less than 4mm day^{-1} around the western part of the region and small extent of 2mm day^{-1} drying in other land areas (Figure 4.35h, l, and p). Further, to examine the effect of warming on precipitation the statistics of observations and model results are presented in the bottom of Figure 4.35 (Boxplot). Results show that the maximum observed and modeled daily precipitation in the considered area (5^{o}-15^{o}N and 10^{o}W-10^{o}E) is about 11mm day^{-1} and 12mm day^{-1} for PGW runs. In CESM the values are less than 8mm day^{-1}. The mean value for GPCP and TRMM is slightly above 4mm day^{-1}. For the current climate runs, GD-MYJ-BMJ agrees with the observed mean values while WSM5-MYNN-nTDK simulates exactly 4mmday^{-1}. WSM5-YSU-nSAS produces higher magnitudes of daily precipitation and an increase in the mean (i.e. 5 mm day^{-1}). The

impact of warming is evident through the increase in the mean and maximum value of PGW runs. This response is most obvious in GD-MYJ-BMJ8.5 and WSM5-YSU-nSAS8.5, where there is a slight increase of the mean (~0.2mm day^{-1}) and maximum (>12mm day^{-1}). In WSM5-MYNN-nTDK, there is an increase in the maximum daily precipitation values but no significant change in the mean distribution.

Table 4.7 shows the total amount of rainfall received from GPCP and TRMM, and WRF model for each climatic zone during the month of March through to October. Results show that the wet and dry year is consistent in GD-MYJ-BMJ for both current and PGW simulations in all the three climatic zones (Guinea Coast, Savannah, and Sahel) outlined in Figure 3.1. The monsoon characteristics of WSM5-MYNN-nTDK for the simulated years is well defined only in Savannah and Sahel in both periods but not distinctly defined in WSM5-YSU-nSAS runs. Further, WSM5-YSU-nSAS simulated higher values compared with the other two experiments.

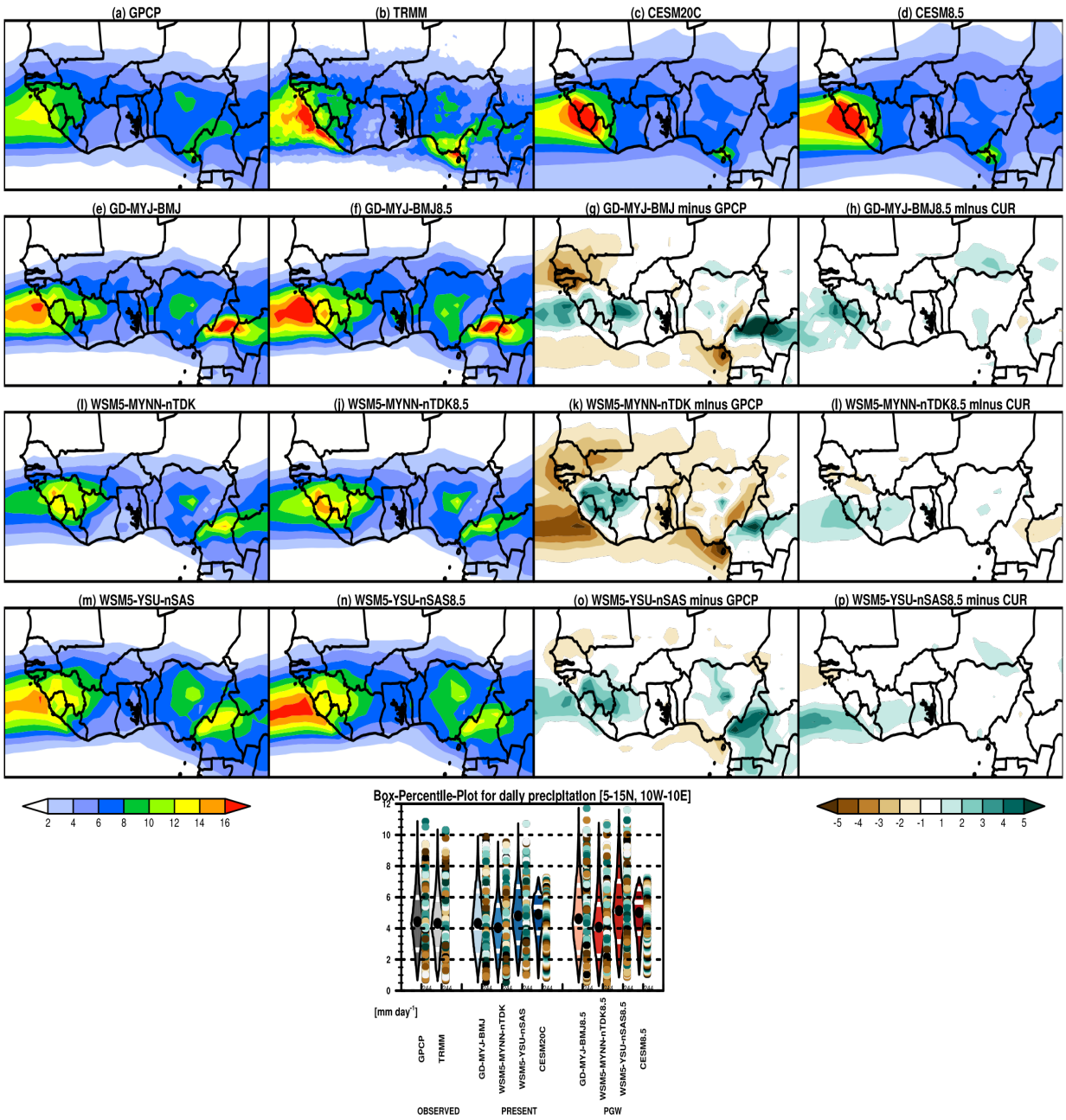

Figure 4.35: Spatial Distribution of Average Daily Rainfall (mm day^{-1}) for the Period JJAS.

NOTE: Values of (a) GPCP, (b) TRMM and (e, f, I, j, m and m) WRF runs are derived from the average of the five simulated years while the ((c and d) CESM values are derived from the considered 30years current and future periods. Differences between (g, k and o) GPCP and WRF current and (h, l and p) PGW and current runs are also presented in the figure. The bottom boxplot shows the statistics of the daily precipitation distribution from March to October over the area of latitudes 5-15N and longitudes 10W-10E.

Table 4.7: Total Rainfall Amount (mm) from GPCP and TRMM, and Current and PGW WRF Model for each Climatic Zone from March through to October.

		GPCP	TRMM	BMJ	nTDK	nSAS	BMJ8.5	nTDK8.5	nSAS8.5
Monsoon	**Year**	**Guinea Coast (4-8^{o}N)**							
Dry	2001	1291	1423	1069	1107	1326	1100	1119	1370
	2011	1154	1311	1109	1132	1385	1079	1052	1471
Wet	2008	**1422**	**1607**	**1137**	**1202**	**1436**	**1186**	**1204**	**1566**
	2010	**1367**	**1592**	**1174**	1076	1341	**1179**	1109	**1484**
Normal	2007	1428	1520	1206	1272	1433	1304	1263	1557
		Savannah (8-11^{o}N)							
Dry	2001	1156	1121	1254	1135	1367	1189	1212	1466
	2011	1050	1015	1224	1183	1325	1301	1142	1448
Wet	2008	**1330**	**1260**	**1360**	**1281**	**1405**	**1417**	**1310**	1460
	2010	**1277**	**1185**	**1336**	**1251**	**1461**	**1438**	**1399**	**1521**
Normal	2007	1287	1212	1340	1217	1357	1363	1232	1428
		Sahel (11-15^{o}N)							
Dry	2001	672	603	652	461	723	782	490	758
	2011	588	558	621	450	616	727	420	684
Wet	2008	**765**	**708**	**703**	**596**	671	**789**	**590**	**779**
	2010	**774**	**730**	**752**	**605**	**791**	**860**	**583**	**830**
Normal	2007	719	624	692	557	742	810	541	810

The result in Table 4.7 further underscores the role of surface air temperature on rainfall amount associated with West African monsoon activity. Further statistics (see Table 4.8) shows that the precipitation changes between GPCP and current runs are averagely found to be -5, 0.6 and -50% in the Guinea Coast, Savannah, and Sahel, respectively. Also, differences between TRMM and current runs may reach maximum values of -19, -7 and -52% for the corresponding climatic zones. Some of the models underestimate the observed average daily rainfall, mostly in TRMM. Between the current and PGW runs, the average percentage difference is generally small and range between -2 to 16% over the entire monsoon region. In general, the average percentage difference is greater mostly in the Sahel. This suggests possibilities of greater impact on rainfall in the Sahel as a result of global warming. Relative to the Sahel, a less impact is felt in the Guinea Coast, where there are heterogeneous surfaces and features, and a mild influence in Savannah.

The probability distribution analysis of average daily rainfall amount reveals varying densities over the 5-15^{o}N latitudes and 10^{o}W-10^{o}E longitudes (as shown in Figure 4.36). The rainfall distribution between GPCP and TRMM are similar with little differences. Both the current and future climate runs of CESM possess a high density of rainfall of about 6mm day^{-1}. Also, slight rainfall increase of greater than 6mm day^{-1} is simulated in CESM future runs relative to the current runs. Whereas values of less than 6mm day^{-1}, however, occur more in the GCM's current runs. The distribution in the WRF simulations is similar to that of the observations. Generally, the WRF model simulates occurrences of increased heavy and light rainfall in the PGW runs. Also, the PGW run simulates decreased occurrences of moderate rains.

Table 4.8: Average Percentage Difference (%) of Total Rainfall Amount Observed and Modeled during the Period March to October for the 5 Years over each Climatic Zone. GPCP and TRMM (Upper Row) are Subtracted from the Current Model Runs (Lower Rows) to Compute the Percentage Difference. In the same Manner, the Current Runs are Subtracted from the PGW Runs.

Climatic zone	GPCP			TRMM			PRESENT		
	BMJ	**nTDK**	**nSAS**	**BMJ**	**nTDK**	**nSAS**	**BMJ8.5**	**nTDK8.5**	**nSAS8.5**
Guinea Coast	-12	-10	7	-3	-18	-19	3	-1	8
Savannah	1	-6	7	-3	-6	-12	3	4	6
Sahel	-47	-59	-45	-50	-44	-63	16	-2	9

WSM5-YSU-nSAS PGW runs simulates higher average daily rainfall intensity relative to WSM5-MYNN-nTDK and GD-MYJ-BMJ, respectively. This combination, however, simulates lower densities of moderate average daily rainfall.

To further investigate the characteristics of daily rainfall over the region, the rainfall is disintegrated into different categories; light (1-2mm day-1), moderate (>2-10mm day^{-1}) and heavy (>10mm day-1), based on the probability density function presented in Figure 4.36. Figure 4.37 shows the total rainfall and percentage contribution derived from light rainfall intensity, that is, rainfall between 1-2mm, for the period March to October. Observed and simulated total rainfall in this category could reach 200mm. GPCP and TRMM (Figures 4.37a and b) show that daily rainfall within this range provides 9.1% and 8.4% of rainfall, respectively, over the entire monsoon domain. Most of the rains in this category are received within 10^{o}W – 10^{o}E longitudes and extends to 15^{o}N latitude as well as along the southern coast of the Atlantic Ocean. Also, the rains are observed to spread over complex terrains like the Cameroun Mountains, mostly in TRMM. The WRF simulations (Figures 4.37c-h) also agree with the observed spatial pattern and provide a percentage of rainfall within the range of 7.7 - 8.7%. Though Figure 4.36 shows that the rainfall in this category slightly increases, the percentage is expected to decrease by 0.8-1% in GD-MYJ-BMJ and WSM5-YSU-nSAS while no change is found in WSM5-MYNN-nTDK. The total amount of rainfall in the range 1-2mm simulated by CESM (Figures 4.37i and j) provides more widely spread spatial pattern along the Sahel and the southern coast of the Atlantic. Similar to the WRF runs, the GCM simulates percentage decrease of 0.8% and no contribution of this type of rainfall for some areas along Guinea coast.

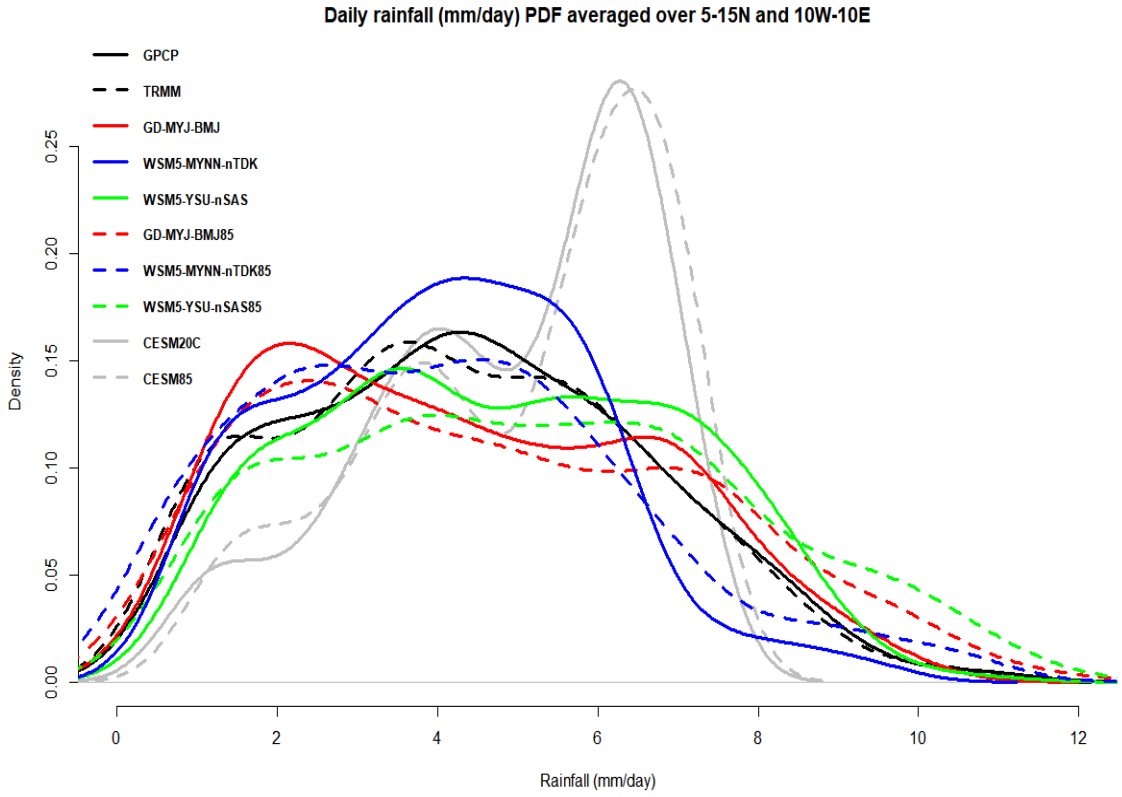

Figure 4.36: Probability Density Function of Observed and Simulated Daily Mean Rainfall Averaged over the 5-15^{o}N and 10^{o}W-10^{o}E Domain.

NOTE: GPCP, TRMM and WRF outputs are derived from the average of the selected five years while CESM20C and CESM85 are derived for the period 1976-2005 and 2071-2100, respectively.

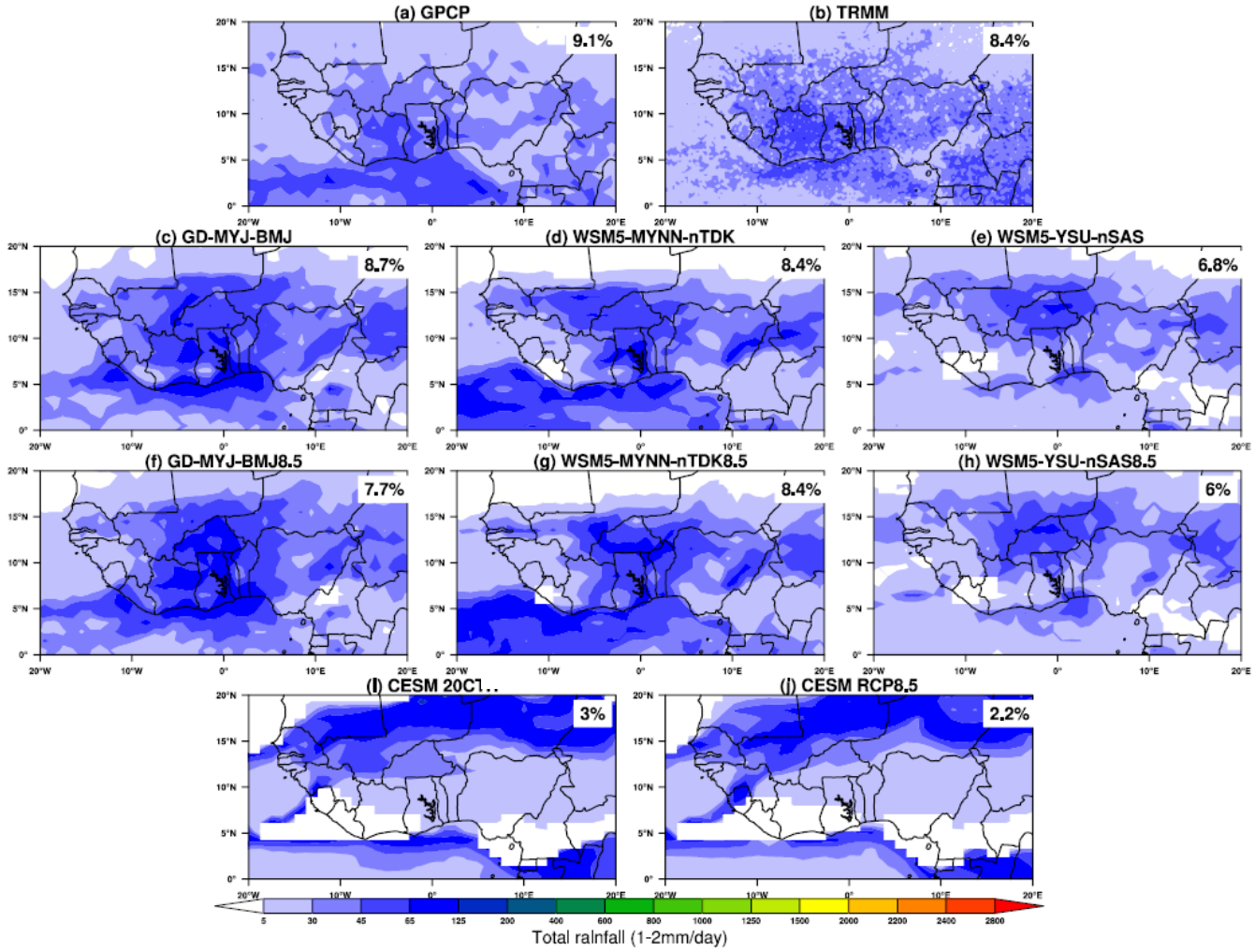

Figure 4.37: Total Rainfall and Percentage Contribution from Light Rainfall (1-2 mm) Intensity Received for the Period March-October.

NOTE: GPCP, TRMM and WRF outputs are derived from the average of the selected five years while CESM20C and CESM85 are derived for the period 1976-2005 and 2071-2100, respectively.

Rainfall within 2-10mm provides the most wide area spread values that are observed to reach 1250mm in the monsoon region. This rainfall category provides 71.7% and 51.6% of rainfall in GPCP and TRMM (Figures 4.38a and b), respectively. WRF PGW runs (Figures 4.38f-g) shows not only a decrease in the frequency of rains in this category but also a decrease in the percentage (i.e. 3-6%). Also, the rainfall amount can possibly reach 1500mm. CESM (Figures 4.38i and j) simulates a percentage decrease of 6.5% in the future runs and this type of rains provides virtually all the rainfall over most parts of the Guinea Coast.

Figure 4.39 depicts the total amount and percentage of heavy rainfall received in the monsoon domain. Heavy rainfall (i.e. 10mm and above) contributes 19.1% and 40% of rainfall is observed in GPCP and TRMM (Figure 4.39a and b), respectively. The values of this type of rainfall can reach 2500mm and are mostly produced over complex terrains, especially over Cameroun Mountains and west coast of West Africa. Other areas of the region also receive rainfall from this category but at a far lesser amount. WRF runs (Figures 4.39c-h) also agree with observations, mostly over the complex topographic terrains. In the PGW runs, the percentage of this type of rainfall is expected to increase by 3-6.5%. For CESM (Figures 4.39i and j), the percentage of 42.2% and 49.4% is simulated in the current and future climate, respectively. The GCM simulates this feature only in the complex terrain of Cameroun Mountains and west coast of the monsoon region.

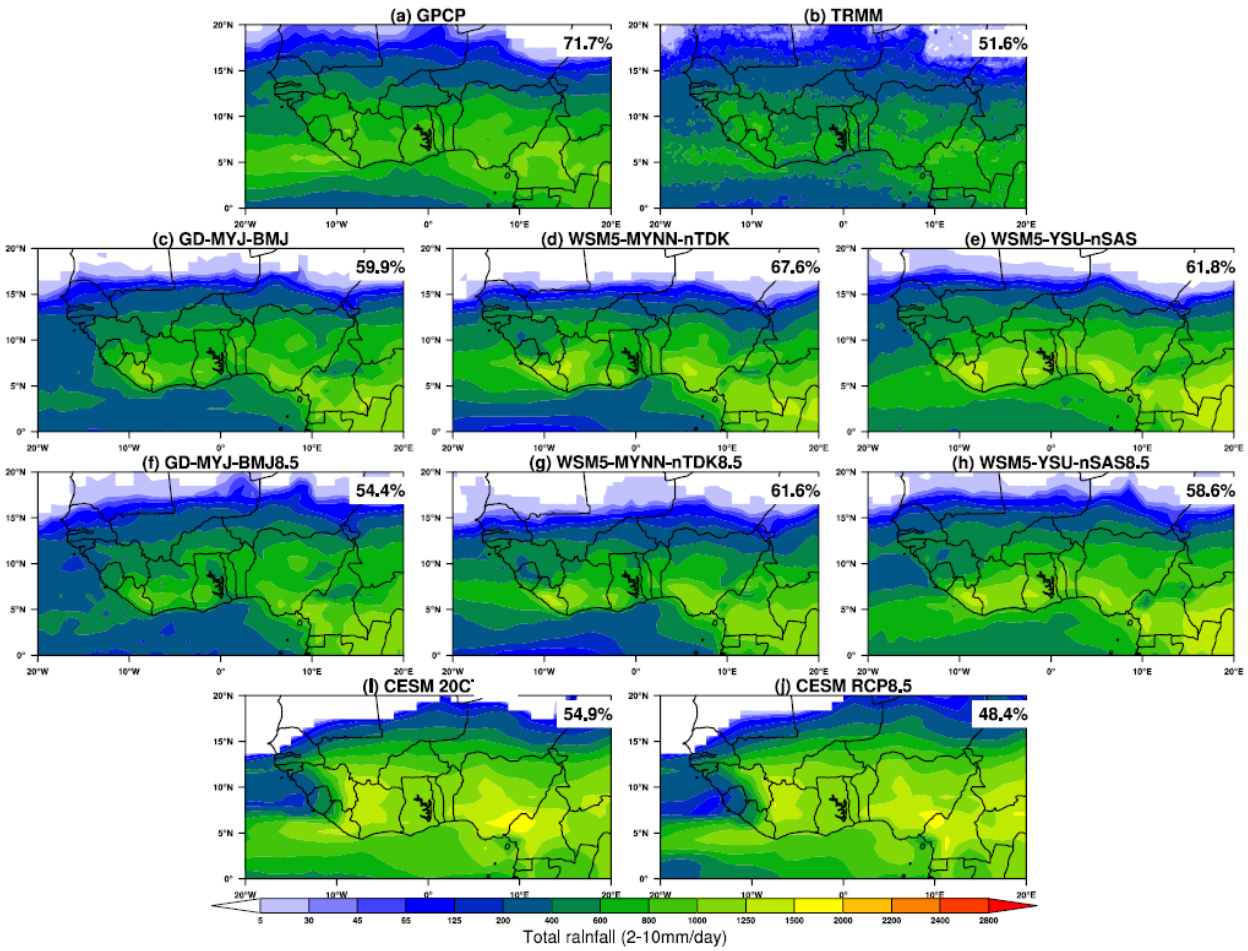

Figure 4.38: Total Rainfall and Percentage Contribution from Moderate Rainfall (>2-10mm) Intensity Received for the Period March-October.

NOTE: GPCP, TRMM and WRF outputs are derived from the average of the selected five years while CESM20C and CESM85 are derived for the period 1976-2005 and 2071-2100, respectively.

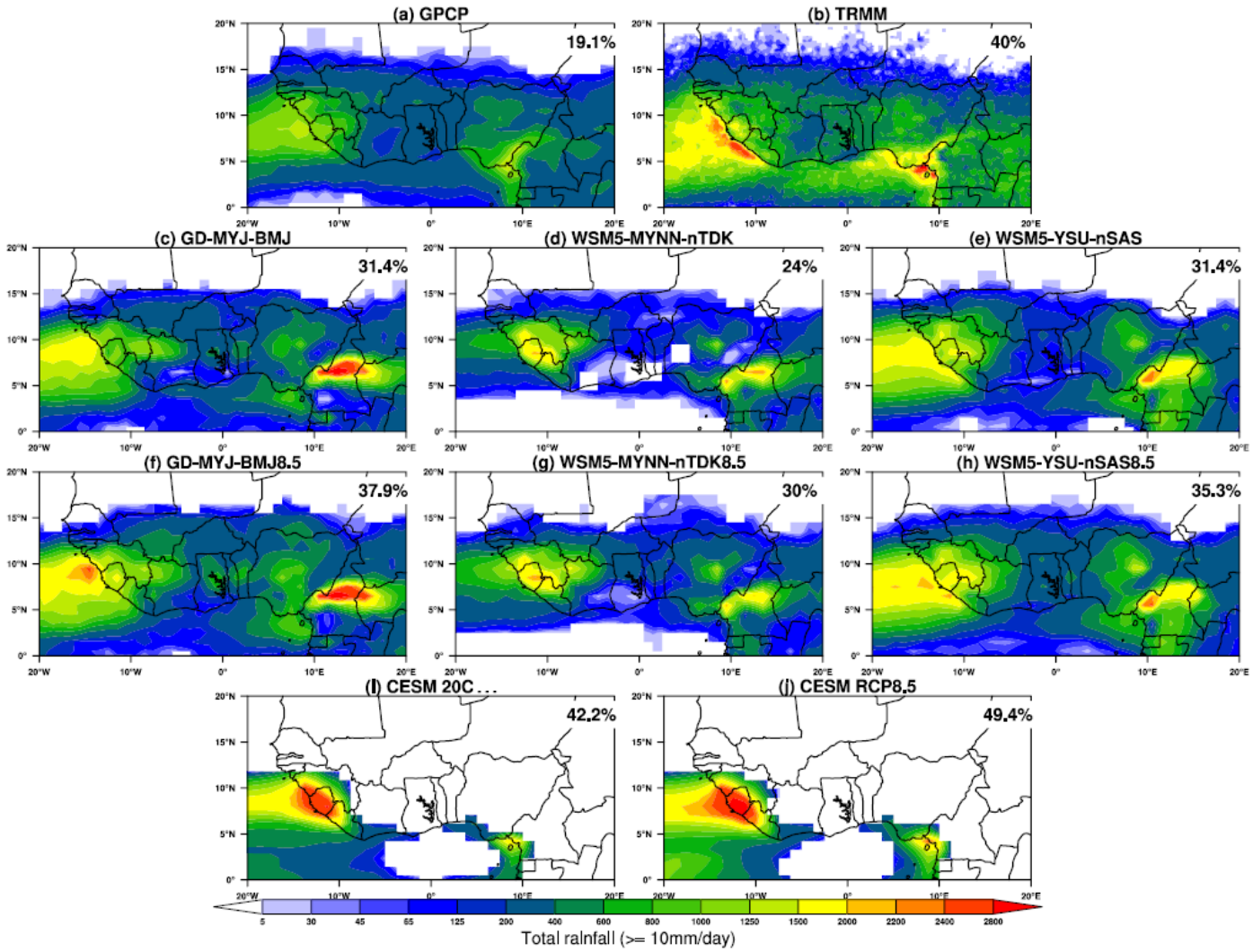

Figure 4.39: Total Rainfall and Percentage Contribution from Heavy Rainfall (10 mm and Above) Intensity Received for the Period March-October.

NOTE: GPCP, TRMM and WRF outputs are derived from the average of the selected five years while CESM20C and CESM85 are derived for the period 1976-2005 and 2071-2100, respectively.

Furthermore, the model's total rainfall is disintegrated in order to quantify the contribution of cumulus (CU) and microphysics (MP) physics (shown in Table 4.9). As stated earlier, the CU schemes are responsible for the convective rainfall while the MP schemes produce the non-convective rainfall. This analysis is performed to investigate the influence of these schemes in each of the three configurations over the three climatic zones and monsoon region. GD-MYJ-BMJ combination reproduces approximately 0.60 and 0.40 fraction of convective and non-convective rainfall, respectively. In the Guinea coast, the fraction of convective rainfall is as high as 0.75. In WSM5-MYNN-nTDK and WSM5-YSU-nSAS, convective rainfall dominates the non-convective rainfall combination by the ratio of approximately 0.93 to 0.07. The results suggest that the role of mass flux convection schemes, nTDK and nSAS, dominates that of the WSM5 microphysics schemes. Both CU and MP schemes provide a considerable amount of rainfall in the GD-MYJ-BMJ and thus, suggesting that the profile adjustment BMJ scheme simulates less rainfall compared with mass flux schemes but however reproduce realistic rainfall.

Table 4.9: Fraction of Convective and Non-Convective Rainfall Produced from the Model Runs. The Domains Considered are West Africa (0-20°N and 20°W-20°E), Guinea Coast (4-8°N and 10°W-10°E), Savannah (8-11°N and 10°W-10°E) and Sahel (11-16°N and 10°W-10°E).

Domain	GD-MYJ-BMJ		WSM5-MYNN-nTDK		WSM5-YSU-nSAS	
	Convective	Non-convective	Convective	Non-convective	Convective	Non-convective
West Africa	0.64	0.36	0.96	0.04	0.93	0.07
Guinea Coast	0.75	0.25	0.98	0.02	0.96	0.04
Savannah	0.54	0.46	0.95	0.05	0.93	0.07
Sahel	0.57	0.43	0.94	0.06	0.85	0.15
	GD-MYJ-BMJ8.5		**WSM5-MYNN-nTDK8.5**		**WSM5-YSU-nSAS8.5**	
West Africa	0.61	0.39	0.95	0.05	0.93	0.07
Guinea Coast	0.72	0.28	0.97	0.03	0.96	0.04
Savannah	0.53	0.47	0.93	0.07	0.93	0.07
Sahel	0.56	0.44	0.88	0.12	0.83	0.17

The results of this study are however contingent on the GCM, which provides the boundary conditions of the RCM. Most especially, the temperature change of the GCM will rather be sensitive to the change in precipitation amount. CESM1.0-CAM5.2, the GCM employed in this study, tends to provide a greater temperature change of about 4^{o}C from the 40-member ensemble of the Large Ensemble Community (LENS) project. This increase consequently leads to an increase in the simulated precipitation in the PGW experiments as it intensifies evaporation that enhances convective activities. The projection of the precipitation is, however, limited to the average of the selected 5years and the RCP used. Also, the role of air temperature on precipitation activity may change for different range of RCPs. Although the PGW method used in the study further reduces large scale model bias and allows the estimate of climate difference between current and future climate without an ensemble of numerous numbers of simulations, it doesn't account for extreme events. Hence, the need for longer-term simulations in future studies.

CHAPTER FIVE

CONCLUSION AND RECOMMENDATIONS

5.1 CONCLUSION

This research successfully evaluates the Weather Research and Forecasting model physics in simulating the West African monsoon. The specific objectives achieved in the research include assessment of the sensitivity of West African Monsoon (WAM) regimes to three model physics (i.e. Cumulus (CU), Microphysics (MP) and Planetary Boundary Layer (PBL) parameterization schemes); evaluation of the performance of the model in representing the WAM dynamics in comparison to observed data and; application of the identified best performing model physics combination to assess the impact of warming climate on WAM under the business-as-usual representative concentration pathway (RCP8.5).

5.1.1 Sensitivity Study

A total of 27 WRF simulations of the August-September 2007 monsoon regime, run on a 20-km grid over West Africa, were evaluated to investigate the sensitivity of the WAM regime using the three model physics. The focus was on hourly and daily precipitation and surface temperature at 2 meters during a period of widely spread convective activity over the West African region. The 27 WRF runs were derived from the combinations of two (2) MP, six (6) CU and three (3) PBL schemes, three of which was done in the latest WRF version 3.9 to test the advantage of the improved nGF CU over the old one in WRF version 3.8.1. The model's precipitation was evaluated against the TRMM (reference), CMORPH and GPCP SRPs. Also, the surface temperature was

evaluated against the ERAI (reference), NCEP, MERRA and GSAT, which is an ensemble of the three corresponding reanalysis products.

All model physics combinations simulated the diurnal cycles of surface temperature more adequately than precipitation, however with some biases. Some combinations simulated realistic westward propagation of precipitation maxima associated with the AEWs. Correlations found in surface temperature are higher than for precipitation, which depicts that the simulations have higher skills in simulating temperature as may be expected because of the variation of surface characteristics over the area. This also suggests that any form of evaluation is subjective and varies with respect to the variable of interest. Based on the overall MSS the best performing physics combinations in both surface temperature and precipitation for the period of study are WSM5-MYNN-nTDK and GD-MYJ-BMJ. However, the good combinations are rather clustered in the overall skill scores and any combinations highlighted in green in Figure 4.12 should be considered not significantly different within the error margins and equally adequate for use to investigate the seasonal, annual and decadal variability of WAM as well as its future (climate) outlook.

5.1.2 Simulation of Normal Monsoon Year

In this aspect of the research, WRF model physics was employed to assess the role of parameterizations on the West African monsoon (WAM) for the 2007 rainy season. Both ERA-Interim and NCEP Final reanalysis were used to drive the model and focus was on parameterization schemes that affect the heat, momentum and moisture distribution. Two different schemes from the MP and three from CU, and PBL

parameterization schemes are combined to produce three physics combination suites. Although the model results contain some uncertainties associated with parameterizations used, they, however, provided useful information on the response of the WAM system to multi-scale dynamic features and to physically resolved sub-grid scale processes. The ability of the three physics treatments to simulate WAM precipitation and its associated dynamical features was analyzed.

The differences among selected physics combinations demonstrate the ability of the WRF model to reproduce the characteristics of the region's monsoon. Thus, the simulation of WAM dynamics such as monsoon flow, African Easterly Jet, and Tropical Easterly Jet, is robust in both reanalysis and model datasets. Also, the simulated mean vertical ascent of moisture flux convergence and asymmetrical nature of rainfall maximum in August is comparable to observed patterns, most especially in WSM5-YSU-nSAS.

This study, however, underscores the strong potential impact of regional moisture, heat and momentum transport and redistribution on the monsoon dynamics as prescribed by the physics. It also, presented the skill of selected physics combinations to reproduce the characteristics of WAM precipitation evolution as well as its associated dynamics and thus their suitability for impact and climate studies.

5.1.3 Wet and Dry WAM Summer Rainfall Seasons

This part of the research presented the results from the simulation of wet and dry West African Monsoon (WAM) rainfall seasons using the Weather Research and Forecasting (WRF) regional climate model. The model was run for four WAM seasons

that consist of two wet (2008 and 2010) and two dry years (2001 and 2011). The four simulations were used to compute composites of wet and dry WAM rainfall seasons.

The results presented here depict that simulation of the WAM showed strong sensitivity to the choice of both the planetary boundary layer and the convection scheme. WSM5-YSU-nSAS has good agreements with observations in simulating the WAM rainfall distribution pattern because it was able to reproduce better circulations features that are associated with typical wet and dry WAM. However, the combination was unable to quantitatively differentiate between wet and dry years as compared with GD-MYJ-BMJ and WSM5-MYNN-nTDK, which produced both a good seasonal evolution and magnitude of the monsoon rainfall. On the contrary, the WSM5-MYNN-nTDK tends to underestimate rainfall along the coast especially over the western coast of West Africa and the tropical Atlantic Ocean. Simulation outputs from GD-MYJ-BMJ show moderate spatial over- and underestimates of rainfall compared with the GPCP product over the region. The inconsistent simulation of the observed circulation features related to the WAM activity caused the WSM5-MYNN-nTDK to perform less well with respect to observed rainfall. However, this combination and others were able to reproduce good vertical distributions of temperature and moisture profiles, though with warm and wet biases over land and the reverse over the ocean region. This feature is noticeable during the wet and dry WAM seasons.

Lastly, it was shown that the WRF regional climate model is capable of reproducing the main features of the large-scale circulation during wet and dry WAM rainfall years. During these periods, the three model experiments were able to capture the low-level westerly monsoon flow, middle level African Easterly Jet and upper

tropospheric Tropical Easterly Jet. Also, two of the model combinations, GD-MYJ-BMJ and WSM5-MYNN-nTDK, demonstrate significantly good skill in capturing the difference in wet and dry WAM rainfall seasons.

5.1.4 Impact of Warming on WAM

This aspect of the research examined the impact of global warming on precipitation amount during the West African monsoon season using the PGW method. Three experiments that combine microphysics, convection and planetary boundary layer parameterization schemes were also conducted for both current and PGW climate runs. Model runs were performed for selected wet (2008-2010), dry (2001-2011) and normal (2007) monsoon years over the monsoon region at 20km horizontal resolution. Also, the precipitation characteristics over the three climatic zones; Guinea Coast, Savannah, and Sahel, were analyzed. The current and PGW climate runs showed good agreement with the observed precipitation in reproducing the spatial distribution pattern over complex orographic terrains. The precipitation amount in the 2070s estimated by the PGW runs slightly increased over that of the current climate runs. In all climatic zones, the total precipitation amount simulated by the current climate is less than 16% and 63% relative to the PGW runs and the observations, respectively. However, the difference between current climate runs and observations is higher compared with the PGW runs. GD-MYJ-BMJ runs have good agreement with observations in terms of simulating the characteristics of wet, dry and normal year monsoon, which is defined by total precipitation amount. WSM5-MYNN-nTDK is more consistent in defining the precipitation characteristic in Savannah and Sahel while WSM5-YSU-nSAS rarely agree

in any two of the climatic zones. Also, found is an increase in heavy rainfall amount and a decrease in both light and moderate rainfall amount.

These results are however contingent on the GCM, which provides the boundary conditions of the RCM. Especially, the temperature change of the GCM will rather be sensitive to the change in precipitation amount. CESM1.0-CAM5.2, the GCM employed in this study, tends to provide a greater temperature change of about 4^{o}C from the 40-member ensemble of the Large Ensemble Community (LENS) project. This increase consequently leads to an increase in the simulated precipitation in the PGW experiments as it intensifies evaporation that enhances convective activities.

The projection of the precipitation is, however, limited to the average of the selected 5 years and the RCP used. Also, the role of air temperature on precipitation activity may change for different range of RCPs. Although the PGW method used in the study further reduces large scale model bias and allows the estimate of climate difference between current and future climate without an ensemble of numerous numbers of simulations, it doesn't account for extreme events. Hence, the need for longer-term simulations in future studies.

The outcomes of this research underscore the significance of the WRF model as a potentially useful tool to investigate how future WAM seasons could vary in a changing climate. This provides relevant information to improve the understanding of the possible implications of such changes on economic activities such as agriculture, water resources and other climate-sensitive sectors, and to guide the design and implementation of climate-resilient projects.

5.2 RECOMMENDATIONS

This research requires a richly dense observation network to perform a more robust evaluation of the WRF model outputs but the evaluation was however limited as the observed data were verified against satellite and reanalysis products. Therefore, there is the need for expansion of the existing observation networks in order to perform a more reliable model validation at a higher temporal and spatial scale, most especially for a highly variable parameter like rainfall.

Climate model development is a continuous process because the advent of new techniques would require a constant need to modify different aspects of the model components such as the dynamics, physics and other model elements as well as change in the algorithm of forcing datasets, that serves as sources of model error. Therefore, it is recommended that the WRF model physics combinations identified in this research should be subjected to further test so as to understanding how the combinations might behave in different atmospheric conditions and to help reduce the uncertainties that they introduce into the model's output

Lastly, the purpose of performing this research is to identify a regional climate model whose output can be used as an integral input to generate quality climate information to support decision-making process of public and private sectors on weather- and climate-related issues for socio-economic benefits. The result from this research shows the possibility of increasing rainfall and temperature under a warming climate over West Africa. Thus, the need to assess the exposure and vulnerability of the regions economy and environment to the various potential risks associated with the increased rainfall and temperature in order to identify appropriate adaptation measures that will be

relevant to increase the resilience of West African communities to climate change and variability.

REFERENCES

Abiodun, B. J., Salami, A. T., Matthew, O. J., & Odedokun, S. (2013). Potential impacts of afforestation on climate change and extreme events in Nigeria. *Climate Dynamics*, *41*(2), 277–293. https://doi.org/10.1007/s00382-012-1523-9

Afiesimama, E. A., Pal, J. S., Abiodun, B. J., Gutowski, W. J., & Adedoyin, A. (2006). Simulation of West African monsoon using the RegCM3. Part I: Model validation and interannual variability. *Theoretical and Applied Climatology*, *86*(1–4), 23–37. https://doi.org/10.1007/s00704-005-0202-8

Besler, H. (1984). The Tropical Easterly Jet as a cause for intensi ed aridity in the Sahara. *Palaeoecology of Africa*, *16*, 163–172.

Biasutti, M., Sobel, A. H., & Camargo, S. J. (2009). The role of the Sahara low in summertime Sahel rainfall variability and change in the CMIP3 models. *Journal of Climate*, *22*(21), 5755–5771. https://doi.org/10.1175/2009JCLI2969.1

Biasutti, Michela, & Giannini, A. (2006). Robust Sahel drying in response to late 20th century forcings. *Geophysical Research Letters*, *33*(11). https://doi.org/10.1029/2006GL026067

Bryson, R. A. (1973). Drought in Sahelia. Who or what is to blame? *Ecologist*, *3*(10), 366–371.

Charney, J., Quirk, W. J., Chow, S., & Kornfield, J. (1977). A Comparative Study of the Effects of Albedo Change on Drought in Semi–Arid Regions. *Journal of the Atmospheric Sciences*, Vol. 34, pp. 1366–1385. https://doi.org/10.1175/1520-0469(1977)034<1366:ACSOTE>2.0.CO;2

Chauvin, F., Roehrig, R., & Lafore, J. P. (2010). Intraseasonal variability of the saharan heat low and its link with midlatitudes. *Journal of Climate*, *23*(10), 2544–2561. https://doi.org/10.1175/2010JCLI3093.1

Chen, F., & Dudhia, J. (2001). Coupling an Advanced Land Surface–Hydrology Model with the Penn State–NCAR MM5 Modeling System. Part I: Model Implementation and Sensitivity. *Monthly Weather Review*, *129*(4), 569–585. https://doi.org/10.1175/1520-0493(2001)129<0569:CAALSH>2.0.CO;2

Chen, T. C. (2005). Maintenance of the midtropospheric North African summer circulation; Saharan high and African easterly jet. *Journal of Climate*, *18*(15), 2943–

2962. https://doi.org/10.1175/JCLI3446.1

Collins, M., Knutti, R., Arblaster, J., Dufresne, J.-L., Fichefet, T., Friedlingstein, P., … Wehner, M. (2013). IPCC AR5 (2013) Chapter 12: Long-term Climate Change: Projections, Commitments and Irreversibility. *Climate Change 2013: The Physical Science Basis. Contribution of Working Group I to the Fifth Assessment Report of the Intergovernmental Panel on Climate Change (Pp. 1029-1136). Cambridge University Press.* https://doi.org/10.1017/CBO9781107415324.024

Cook, K. H. (1999). Generation of the African easterly jet and its role in determining West African precipitation. *Journal of Climate*, *12*(5), 1165–1184. https://doi.org/10.1175/1520-0442(1999)012<1165:GOTAEJ>2.0.CO;2

Cornforth, R. J., Hoskins, B. J., & Thorncroft, C. D. (2009). The impact of moist processes on the African Easterly Jet-African Easterly Wave system. *Quarterly Journal of the Royal Meteorological Society*, *135*(641), 894–913. https://doi.org/10.1002/qj.414

Dai, A., Lamb, P. J., Trenberth, K. E., Hulme, M., Jones, P. D., & Xie, P. (2004). The recent Sahel drought is real. *International Journal of Climatology*, *24*(11), 1323–1331. https://doi.org/10.1002/joc.1083

Dee, D. P., Uppala, S. M., Simmons, A. J., Berrisford, P., Poli, P., Kobayashi, S., … Vitart, F. (2011). The ERA-Interim reanalysis: Configuration and performance of the data assimilation system. *Quarterly Journal of the Royal Meteorological Society*, *137*(656), 553–597. https://doi.org/10.1002/qj.828

Dezfuli, A. K., & Nicholson, S. E. (2011). A note on long-term variations of the African easterly jet. *International Journal of Climatology*, *31*(13), 2049–2054. https://doi.org/10.1002/joc.2209

Dhonneur, G. (1971). General circulation and types of weather over Western and Central Africa. *Annex-IV GARP-GATE 2*, 22.

Diagne, K. (2007). Governance and natural disasters: Addressing flooding in Saint Louis, Senegal. *Environment and Urbanization*, *19*(2), 552–562. https://doi.org/10.1177/0956247807082836

Diallo, I., & Sylla, M. B. (2012). *Interannual variability of rainfall over the Sahel based on multiple regional climate models simulations*. https://doi.org/10.1007/s00704-

012-0791-y

Diedhiou, A., Janicot, S., Viltard, A., & De Felice, P. (1998). Evidence of two regimes of easterly waves over West Africa and the tropical Atlantic. *Geophysical Research Letters*, *25*, 2805–2808. https://doi.org/10.1029/98GL02152

Druyan, L. M., Feng, J., Cook, K. H., Xue, Y., Fulakeza, M., Hagos, S. M., … Ibrah, S. S. (2010). The WAMME regional model intercomparison study. *Climate Dynamics*, *35*(1), 175–192. https://doi.org/10.1007/s00382-009-0676-7

Druyan, L. M., Fulakeza, M., Lonergan, P., & Noble, E. (2009). Regional climate model simulation of the AMMA Special Observing Period #3 and the pre-Helene easterly wave. *Meteorology and Atmospheric Physics*, *105*(3–4), 191–210. https://doi.org/10.1007/s00703-009-0044-5

Dudhia, J. (2010). *Overview of WRF Physics*. *University Corporation for Atmospheric Research, Boulder, CO, http://www2.mmm.ucar.edu/wrf/users/tutorial/201401/Physics_full.pdf*

Duvel, J. P. (1990). Convection over Tropical Africa and the Atlantic Ocean during Northern Summer. Part II: Modulation by Easterly Waves. *Monthly Weather Review*, *118*, 1855–1868. https://doi.org/10.1175/1520-0493(1990)118<1855:cotaat>2.0.co;2

Eltahir, E. A. B., & Gong, C. (1995). Ocean-Atmosphere-Land Interactions and Rainfall in the Sahel. *Transactions of the American Geophysical Union*, *74*(46), F91.

Eltahir, E. A B, & Cuiling Gong. (1996). Dynamics of wet and dry years in West Africa. *Journal of Climate*, *9*(5), 1030–1042. https://doi.org/10.1175/1520-0442(1996)009<1030:DOWADY>2.0.CO;2

Eltahir, Elfatih A.B. (1998). A soil moisture-rainfall feedback mechanism 1. Theory and observations. *Water Resources Research*, *34*(4), 765–776. https://doi.org/10.1029/97WR03499

FAO. (2009). *Food and Agricultural Organization of the United Nations, FAO Statistical Yearbook 2009*.

Findell, K. L., & Eltahir, E. A. B. (2003). Atmospheric Controls on Soil Moisture–Boundary Layer Interactions. Part I: Framework Development. *Journal of Hydrometeorology*, *4*(3), 552–569. https://doi.org/10.1175/1525-

7541(2003)004<0552:acosml>2.0.co;2

Flaounas, E., Bastin, S., & Janicot, S. (2011). Regional climate modelling of the 2006 West African monsoon: Sensitivity to convection and planetary boundary layer parameterisation using WRF. *Climate Dynamics*, *36*(5–6), 1083–1105. https://doi.org/10.1007/s00382-010-0785-3

Flohn, H. (1964). The tropical easterly jet. *Bonner Meteorologische Abhandlungen*, *4*, 1–69.

Fontaine, B., Trzaska, S., & Janicot, S. (1998). Evolution of the relationship between near global and Atlantic SST modes and the rainy season in West Africa: statistical analyses and sensitivity experiments. *Climate Dynamics*, *14*(5), 353–368. https://doi.org/10.1007/s003820050228

Freeman, L. (2017). Environmental Change, Migration, and Conflict in Africa: A Critical Examination of the Interconnections. *Journal of Environment and Development*, *26*(4), 351–374. https://doi.org/10.1177/1070496517727325

Gallée, H., Moufouma-Okia, W., Bechtold, P., Brasseur, O., Dupays, I., Marbaix, P., … Lebel, T. (2004). A high-resolution simulation of a West African rainy season using a regional climate model. *Journal of Geophysical Research*, *109*(D5). https://doi.org/10.1029/2003jd004020

Gbode, Imole Ezekiel, Akinsanola, A. A., & Ajayi, V. O. (2015). Recent Changes of Some Observed Climate Extreme Events in Kano. *International Journal of Atmospheric Sciences*. https://doi.org/10.1155/2015/298046

Gbode, Imoleayo E., Dudhia, J., Ogunjobi, K. O., & Ajayi, V. O. (2019). Sensitivity of different physics schemes in the WRF model during a West African monsoon regime. *Theoretical and Applied Climatology*, *136*(1–2), 733–751. https://doi.org/10.1007/s00704-018-2538-x

Giannini, A., Saravanan, R., & Chang, P. (2003). Oceanic forcing of Sahel rainfall on interannual to interdecadal time scales. *Science*, *302*(5647), 1027–1030. https://doi.org/10.1126/science.1089357

Giorgi, F, Jones, C., & Asrar, G. R. (2009). Addressing climate information needs at the regional level: the CORDEX framework. *Bulletin - World Meteorological Organization*, *58*(3), 175–183.

Giorgi, Filippo, & Mearns, L. O. (1999). Introduction to special section: Regional Climate Modeling Revisited. *Journal of Geophysical Research*, *104*(D6), 6335. https://doi.org/10.1029/98JD02072

Grell, G. A., & Freitas, S. R. (2014). A scale and aerosol aware stochastic convective parameterization for weather and air quality modeling. *Atmospheric Chemistry and Physics*, *14*(10), 5233–5250. https://doi.org/10.5194/acp-14-5233-2014

Grist, J.P., Nicholson, S. E., & Barcilon, A. I. (2002). Easterly waves over Africa. II: observed and modeled contrasts between wet and dry years. *Monthly Weather Review*, *130*(2), 212–225. https://doi.org/10.1175/1520-0493(2002)130<0212:EWOAPI>2.0.CO;2

Grist, Jeremy P., & Nicholson, S. E. (2001). A Study of the Dynamic Factors Influencing the Rainfall Variability in the West African Sahel. *Journal of Climate*, *14*(7), 1337–1359. https://doi.org/10.1175/1520-0442(2001)014<1337:ASOTDF>2.0.CO;2

Grodsky, S. A., Carton, J. A., & Nigam, S. (2003). Near surface westerly wind jet in the Atlantic ITCZ. *Geophysical Research Letters*, *30*(19), 1–4. https://doi.org/10.1029/2003GL017867

Gu, G., & Adler, R. F. (2004). Seasonal evolution and variability associated with the West African monsoon system. *Journal of Climate*, *17*(17), 3364–3377. https://doi.org/10.1175/1520-0442(2004)017<3364:SEAVAW>2.0.CO;2

Hagos, S. M., & Cook, K. H. (2007a). Dynamics of the West African monsoon jump. *Journal of Climate*, *20*(21), 5264–5284. https://doi.org/10.1175/2007JCLI1533.1

Hagos, S. M., & Cook, K. H. (2007b). Dynamics of the West African monsoon jump. *Journal of Climate*, *20*(21), 5264–5284. https://doi.org/10.1175/2007JCLI1533.1

Hagos, S. M., & Cook, K. H. (2008). Ocean warming and late-twentieth-century Sahel drought and recovery. *Journal of Climate*, *21*(15), 3797–3814. https://doi.org/10.1175/2008JCLI2055.1

Hall, N. M. J., Kiladis, G. N., & Thorncroft, C. D. (2006). Three-Dimensional Structure and Dynamics of African Easterly Waves. Part II: Dynamical Modes. *Journal of the Atmospheric Sciences*, *63*(9), 2231–2245. https://doi.org/10.1175/JAS3742.1

Han, J., & Pan, H.-L. (2011). Revision of Convection and Vertical Diffusion Schemes in the NCEP Global Forecast System. *Weather and Forecasting*, *26*(4), 520–533.

https://doi.org/10.1175/waf-d-10-05038.1

Hara, M., Yoshikane, T., Kawase, H., & Kimura, F. (2008). Estimation of the Impact of Global Warming on Snow Depth in Japan by the Pseudo-Global-Warming Method. *Hydrological Research Letters*, *2*, 61–64. https://doi.org/10.3178/hrl.2.61

Held, I. M., & Soden, B. J. (2006). Robust responses of the hydrological cycle to global warming. *J. Climate*, *19*(21), 5686–5699.

Hernández-Díaz, L., Laprise, R., Sushama, L., Martynov, A., Winger, K., & Dugas, B. (2013). Climate simulation over CORDEX Africa domain using the fifth-generation Canadian Regional Climate Model (CRCM5). *Climate Dynamics*, *40*(5–6), 1415–1433. https://doi.org/10.1007/s00382-012-1387-z

Hoerling, M., Hurrell, J., Eischeid, J., & Phillips, A. (2006). Detection and attribution of twentieth-century northern and southern African rainfall change. *Journal of Climate*, *19*(16), 3989–4008. https://doi.org/10.1175/JCLI3842.1

Hong, S.-Y., Dudhia, J., & Chen, S.-H. (2004). A Revised Approach to Ice Microphysical Processes for the Bulk Parameterization of Clouds and Precipitation. *Monthly Weather Review*, *132*(1), 103–120. https://doi.org/10.1175/1520-0493(2004)132<0103:ARATIM>2.0.CO;2

Hong, S.-Y., Noh, Y., & Dudhia, J. (2006). A New Vertical Diffusion Package with an Explicit Treatment of Entrainment Processes. *Monthly Weather Review*, *134*(9), 2318–2341. https://doi.org/10.1175/mwr3199.1

Hourdin, F., Musat, I., Guichard, F. se, Ruti, P. M., Favot, F., Filiberti, M.-A., … Gallée, H. (2010). AMMA-model intercomparison project. *Bulletin of the American Meteorological Society*, *91*(1), 95–104. https://doi.org/10.1175/2009BAMS2791.1

Huffman, G.J., Bolvin, D. T., & Adler, R. F. (2016). *GPCP Version 1.2 One- Degree Daily Precipitation Data Set. Research Data Archive at the National Center for Atmospheric Research, Computational and Information Systems Laboratory.* https://doi.org/https://doi.org/10.5065/ D6D50K46

Huffman, George J., Adler, R. F., Bolvin, D. T., & Gu, G. (2009). Improving the global precipitation record: GPCP Version 2.1. *Geophysical Research Letters*, *36*(17). https://doi.org/10.1029/2009GL040000

Huffman, George J., Bolvin, D. T., Nelkin, E. J., Wolff, D. B., Adler, R. F., Gu, G., …

Stocker, E. F. (2007). The TRMM Multisatellite Precipitation Analysis (TMPA): Quasi-Global, Multiyear, Combined-Sensor Precipitation Estimates at Fine Scales. *Journal of Hydrometeorology*, *8*(1), 38–55. https://doi.org/10.1175/jhm560.1

Hulme, M., & Tosdevin, N. (1989). The Tropical easterly Jet and Sudan rainfall: A review. *Theoretical and Applied Climatology*, *39*(4), 179–187. https://doi.org/10.1007/BF00867945

Hulme, M. (1994). Regional Climate-Change Scenarios Based on IPCC Emissions Projections with Some Illustrations for Africa. *Area*, *26*, 33–44.

Hulme, Mike. (1992). Rainfall changes in Africa: 1931–1960 to 1961–1990. *International Journal of Climatology*, *12*(7), 685–699. https://doi.org/10.1002/joc.3370120703

Hulme, Mike. (2001). Climatic perspectives on Sahelian desiccation: 1973-1998. *Global Environmental Change*, *11*(1), 19–29. https://doi.org/10.1016/S0959-3780(00)00042-X

Iacono, M. J., Delamere, J. S., Mlawer, E. J., Shephard, M. W., Clough, S. A., & Collins, W. D. (2008). Radiative forcing by long-lived greenhouse gases: Calculations with the AER radiative transfer models. *Journal of Geophysical Research Atmospheres*, *113*(D13). https://doi.org/10.1029/2008JD009944

Iloeje, N. P. (1981). *A New Geography of Nigeria. Longman, UK*.

Im, E. S., Gianotti, R. L., & Eltahir, E. A. B. (2014). Improving the simulation of the West African monsoon using the MIT regional climate model. *Journal of Climate*, *27*(6), 2209–2229. https://doi.org/10.1175/JCLI-D-13-00188.1

Intergovenmental Panel on Climate Change (IPCC) (2000). *Special report on emissions scenarios (SRES), a special report of Working Group III. edited by Nakicenovic, N., Alcamo, J., Grubler, A., Riahi, K., Roehrl, R.A., Rogner, H.H. and Victor, N. Cambridge University Press.*

Intergovenmental Panel on Climate Change (IPCC) (2007). Climate Change 2007 - The Physical Science Basis: Working Group I Contribution to the Fourth Assessment Report of the IPCC. *Science*, (October 2009), 1009. https://doi.org/volume

Intergovenmental Panel on Climate Change (IPCC) (2001). *Climate Change 2001: The Scientific Basis. Contribution of Working Group I to the Third Assessment Report of*

the Intergovernmental Panel on Climate Change, edited by J. T. Houghton et al., 881 pp., Cambridge Univ. Press, New York.

Intergovenmental Panel on Climate Change (IPCC) (2014). *Climate Change 2014: synthesis report. Contribution of Working Groups I. II and III to the Fifth Assessment Report edited by Team, C.W., Pachauri, R.K. and Meyer, L.A., Geneva, Switzerland, 151.*

Intergovenmental Panel on Climate Change (IPCC) (2018). *Global warming of 1.5°C. An IPCC Special Report on the impacts of global warming of 1.5°C above pre-industrial levels and related global greenhouse gas emission pathways, in the context of strengthening the global response to the threat of climate change,.*

Janicot, S., Thorncroft, C. D., Ali, A., Asencio, N., Berry, G., Bock, O., … Ulanovsky, A. (2008). Large-scale overview of the summer monsoon over West Africa during the AMMA field experiment in 2006. *Annales Geophysicae*, *26*(9), 2569–2595. https://doi.org/10.5194/angeo-26-2569-2008

Janicot, Serge, Thorncroft, C. D., Ali, A., Asencio, N., Berry, G., Bock, O., … Ulanovsky, A. (2008). Large-scale overview of the summer monsoon over West Africa during the AMMA field experiment in 2006. *Annales Geophysicae*, *26*, 2569–2595. https://doi.org/10.5194/angeo-26-2569-2008

Janjić, Z. I. (1994). The Step-Mountain Eta Coordinate Model: Further Developments of the Convection, Viscous Sublayer, and Turbulence Closure Schemes. *Monthly Weather Review*, *122*(5), 927–945. https://doi.org/10.1175/1520-0493(1994)122<0927:tsmecm>2.0.co;2

Janjić, Z. I. (2000). Comments on "Development and Evaluation of a Convection Scheme for Use in Climate Models." *Journal of the Atmospheric Sciences*, *57*(21), 3686–3686. https://doi.org/10.1175/1520-0469(2000)057<3686:codaeo>2.0.co;2

Jenkins, G. S., Gaye, A. T., & Sylla, B. (2005). Late 20th century attribution of drying trends in the Sahel from the Regional Climate Model (RegCM3). *Geophysical Research Letters*, *32*(22). https://doi.org/10.1029/2005GL024225

Jones, P. W. (1999). First- and Second-Order Conservative Remapping Schemes for Grids in Spherical Coordinates. *Monthly Weather Review*, *127*(9), 2204–2210. https://doi.org/10.1175/1520-0493(1999)127<2204:fasocr>2.0.co;2

Joyce, R. J., Janowiak, J. E., Arkin, P. A., & Xie, P. (2004). CMORPH: A Method that Produces Global Precipitation Estimates from Passive Microwave and Infrared Data at High Spatial and Temporal Resolution. *Journal of Hydrometeorology*, *5*, 487–503. https://doi.org/10.1175/1525-7541(2004)005<0487:camtpg>2.0.co;2

Kain, J. S. (2004). The Kain–Fritsch Convective Parameterization: An Update. *Journal of Applied Meteorology*, *43*, 170–181. https://doi.org/10.1175/1520-0450(2004)043<0170:tkcpau>2.0.co;2

Kalapureddy, M. C. R., Lothon, M., Campistron, B., Lohou, F., & Saïd, F. (2010). Wind profiler analysis of the African Easterly Jet in relation with the boundary layer and the Saharan heat-low. *Quarterly Journal of the Royal Meteorological Society*, *136*(1), 77–91. https://doi.org/10.1002/qj.494

Kalnay, E., Kanamitsu, M., Kistler, R., Collins, W., Deaven, D., Gandin, L., … Joseph, D. (1996). The NCEP/NCAR 40-year reanalysis project. *Bulletin of the American Meteorological Society*, *77*(3), 437–472. https://doi.org/10.1175/1520-0477(1996)077<0437:TNYRP>2.0.CO;2

Kamga Foamouhoue, A., & Buscarlet, E. (2006). Simulation du climat de l'Afrique de l'Ouest à l'aide d'un modèle climatique régional : Validation sur la période 1961-1990. *La Météorologie*. https://doi.org/10.4267/2042/20053

Kanamitsu, M., Ebisuzaki, W., Woollen, J., Yang, S. K., Hnilo, J. J., Fiorino, M., & Potter, G. L. (2002). NCEP-DOE AMIP-II reanalysis (R-2). *Bulletin of the American Meteorological Society*, *83*(11), 1631–1644.

Kay, J. E., Deser, C., Phillips, A., Mai, A., Hannay, C., Strand, G., … Vertenstein, M. (2015). The community earth system model (CESM) large ensemble project : A community resource for studying climate change in the presence of internal climate variability. *Bulletin of the American Meteorological Society*, *96*(8), 1333–1349. https://doi.org/10.1175/BAMS-D-13-00255.1

Kimura, F., & Kitoh, A. (2007). Downscaling by Pseudo Global Warning Method. In *The Final Report of ICCAP*.

Klein, C., Heinzeller, D., Bliefernicht, J., & Kunstmann, H. (2015). Variability of West African monsoon patterns generated by a WRF multi-physics ensemble. *Climate Dynamics*, *45*(9–10), 2733–2755. https://doi.org/10.1007/s00382-015-2505-5

Klutse, N. A. B., Ajayi, V. O., Gbobaniyi, E. O., Egbebiyi, T. S., Kouadio, K., Nkrumah, F., … Dosio, A. (2018). Potential impact of 1.5 °c and 2 °c global warming on consecutive dry and wet days over West Africa. *Environmental Research Letters*, *13*(5), 055013. https://doi.org/10.1088/1748-9326/aab37b

Kraus, E. B. (1977). Subtropical Droughts and Cross-Equatorial Energy Transports. *Monthly Weather Review*, *105*, 1009–1018. https://doi.org/10.1175/1520-0493(1977)105<1009:sdacee>2.0.co;2

L'Hôte, Y., Mahé, G., Somé, B., & Triboulet, J. P. (2002). Analysis of a Sahelian annual rainfall index from 1896 to 2000; the drought continues. *Hydrological Sciences Journal*, *47*(4), 563–572. https://doi.org/10.1080/02626660209492960

Lafore, J. P., Flamant, C., Giraud, V., Guichard, F., Knippertz, P., Mahfouf, J. F., … Williams, E. R. (2010). Introduction to the AMMA Special Issue on "Advances in understanding atmospheric processes over West Africa through the AMMA field campaign." *Quarterly Journal of the Royal Meteorological Society*, *136*(s1), 2–7. https://doi.org/10.1002/qj.583

Lavaysse, C., Flamant, C., & Janicot, S. (2010). Regional-scale convection patterns during strong and weak phases of the Saharan heat low. *Atmospheric Science Letters*, *11*(4), 255–264. https://doi.org/10.1002/asl.284

Lavaysse, C., Flamant, C., Janicot, S., & Knippertz, P. (2010). Links between African easterly waves, midlatitude circulation and intraseasonal pulsations of the West African heat low. *Quarterly Journal of the Royal Meteorological Society*, *136*(1), 141–158. https://doi.org/10.1002/qj.555

Lavaysse, Christophe, Flamant, C., Janicot, S., Parker, D. J., Lafore, J. P., Sultan, B., & Pelon, J. (2009). Seasonal evolution of the West African heat low: A climatological perspective. *Climate Dynamics*, *33*(2–3), 313–330. https://doi.org/10.1007/s00382-009-0553-4

Le Barbé, L., Lebel, T., & Tabsoba, D. (2002). Rainfall Variability in West Africa during the Years 1950 – 90. *Journal of Climate*, *15*(2), 187–202. https://doi.org/10.1175/1520-0442(2002)015<0187:RVIWAD>2.0.CO;2

Lebel, T., Diedhiou, A., & Laurent, H. (2003). Seasonal cycle and interannual variability of the Sahelian rainfall at hydrological scales. *Journal of Geophysical Research*,

108, 8389. https://doi.org/10.1029/2001jd001580

Levermann, A., Schewe, J., Petoukhov, V., & Held, H. (2009). Basic mechanism for abrupt monsoon transitions. *Proceedings of the National Academy of Sciences*, *106*(49), 20572–20577. https://doi.org/10.1073/pnas.0901414106

Li, R., Jin, J., Wang, S. Y., & Gillies, R. R. (2015a). Significant impacts of radiation physics in the Weather Research and Forecasting model on the precipitation and dynamics of the West African Monsoon. *Climate Dynamics*, *44*(5–6), 1583–1594. https://doi.org/10.1007/s00382-014-2294-2

Li, R., Jin, J., Wang, S. Y., & Gillies, R. R. (2015b). Significant impacts of radiation physics in the Weather Research and Forecasting model on the precipitation and dynamics of the West African Monsoon. *Climate Dynamics*, *44*(5–6), 1583–1594. https://doi.org/10.1007/s00382-014-2294-2

Lin, Y.-L., Farley, R. D., & Orville, H. D. (1983). Bulk Parameterization of the Snow Field in a Cloud Model. *Journal of Climate and Applied Meteorology*, *22*(6), 1065–1092. https://doi.org/10.1175/1520-0450(1983)022<1065:bpotsf>2.0.co;2

Liu, C., Ikeda, K., Rasmussen, R., Barlage, M., Newman, A. J., Prein, A. F., … Yates, D. (2017). Continental-scale convection-permitting modeling of the current and future climate of North America. *Climate Dynamics*, *49*(1–2), 71–95. https://doi.org/10.1007/s00382-016-3327-9

Maynard, K., Royer, J. F., & Chauvin, F. (2002). Impact of greenhouse warming on the West African summer monsoon. *Climate Dynamics*, *19*(5–6), 499–514. https://doi.org/10.1007/s00382-002-0242-z

Meinshausen, M., Smith, S. J., Calvin, K., Daniel, J. S., Kainuma, M. L. T., Lamarque, J., … van Vuuren, D. P. P. (2011). The RCP greenhouse gas concentrations and their extensions from 1765 to 2300. *Climatic Change*, *109*(1–2), 213. https://doi.org/10.1007/s10584-011-0156-z

Miles, M. K., & Follard, C. K. (1974). Changes in the latitude of the climatic zones of the Northern Hemisphere. *Nature*, *252*(5484), 616.

Mori, S., Jun-Ichi, H., Tauhid, Y. I., Yamanaka, M. D., Okamoto, N., Murata, F., … Sribimawati, T. (2004). Diurnal land-sea rainfall peak migration over Sumatera Island, Indonesian Maritime Continent, observed by TRMM satellite and intensive

rawinsonde soundings. *Monthly Weather Review*, *132*, 2021–2039. https://doi.org/10.1175/1520-0493(2004)132<2021:DLRPMO>2.0.CO;2

Mounier, F., Janicot, S., & Kiladis, G. N. (2008). The West African Monsoon Dynamics. Part III: The Quasi-Biweekly Zonal Dipole. *Journal of Climate*, *21*(9), 1911–1928. https://doi.org/10.1175/2007JCLI1706.1

Nakanishi, M., & Niino, H. (2004). An improved Mellor-Yamada Level-3 model with condensation physics: Its design and verification. *Boundary-Layer Meteorology*, *112*(1), 1–31. https://doi.org/10.1023/B:BOUN.0000020164.04146.98

Nakanishi, M., & Niino, H. (2006). An improved Mellor-Yamada Level-3 model: Its numerical stability and application to a regional prediction of advection fog. *Boundary-Layer Meteorology*, *119*(2), 397–407. https://doi.org/10.1007/s10546-005-9030-8

National Center for Environmental Information (NCEI), National Oceanic and Atmospheric Administration (NOAA). (2019). Definition of drought. *https://www.ncdc.noaa.gov/monitoring-references/dyk/drought-definition*. (accessed on 14th March 2019)

NCEP-FNL. (2000). *National Centers for Environmental Prediction/National Weather Service/ NOAA/U.S. Department of Commerce (2000) updated daily. NCEP FNL Operational Model Global Tropospheric Analyses, continuing from July 1999. Research Data Archive at the National Center*.

Newell, R. E., & Kidson, J. W. (1984). African mean wind changes between sahelian wet and dry periods. *Journal of Climatology*, *4*(1), 27–33. https://doi.org/10.1002/joc.3370040103

Nicholson, S. E., Barcilon, a. I., & Challa, M. (2008). An Analysis of West African Dynamics Using a Linearized GCM*. *Journal of the Atmospheric Sciences*, *65*(4), 1182–1203. https://doi.org/10.1175/2007JAS2194.1

Nicholson, S. E., & Grist, J. P. (2001). A conceptual model for understanding rainfall variability in the West African Sahel on interannual and interdecadal timescales. *International Journal of Climatology*, *21*(14), 1733–1757. https://doi.org/10.1002/joc.648

Nicholson, S. E., Some, B., & Kone, B. (2000). An analysis of recent rainfall conditions

in West Africa, including the rainy seasons of the 1997 El Nino and the 1998 La Nina years. *Journal of Climate*, *13*(14), 2628–2640. https://doi.org/10.1175/1520-0442(2000)013<2628:AAORRC>2.0.CO;2

Nicholson, Sharon E. (1981). Rainfall and Atmospheric Circulation during Drought Periods and Wetter Years in West Africa. *Monthly Weather Review*, *109*(10), 2191–2208. https://doi.org/10.1175/1520-0493(1981)109<2191:raacdd>2.0.co;2

Nicholson, Sharon E. (1989). African Drought: Characteristics, Causal Theories and Global Teleconnections. *American Geophysical Union, Geophysical Monograph*, *52*(IUGG 7), 79–100. https://doi.org/10.1029/gm052p0079

Nicholson, Sharon E. (2008). The intensity, location and structure of the tropical rainbelt over west Africa as factors in interannual variability. *International Journal of Climatology*, *28*(13), 1775–1785. https://doi.org/10.1002/joc.1507

Nicholson, Sharon E. (2009a). A revised picture of the structure of the "monsoon" and land ITCZ over West Africa. *Climate Dynamics*, Vol. 32, pp. 1155–1171. https://doi.org/10.1007/s00382-008-0514-3

Nicholson, Sharon E. (2009b). On the factors modulating the intensity of the tropical rainbelt over West Africa. *International Journal of Climatology*, *29*(5), 673–689. https://doi.org/10.1002/joc.1702

Nicholson, Sharon E., & Grist, J. P. (2003). The seasonal evolution of the atmospheric circulation over West Africa and equatorial Africa. *Journal of Climate*, *16*, 1013–1030. https://doi.org/10.1175/1520-0442(2003)016<1013:TSEOTA>2.0.CO;2

Nicholson, Sharon E., & Webster, P. J. (2007). A physical basis for the interannual variability of rainfall in the Sahel. *Quarterly Journal of the Royal Meteorological Society*, *133*, 2065–2084. https://doi.org/10.1002/qj.104

Nicholson, Sharon E. (2013). *The West African Sahel : A Review of Recent Studies on the Rainfall Regime and Its Interannual Variability*. *2013*.

Nikulin, G., Jones, C., Giorgi, F., Asrar, G., Büchner, M., Cerezo-Mota, R., … Sushama, L. (2012). Precipitation climatology in an ensemble of CORDEX-Africa regional climate simulations. *Journal of Climate*, *25*(18), 6057–6078. https://doi.org/10.1175/JCLI-D-11-00375.1

Noble, E., Druyan, L. M., & Fulakeza, M. (2014). The Sensitivity of WRF Daily

Summertime Simulations over West Africa to Alternative Parameterizations. Part I: African Wave Circulation. *Monthly Weather Review*, *142*(4), 1588–1608. https://doi.org/10.1175/MWR-D-13-00194.1

Noble, E., Druyan, L. M., & Fulakeza, M. (2017). The Sensitivity of WRF Daily Summertime Simulations over West Africa to Alternative Parameterizations. Part II: Precipitation. *Monthly Weather Review*, *145*(1), 215–233. https://doi.org/10.1175/mwr-d-15-0294.1

Nolan, D. S., Zhang, C., & Chen, S. (2007). Dynamics of the Shallow Meridional Circulation around Intertropical Convergence Zones. *Journal of the Atmospheric Sciences*, *64*(7), 2262–2285. https://doi.org/10.1175/jas3964.1

Oguntunde, P. G., Abiodun, B. J., & Lischeid, G. (2011). Rainfall trends in Nigeria, 1901-2000. *Journal of Hydrology*, *411*, 207–218. https://doi.org/10.1016/j.jhydrol.2011.09.037

Omotosho, J. B., & Abiodun, B. J. (2007). A numerical study of moisture build-up and rainfall over West Africa. *Meteorological Applications*, *14*(3), 209–225. https://doi.org/10.1002/met.11

Paeth, H., Born, K., Podzun, R., & Jacob, D. (2005). Regional dynamical downscaling over West Africa: Model evaluation and comparison of wet dry years. *Meteorologische Zeitschrift*, *14*(3), 349–367. https://doi.org/10.1127/0941-2948/2005/0038

Paeth, H., Hall, N. M. J., Gaertner, M. A., Alonso, M. D., Moumouni, S., Polcher, J., … Rummukainen, M. (2011). Progress in regional downscaling of west African precipitation. *Atmospheric Science Letters*, *12*(1), 75–82. https://doi.org/10.1002/asl.306

Paeth, H., & Hense, A. (2004). SST versus climate change signals in West African rainfall: 20th-century variations and future projections. *Climatic Change*, *65*(1–2), 179–208. https://doi.org/10.1023/B:CLIM.0000037508.88115.8a

Pal, J. S., Giorgi, F., Bi, X., Elguindi, N., Solmon, F., Gao, X., … Steiner, A. L. (2007). Regional climate modeling for the developing world: The ICTP RegCM3 and RegCNET. *Bulletin of the American Meteorological Society*, *88*(9), 1395–1410. https://doi.org/10.1175/BAMS-88-9-1395

Parker, D. J., Burton, R. R., Diongue-Niang, A., Ellis, R. J., Felton, M., Taylor, C. M., … Tompkins, A. M. (2005). The diurnal cycle of the West African monsoon circulation. *Quarterly Journal of the Royal Meteorological Society*, *131*, 2839–2860. https://doi.org/10.1256/qj.04.52

Pattanaik, D. R., & Satyan, V. (2000). Fluctuations of Tropical Easterly Jet during contrasting monsoons over India: A GCM study. *Meteorology and Atmospheric Physics*, *75*(1–2), 51–60. https://doi.org/10.1007/s007030070015

Pelling, M., & Wisner, B. (2009). *Disaster Risk Reduction: Cases from Urban Africa, Earthscan*.

Pohl, B., & Douville, H. (2011a). Diagnosing GCM errors over West Africa using relaxation experiments. Part I: Summer monsoon climatology and interannual variability. *Climate Dynamics*, *37*(7–8), 1293–1312. https://doi.org/10.1007/s00382-010-0911-2

Pohl, B., & Douville, H. (2011b). Diagnosing GCM errors over West Africa using relaxation experiments. Part II: Intraseasonal variability and African easterly waves. *Climate Dynamics*, *37*(7–8), 1313–1334. https://doi.org/10.1007/s00382-011-1106-1

Prein, A. F., Gobiet, A., Suklitsch, M., Truhetz, H., Awan, N. K., Keuler, K., & Georgievski, G. (2013). Added value of convection permitting seasonal simulations. *Climate Dynamics*, *41*, 2655–2677. https://doi.org/10.1007/s00382-013-1744-6

Prein, Andreas F., Langhans, W., Fosser, G., Ferrone, A., Ban, N., Goergen, K., … Leung, R. (2015). A review on regional convection-permitting climate modeling: Demonstrations, prospects, and challenges. *Reviews of Geophysics*, *53*(2), 323–361. https://doi.org/10.1002/2014RG000475

Pu, B., & Cook, K. H. (2010). Dynamics of the West African westerly jet. *Journal of Climate*, *23*(23), 6263–6276. https://doi.org/10.1175/2010JCLI3648.1

Pu, B., & Cook, K. H. (2012). Role of the west African westerly jet in sahel rainfall variations. *Journal of Climate*, *25*(8), 2880–2896. https://doi.org/10.1175/JCLI-D-11-00394.1

Rao, B. R. S., Rao, D. V. B., & Rao, V. B. (2004). Decreasing trend in the strength of Tropical Easterly Jet during the Asian summer monsoon season and the number of tropical cyclonic systems over Bay of Bengal. *Geophysical Research Letters*,

31(14), L141031–L141033. https://doi.org/10.1029/2004GL019817

Rasmussen, R., Ikeda, K., Liu, C., Gochis, D., Clark, M., Dai, A., … Zhang, G. (2014). Climate Change Impacts on the Water Balance of the Colorado Headwaters: High-Resolution Regional Climate Model Simulations. *Journal of Hydrometeorology*, *15*(3), 1091–1116. https://doi.org/10.1175/jhm-d-13-0118.1

Rasmussen, R., Liu, C., Ikeda, K., Gochis, D., Yates, D., Chen, F., … Gutmann, E. (2011). High-resolution coupled climate runoff simulations of seasonal snowfall over Colorado: A process study of current and warmer climate. *Journal of Climate*, *24*(12), 3015–3048. https://doi.org/10.1175/2010JCLI3985.1

Redelsperger, J.-L., Diongue, a., Diedhiou, a., Ceron, J.-P., Diop, M., Gueremy, J.-F., & Lafore, J.-P. (2002). Multi-scale description of a Sahelian synoptic weather system representative of the West African monsoon. *Quarterly Journal of the Royal Meteorological Society*, *128*, 1229–1257. https://doi.org/10.1256/003590002320373274

Redelsperger, Jean-Luc, Thorncroft, C. D., Diedhiou, A., Lebel, T., Parker, D. J., & Polcher, J. (2006). African Monsoon Multidisciplinary Analysis: An International Research Project and Field Campaign. *Bulletin of the American Meteorological Society*, *87*(12), 1739–1746. https://doi.org/10.1175/BAMS-87-12-1739

Riahi, K., Rao, S., Krey, V., Cho, C., Chirkov, V., Fischer, G., … Rafaj, P. (2011). RCP 8.5-A scenario of comparatively high greenhouse gas emissions. *Climatic Change*, *109*(1–2), 33. https://doi.org/10.1007/s10584-011-0149-y

Rienecker, M. M., Suarez, M. J., Gelaro, R., Todling, R., Bacmeister, J., Liu, E., … Woollen, J. (2011). MERRA: NASA's modern-era retrospective analysis for research and applications. *Journal of Climate*, *24*(14), 3624–3648. https://doi.org/10.1175/JCLI-D-11-00015.1

Rind, D., Goldberg, R., Hansen, J., Rosenzweig, C., & Ruedy, R. (1990). Potential evapotranspiration and the likelihood of future drought. *Journal of Geophysical Research: Atmospheres*, *95*, 9983-10,004. https://doi.org/10.1029/jd095id07p09983

Roja Raman, M., Jagannadha Rao, V. V. M., Venkat Ratnam, M., Rajeevan, M., Rao, S. V. B., Narayana Rao, D., & Prabhakara Rao, N. (2009). Characteristics of the Tropical Easterly Jet: Long-term trends and their features during active and break

monsoon phases. *Journal of Geophysical Research Atmospheres*, *114*(19), Article ID D19105. https://doi.org/10.1029/2009JD012065

Rowlands, I. H. (1996). South Africa and global climate change. *J Mod Af Stud*, *34*, 163–178.

Rummukainen, M. (2010). State-of-the-art with regional climate models. *Wiley Interdisciplinary Reviews: Climate Change*, *1*(1), 82–96. https://doi.org/10.1002/wcc.8

Sathiyamoorthy, V. (2005). Large scale reduction in the size of the Tropical Easterly Jet. *Geophysical Research Letters*, *32*(14), Article ID L14802. https://doi.org/10.1029/2005GL022956

Sato, T., Kimura, F., & Kitoh, A. (2007). Projection of global warming onto regional precipitation over Mongolia using a regional climate model. *Journal of Hydrology*, *333*(1), 144–154. https://doi.org/10.1016/j.jhydrol.2006.07.023

Segele, Z. T., Lamb, P. J., & Leslie, L. M. (2009). Large-scale atmospheric circulation and global sea surface temperature associations with horn of Africa June-September rainfall. *International Journal of Climatology*, *29*(8), 1075–1100. https://doi.org/10.1002/joc.1751

Semazzi, F. H. M., & Sun, L. (1997). The role of orography in determining the sahelian climate. *International Journal of Climatology*, *17*, 581–596. https://doi.org/10.1002/(SICI)1097-0088(199705)17:6<581::AID-JOC134>3.0.CO;2-E

Speth, P., Christoph, M., Diekkrüger, B., Bollig, M., Fink, B. A. H., Goldbach, H., … RöSSLER, M. (2010). Impacts of global change on the hydrological cycle in west and Northwest Africa. In *Impacts of Global Change on the Hydrological Cycle in West and Northwest Africa*. https://doi.org/10.1007/978-3-642-12957-5

Sultan, B., & Janicot, S. (2000). Abrupt shift of the ITCZ over West Africa and intra-seasonal variability. *Geophysical Research Letters*, *27*(20), 3353–3356. https://doi.org/10.1029/1999GL011285

Sultan, Benjamin, Baron, C., Dingkuhn, M., Sarr, B., & Janicot, S. (2005). Agricultural impacts of large-scale variability of the West African monsoon. *Agricultural and Forest Meteorology*, *128*(1–2), 93–110.

https://doi.org/10.1016/j.agrformet.2004.08.005

Sultan, Benjamin, & Janicot, S. (2003). The West African monsoon dynamics. Part II: The “preonset” and “onset” of the summer monsoon. *Journal of Climate*, *16*(21), 3407–3427. https://doi.org/10.1175/1520-0442(2003)016<3407:TWAMDP>2.0.CO;2

Sylla, B. M., Diallo, I., & Pal, J. S. (2013). West African Monsoon in State-of-the-Science Regional Climate Models. In *Climate Variability - Regional and Thematic Patterns* (pp. 3–36). https://doi.org/10.5772/55140

Sylla, M. B., Dell’Aquila, A., Ruti, P. M., & Giorgi, F. (2010). Simulation of the intraseasonal and the interannual variability of rainfall over West Africa with RegCM3 during the monsoon period. *International Journal of Climatology*, *30*(12), 1865–1883. https://doi.org/10.1002/joc.2029

Sylla, M. B., Gaye, A. T., Pal, J. S., Jenkins, G. S., & Bi, X. Q. (2009). High-resolution simulations of West African climate using regional climate model (RegCM3) with different lateral boundary conditions. *Theoretical and Applied Climatology*, *98*(3–4), 293–314. https://doi.org/10.1007/s00704-009-0110-4

Tall, A., Mason, S. J., Van Aalst, M., Suarez, P., Ait-Chellouche, Y., Diallo, A. A., & Braman, L. (2012). Using seasonal climate forecasts to guide disaster management: The Red Cross experience during the 2008 West Africa floods. *International Journal of Geophysics*. https://doi.org/10.1155/2012/986016

Tao, W.-K., Simpson, J., & McCumber, M. (1989). An Ice-Water Saturation Adjustment. *Monthly Weather Review*, *117*(1), 231–235. https://doi.org/10.1175/1520-0493(1989)117<0231:aiwsa>2.0.co;2

Thorncroft, C. D., Parker, D. J., Burton, R. R., Diop, M., Ayers, J. H., Barjat, H., … Tompkins, A. M. (2003). The JET2000 Project: Aircraft Observations of the African Easterly Jet and African Easterly Waves. *Bulletin of the American Meteorological Society*, *84*(3), 337–352. https://doi.org/10.1175/bams-84-3-337

Thorncroft, C.D., & Blackburn, M. (1999). Maintenansce of the African easterly jet. *Quarterly Journal of the Royal Meteorological Society*, *125*(555), 763–786. https://doi.org/10.1256/smsqj.55501

Thorncroft, Chris D., Nguyen, H., Zhang, C., & Peyrille, P. (2011). Annual cycle of the

West African monsoon: Regional circulations and associated water vapour transport. *Quarterly Journal of the Royal Meteorological Society*, *137*(654), 129–147. https://doi.org/10.1002/qj.728

Tiedtke, M. (1989). A Comprehensive Mass Flux Scheme for Cumulus Parameterization in Large-Scale Models. *Monthly Weather Review*, *117*(8), 1779–1800. https://doi.org/10.1175/1520-0493(1989)117<1779:acmfsf>2.0.co;2

Tomas, R. A., & Webster, P. J. (1997). The role of inertial instability in determining the location and strength of near-equatorial convection. *Quarterly Journal of the Royal Meteorological Society*, *123*(542), 1445–1482. https://doi.org/10.1256/smsqj.54201

Tompkins, A. M., Cardinali, C., Morcrette, J. J., & Rodwell, M. (2005). Influence of aerosol climatology on forecasts of the African Easterly Jet. *Geophysical Research Letters*, *32*(10), ID L10801. https://doi.org/10.1029/2004GL022189

Ulate, M., Dudhia, J., & Zhang, C. (2014). Sensitivity of the water cycle over the Indian Ocean and Maritime Continent to parameterized physics in a regional model. *Journal of Advances in Modeling Earth Systems*, *6*, 1095–1120. https://doi.org/10.1002/2014MS000313

USAID. (2014). Enhancing rainfed agriculture. *https://www.usaid.gov/what-we-do/.../promoting.../enhancing-rainfed*

Vanvyve, E., Hall, N., Messager, C., Leroux, S., & van Ypersele, J. P. (2008). Internal variability in a regional climate model over West Africa. *Climate Dynamics*, *30*(2–3), 191–202. https://doi.org/10.1007/s00382-007-0281-6

Venkat Ratnam, M., Roja Raman, M., Mehta, S. K., Nath, D., Krishnamurthy, B. V., Rajeevan, M., … Narayana Rao, D. (2011). Sub-daily variations observed in Tropical Easterly Jet (TEJ) streams. *Journal of Atmospheric and Solar-Terrestrial Physics*, *73*(7–8), 731–740. https://doi.org/10.1016/j.jastp.2011.02.005

Vizy, E. K., & Cook, K. H. (2002). Development and application of a mesoscale climate model for the tropics: Influence of sea surface temperature anomalies on the West African monsoon. *Journal of Geophysical Research*, *107*(D3), ACL 2-1-ACL 2-22. https://doi.org/10.1029/2001jd000686

Wang, A., & Zeng, X. (2014). *Global hourly 0.5-degree land surface air tem- perature datasets. Research Data Archive at the National Center for Atmospheric Research,*

Computational and Information Systems Laboratory. doi:https://doi.org/10.5065/D6PR7SZF. Accessed 05 April 2017.

Wang, G., & Eltahir, E. A. B. (2000). Role of vegetation dynamics in enhancing the low-frequency variability of the Sahel rainfall. *Water Resources Research*, *36*(4), 1013–1021. https://doi.org/10.1029/1999WR900361

Wang, Y., Zhou, L., & Hamilton, K. (2007). Effect of convective entrainment/detrainment on the simulation of the tropical precipitation diurnal cycle. *Monthly Weather Review*, *135*, 567–585. https://doi.org/10.1175/MWR3308.1

Ward, J. D., Mohr, S. H., Myers, B. R., & Nel, W. P. (2012). High estimates of supply constrained emissions scenarios for long-term climate risk assessment. *Energy Policy*, *51*, 598–604. https://doi.org/10.1016/j.enpol.2012.09.003

Webster, P. J., & Fasullo, J. (2003). Monsoon: dynamical theory. In *in Encyclopedia of Atmospheric Sciences, J. Holton and J. A. Curry, Eds., Academic Press, London, UK* (pp. 1370–1385).

Xue, Y., De Sales, F., Lau, W. K. M., Boone, A., Kim, K. M., Mechoso, C. R., … Zhang, Z. (2016). West African monsoon decadal variability and surface-related forcings: second West African Monsoon Modeling and Evaluation Project Experiment (WAMME II). *Climate Dynamics*, *47*(11), 3517–3545. https://doi.org/10.1007/s00382-016-3224-2

Xue, Y., De Sales, F., Lau, W. K. M., Boone, A., Feng, J., Dirmeyer, P., … Wu, M. L. C. (2010). Intercomparison and analyses of the climatology of the West African Monsoon in the West African Monsoon Modeling and Evaluation project (WAMME) first model intercomparison experiment. *Climate Dynamics*, *35*(1), 3–27. https://doi.org/10.1007/s00382-010-0778-2

Yamada, T. J., Kanae, S., Oki, T., & Hirabayashi, Y. (2012). The onset of the West African monsoon simulated in a high-resolution atmospheric general circulation model with reanalyzed soil moisture fields. *Atmospheric Science Letters*, *13*(2), 103–107. https://doi.org/10.1002/asl.367

Zaroug, M. A., Sylla, M. B., Giorgi, F., Eltahir, E. A., & Aggarwal, P. K. (2013). A sensitivity study on the role of the swamps of southern Sudan in the summer climate of North Africa using a regional climate model. *Theoretical and Applied*

Climatology, *113*(1–2), 63–81.

Zhang, Chidong, Nolan, D. S., Thorncroft, C. D., & Nguyen, H. (2008). Shallow meridional circulations in the tropical atmosphere. *Journal of Climate*, *21*(14), 3453–3470. https://doi.org/10.1175/2007JCLI1870.1

Zhang, Chunxi, Wang, Y., & Hamilton, K. (2011). Improved Representation of Boundary Layer Clouds over the Southeast Pacific in ARW-WRF Using a Modified Tiedtke Cumulus Parameterization Scheme *. *Monthly Weather Review*, *139*(11), 3489–3513. https://doi.org/10.1175/mwr-d-10-05091.1

Zhang, Chunxi, Wang, Y., Lauer, A., & Hamilton, K. (2012). Configuration and Evaluation of the WRF Model for the Study of Hawaiian Regional Climate. *Monthly Weather Review*, *140*(10), 3259–3277. https://doi.org/10.1175/MWR-D-11-00260.1

Zuidema, P. (2003). Convective clouds over the bay of Bengal. *Monthly Weather Review*, *131*, 780–798. https://doi.org/10.1175/1520-0493(2003)131<0780:CCOTBO>2.0.CO;2